POLITECNICO DI TORINO
von Karman Institute for Fluid Dynamics

Master's degree in Aerospace engineering

---

# *Numerical aerodynamic investigation of two propellers in side-by-side configuration*

---


***Supervisors*:**
Prof. Francesco Avallone
Prof. Renzo Arina
Prof. Christophe Schram
Dr. Alessandro Zarri
Dr. Julien Christophe
Phd Candidate. Marco Picillo

***Candidate:***
Fabio Galante
S313369


Academic year 2024/2025

Von Karman Institute for Fluid Dynamics

## *Short Training Program Report 2024/2025*

# Numerical aerodynamic investigation of two propellers in side-by-side configuration

Date: October 2024 - March 2025
Address: Chaussée de Waterloo 72, 1640 Rhode-Saint-Genèse, Belgium

***Supervisors*:**
Prof. Christophe Schram
Dr. Alessandro Zarri
Dr. Julien Christophe

***Candidate*:**
Fabio Galante

*Natura non facit saltus*
*Leibniz*

# Abstract

The increasing focus on sustainability and the need to develop less polluting aircraft models have led to the emergence of Distributed Electric Propulsion (DEP) aircraft as a revolutionary solution.
The utilization of DEP systems has gained considerable traction in Electrical Vertical Take-Off and Landing (eVTOL) aircraft for urban and military applications. These vehicles, known for their versatility, efficiency, and technological innovation, require in-depth analysis of rotor configurations, generated noise, and aerodynamic performance.
This research aims to investigate the wake development and propeller interactions in DEP systems for urban air mobility (UAM). Specifically, it focuses on two side-by-side rotors placed along the wing of the eVTOL VX4 by Vertical Aerospace, analyzing tip vortex evolution in both hover and forward flight conditions.
The study explores the aerodynamic causes behind wake behavior and inter-propeller interaction, evaluating their impact on performance metrics.
The methodology employed is based on computational fluid dynamics (CFD) simulations. The different evolution of the wake will be analyzed through Unsteady Reynolds-Averaged Navier-Stokes (URANS) simulations for both single and side-by-side configurations. Subsequently, a comparison will be made with a low-order model to evaluate their applicability. The study aims to provide a comprehensive understanding of wake dynamics when propellers interact in close proximity.
The final results will show the evolution of the wake and tip vortex in both cases: single propeller and side-by-side configuration. The impact on performance will be assessed through various graphs that illustrate the effects of the interaction in one case compared to the other, and through comparisons across the various simulations. This project is part of the eVTOLUTION initiative, which is designed to develop the knowledge, data, tools, and methods necessary to understand, model, and optimize aerodynamic performance and noise emissions while accounting for the complex interferences between the propulsion system and the airframe.

# Table of Contents

# List of Figures

# List of Tables

# List of Symbols

$B$ Blade number

$c$ speed of sound

$p$ pressure

$\rho$ density

$h$ enthalpy

$v$ velocity

$T$ temperature

$t$ time

$V$ control volume

$q$ heat flux

$n$ surface unit normal

$E$ energy

$I$ moment of inertia

$R^*$ specific gas constant

$s$ entropy

$S$ rigid surface

$J$ advance ratio

$\tau$ viscous stress tensor

$\nu$ kinematic viscosity

$\mu$ dynamic viscosity

$\nu_T$ turbulent viscosity

$\epsilon$ turbulence dissipation rate

$\kappa$ thermal conductivity

$\omega$ vorticity field

$x_p$ position of particle

$\delta$ Dirac function

$I$ moment of inertia

$L_B$ computational size

$G$ filter function

$u_i^{'}$ fluctuating velocity part

$U_i$ mean velocity part

$Re$ reynolds number

$-\rho\overline{u_j^{'}u_i^{'}}$ reynolds stress tensor

$a_{ij}$ anisotropy tensor

$\overline{S_{ij}}$ mean strain rate tensor

$\Omega$ mean rotation rate

$l_m$ mixing length

$\Gamma$ vortex strength

$\Pi$ stress tensor

$c_l$ lift coefficient

$\tau_{ij}^a$ anisotropic residual stress tensor

$C_T$ thrust coefficient

$J$ advance ratio

$R$ radius

$D$ diameter

$n$ propeller rotational speed

XVII

# List of Acronyms

**eVTOL** electric Vertical Take-Off and Landing

**UAM** Urban Air Mobility

**UAV** Unmanned Aerial Vechicle

**DEP** Distributed Electric Propulsion

**uRANS** unsteady Reynolds-Averaged Navier Stokes

**RANS** Reynolds-Averaged Navier Stokes

**DNS** Direct Numerical Simulation

**PDE** Partial Differential Equation

**rVPM** reformulated Vortex Particle Method

**CFD** Computation fluid dynamics

**BS** Base size

**CW** Clockwise

**DEP** Distributed Electric Propulsion

**RBF** Radial Basic Function

**SFS** Subgrid Scales

**FF** Forward Flight

# Chapter 1

# Introduction and Motivation

## 1.1 Urban Air Mobility (UAM): Context and Challenges

*Urban Air Mobility (UAM)* represents one of the most promising prospects in modern aviation. The growth of large metropolitan areas and the need for more environmentally sustainable transport solutions have driven the development of aircraft designed to operate in urban environments, offering safe and fast alternatives to traditional transportation. *eVTOLs* (electric Vertical Take-Off and Landing aircraft) are playing a key role in the technological transition, providing energy efficiency and reduced carbon emissions thanks to electric propulsion. Short travel times, operation in confined spaces, and minimal need for large-scale airport infrastructure are just some of the many advantages offered by this new class of aircraft [1].
The aviation industry is actively exploring further solutions to reduce the environmental impact of air travel. The use of alternative fuels such as biojet fuel could be a valid option. Wind energy is also an essential resource for powering ground infrastructure. Airlines and UAM manufacturers are investing in innovative solutions to integrate renewable energy sources effectively. Some initiatives include carbon offset programs, allowing passengers to partially compensate for the emissions generated by their flights [2].
From an aerodynamic perspective, UAM vehicles benefit from optimized designs for flight performance. They ensure stability in highly populated urban environments and during ground maneuvers. Despite the positive outlook for UAM vehicles, there are still technical challenges to address, such as air traffic integration and noise management. The latter is especially important for eVTOLs operating in densely populated areas, as they can produce disturbing noise due to tip vortex interactions

and other aerodynamic effects [3].
Research and development in the UAM field are highly active, focusing on the energy efficiency of electric motors and noise reduction, to enable greater mobility in urban areas. Urban Air Mobility represents the future of urban transport, offering significant benefits in terms of energy efficiency and reduced travel times. However, technical challenges must be addressed through practical and innovative solutions.
UAM also places strong emphasis on safety and redundancy. The use of aircraft configurations with multiple propulsion systems and advanced flight control technologies ensures that these vehicles can continue operating safely even in the event of a component failure. This level of redundancy is essential to ensure passenger safety and operational reliability, particularly in urban environments where a failure could have serious consequences [4, 5].
*Distributed Electric Propulsion (DEP)* aircraft represent an important advancement. This configuration, which also includes eVTOLs, offers advantages in airflow management in different flight conditions and in reducing aerodynamic drag. However, interaction between nearby propellers can lead to instability and noise, highlighting the need for further studies aimed at optimizing design and improving aerodynamic performance in different configurations. In an era where energy efficiency and sustainability are global priorities, DEP aircraft offer a valuable contribution by harnessing renewable energy sources and enhancing the sustainability of air transport [6, 7].

(a) *Airbus CityAirbus eVTOL*

(b) *VX4 eVTOL Vertical aerospace*

Figure 1.1: *Unmanned Aerial Vehicles examples*

## 1.2 Literature Review and Key Findings

In recent years, the interaction between two adjacent propellers has been the subject of numerous studies, and it has been identified as one of the main mechanisms for unstable noise generation and its impact on aerodynamic performance. It is crucial to investigate the area of interaction between the propellers both experimentally

and numerically to understand the mechanisms of noise generation and propagation and how these affect the surrounding environment under both hover and forward flight conditions.
*Yoon et al.* [8] found significant airflow interference caused variations in the flow velocity and pressure. Investigating airflow dynamics, especially in the presence of significant interference, is essential. These interferences can cause crucial variations in the flow velocity and pressure, which must be closely monitored and analyzed.
The increase in noise level generation, which is a crucial issue for understanding the mechanisms of unstable noise generation and propagation, was investigated by *Zhou et al* [9]. This question was solved by investigating the interaction between two adjacent propellers, which significantly contributes to the overall noise. This phenomenon is particularly problematic in densely populated urban environments where noise pollution negatively impacts residents' quality of life.
The concept of unstable loads (*Sinibaldi et al. [10]*) is also important for understanding the performance and behavior of urban air vehicles. They also examined how load variations affect propeller stability and efficiency. An unstable load can lead to unwanted oscillations and vibrations, which not only reduce the aerodynamic efficiency but can also increase the generated noise level.
Another important phenomenon relates to the tip vortices of rotor blades (*Leslie et al.* [11] ). These vortices increased the airflow dispersion and reduced the aerodynamic efficiency. It has been shown that vortices created by blade tips can increase the flow dispersion, leading to a significant reduction in the aerodynamic efficiency. This effect is particularly relevant for urban air vehicles and multi-rotor drones, where optimizing energy efficiency is crucial.
Misiorowski et al. [12] investigated how the separation distance between rotors significantly influences aerodynamic interactions. They demonstrated that variations in the separation distance can alter the airflow distribution, thereby affecting the thrust force and aerodynamic performance.
*Zhou et al. [9]* highlighted that when the separation distance exceeds 0.5 D, the thrust fluctuations measured in the case of adjacent rotors significantly attenuate, reaching a level similar to that of a single rotor. Conversely, when the rotor approached and the separation distance decreased below 0.5 D, a reduction in thrust was observed, which can be attributed to the generation of an unstable field and the interaction of the tip vortices caused by the two adjacent propellers. Starting from 0.4 D, thrust fluctuations were generated by the interaction of the flow fields of the two propellers.
It has been observed that the proximity between the propellers can negatively influence thrust generation, demonstrating that this closeness can cause a thrust loss of up to 8%. Additionally, it has been found that while the separation distance has

a very limited effect on the rotor's thrust coefficient (i.e., variation within 2% for all test cases), thrust fluctuations (i.e., the standard deviation of thrust) increase drastically as the separation distance decreases.
A recent study by *de Vries et al.* [13] involving an array of three adjacent propellers focused on the forward flight conditions. The authors observed a 1.5% efficiency loss compared to the isolated propeller case for a tip distance equal to 4% of the propeller radius. Additionally, the wake flows generated by each propeller did not merge, thus creating a high-velocity flow region, contrary to previous assumptions. In fact, the time-averaged evolution of the wake flows was not drastically influenced when the propellers were close to each other.
Consequently, each wake flow can be easily distinguished in the downstream orientation when a wing is installed. This can be attributed to the predominance of inertial forces over viscous forces during forward flight, which results in less intense viscous interactions than hovering and prevents the wake flows from deforming and merging.
In a study investigating a side-by-side configuration under hover conditions (*Piccinini et al.* [14]) it was found that the greatest effect of aerodynamic interaction on propeller performance occurred at the smallest lateral separation distance between them. Specifically, a slight reduction in the average propeller thrust and propulsive efficiency (less than 1%) was detected in the case of interaction compared with the single propeller configuration.
On the other hand, a high-amplitude of load fluctuations was observed under this test condition, which could pose aeroacoustic issues. The visualization of the instantaneous flow field demonstrates the strong interaction between the tip vortices released by the two lateral propellers. The prevalence of viscous forces over inertial forces under hover conditions causes the interaction and deformation of the wakes of the two propellers.

This brief literature review overviews the main phenomenological effects of the interaction between two adjacent propellers, highlighting their influence on the aerodynamic performance and the generation of unstable noise. Despite significant progress, many open questions and phenomena still require further investigation.

## 1.3 Motivation

In the topics discussed earlier, it is noted that urban aviation is rapidly evolving, with electric vertical takeoff and landing (eVTOL) aircraft representing the future of sustainable air transport. However, the success of these innovative technologies strongly depends on understanding the aerodynamic dynamics of the propellers

used. The side-by-side configuration of the propellers can significantly affect the generated wake.
Studies have shown that the wake in hover exhibits greater contraction than in forward flight. However, in a side-by-side configuration, thrust in hover is reduced more significantly than in forward flight, likely due to various factors that require investigation. Understanding the cause of this phenomenon is crucial for generating a high-fidelity numerical database for eVTOL vehicles.
This study is based on the need to numerically investigate, using *CFD*, the aerodynamic interactions between two propellers in a side-by-side configuration in hover and forward flight.
The simulations will be conducted using a URANS approach with Simcenter Star-CCM+ software. Starting from the numerical setup, hover and forward flight simulations will be developed for both single and side-by-side propeller configurations. Subsequently, a low-order model based on the vortex particle method (FLOWUnsteady) will be implemented to investigate differences in tip vortex evolution, aerodynamic effects, and noise impact, ultimately comparing these results with the URANS simulations.
The primary objective is to understand how the configuration influences the aerodynamic flow fields produced by the propellers of an eVTOL and how the impact of the interaction on performance is evaluated.
Specifically, it aims to examine:

- *Differences in wake evolution*: analyze how the wake generated by the propellers evolves in both side-by-side and isolated configurations, and how it is presented in the analysis of various flow fields.
- *Tip vortex interaction*: investigate the dynamics of tip vortices and their evolution in both configurations.

Results will be visualized through plots and analyses highlighting the effects of wake contraction and development in the two configurations and in comparison with the various simulations.
Understanding these aspects is essential for optimizing propeller design and improving the overall performance of eVTOLs. This research aims to provide new insights and engineering solutions that can contribute to the development of more efficient and sustainable urban air mobility.

## 1.4 Research questions to address

The questions that merit investigation pertain to the analysis of aerodynamic factors impacting performance.

1. Study of the wake between hover and forward flight configurations in side-by-side interaction.
    - Why is thrust in hover reduced more than thrust in forward flight, despite the stronger contraction in the former case?
    - What occurs aerodynamically?
2. Comparison of various simulation models to observe differences in tip vortex evolution
    - Is it necessary to conduct an URANS simulation?
    - How do the differences in wake evolution present across the various models? Are the aerodynamics accurately modeled?

## 1.5 Thesis outline

*Chapter 1*: introduces the field of interest of the thesis, defines the research questions and project objectives, and presents the motivation behind this work. The main technical challenges on which the project is based are also discussed.
*Chapter 2*: focuses on the theoretical foundations. This chapter describes the theoretical principles supporting the thesis work, including fluid dynamics theory and the vortex particle method. These concepts are essential for the following chapters.
*Chapter 3*: explains the fundamental concepts of CFD and the numerical models used to capture and discretize turbulence and turbulent flows.
*Chapter 4*: presents the numerical setup used in the simulations. This chapter explains the numerical methodology adopted, detailing the various numerical models and the simulation process. A comprehensive overview is provided of the key parameters, the mesh, and the boundary conditions applied in each case.
*Chapter 5*: addresses the first research question, presenting the simulations performed under both conditions, along with the plots and results, to highlight the aerodynamic causes behind the side-by-side configuration.
*Chapter 6*: answers the second research question by showing the comparison with the low-order method and assessing its reliability in reproducing the aerodynamic effects.
*Chapter 7*: summarizes the conclusions reached and outlines future work that can be developed based on this thesis.

# Chapter 2

# Theoretical background

This chapter addresses the theoretical aspects of fluid dynamics to understand the main equations and models used by simulation software to analyze the propeller wake. The primary governing equations from the literature, relevant to the phenomena under investigation, will be presented.

## 2.1 Navier-Stokes equations

The Navier-Stokes equations are fundamental to fluid dynamics [15], as they describe the motion of Newtonian fluids. These equations are the foundation of computational fluid dynamics (CFD) and are derived from the principles of conservation of mass, momentum, and energy, in accordance with the continuum hypothesis. They are partial differential equations (PDE) that include unknowns such as velocity, represented $v$ (rapresented as $u_1$, $u_2$, $u_3$), pressure $p$ and temperature $T$. The final form of the Navier-Stokes equations also incorporates additional thermodynamic variables density $\rho$, enthalpy $h$, viscosity $\mu$ and thermal conductivity $k$. The resulting system consists of six unknowns but only five equations. To close the system, the ideal gas law is applied.

$$p = \rho R^* T \tag{2.1}$$

The term $R^*$ refers to the specific gas constant. The system of partial differential equations (PDEs) can be closed by establishing appropriate boundary conditions and remains valid as long as the continuum hypothesis for the fluid is maintained. Thus, a *physical model* has been developed, which must be translated into mathematical language and subsequently solved numerically. To achieve this, we consider a fluid that adheres to our continuum hypothesis, envisioning that this fluid flows through a specific virtual control volume (a non-physical entity), as seen in Figure 2.1 base on personal notes.

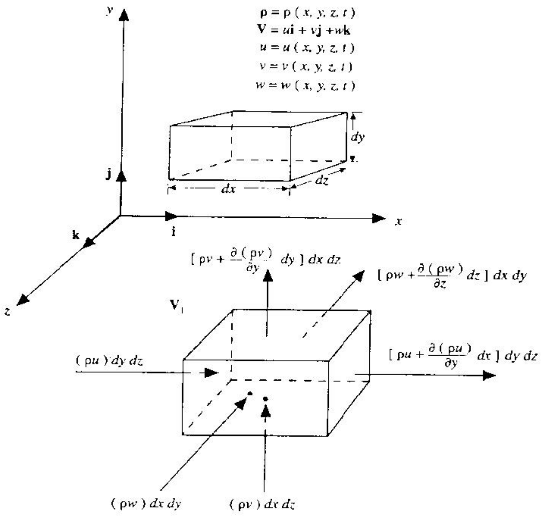


Figure 2.1: *Control volume*

Consider a control volume and imagine observing the events occurring solely within it while disregarding everything outside, Figure 2.2 based on personal notes. This control volume can be categorized into four types, ensuring that the equations we formulate are physically equivalent but may take on different forms depending on the type of control volume being analyzed. It is always possible to interchange these forms, allowing for a straightforward mathematical transition from one representation to another. Thus, there exists one physical form and four mathematical representations. The *control volume* can therefore be classified as follows:

1. Finite and fixed control volume *integral equations in conservative form*)
2. Infinitesimal and fixed control volume (*differential equations in conservative form*)
3. Finite and moving control volume (*integral equations in non-conservative form*)
4. Infinitesimal and moving control volume (*differential equations in non-conservative form*)

The fixed volume in space represents the *Eulerian* viewpoint, while the moving volume represents the *Lagrangian* viewpoint. Although the mathematical forms of the equations differ depending on the choice of control volume, these equations convey the same physical meaning. In integral form, both volume and surface integrals are utilized; in differential form, the operator $\nabla$ is employed. When using the *conservative form*, local time derivatives are included, whereas the non-conservative form introduces the *Lagrangian derivative*.

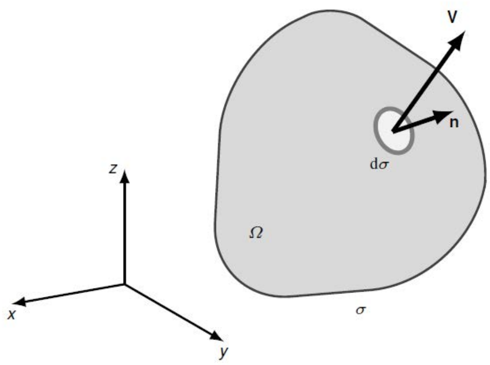


Figure 2.2: *Reference system*

The equations of motion for a viscous fluid are derived by applying the following principles:

- *conservation of mass*: mass is neither created nor destroyed
- *conservation of momentum*: the change in momentum is equal to the applied forces
- *conservation of energy*: energy is neither created nor destroyed

Conservation of mass is a kinematic condition that does not concern the forces applied to the fluid within the control volume. Instead, these forces are relevant to the principle of conservation of momentum, a generalized form of *Newton's law*, and to the principle of energy, which is a broader interpretation of the *first law of thermodynamics*.

### 2.1.1 Conservation of mass

Fictitious mass sources are introduced, resulting in an average net mass of zero, as they both contribute to and reduce mass, when $\overrightarrow{v} \cdot \overrightarrow{n} > 0$ it indicates that mass is exiting the control volume, because $\overrightarrow{n} > 0$ is outgoing, and therefore the control volume is decreasing its mass, there is a mass deduction. Considering the mass per unit volume $\rho$, let $u$ represent the velocity field of the fluid flow, with $f(\rho, u) = \rho u$ and an arbitrary volume $\Omega$, we derive the l*'differential form of the mass conservation equation* also known as the*continuity equation*:

$$\frac{\partial \rho}{\partial t} + \nabla \cdot (\rho u) = Q_m \tag{2.2}$$

where $Q_m$ represents mass generation per unit volume and time.

### 2.1.2 Conservation of momentum

The changes in momentum per unit volume, denoted as $\rho u$ are governed by the integral balance among the momentum flux $\rho uu$, the action of external forces per unit volume $\rho f$, the surface forces represented by the stress tensor $\Pi$ and the change in momentum due to the mass generation of the current $u$. It is assumed that the introduced mass $Q_m$ has a velocity equal to the local value of the current $\overrightarrow{u}$. For an arbitrary volume $\Omega$, the quasi-linear conservative differential form of the momentum equation is:

$$\rho \frac{\partial u}{\partial t} + \rho u \cdot \nabla u = \nabla \cdot \Pi + \rho f \tag{2.3}$$

### 2.1.3 Conservation of energy

Total energy per unit mass is defined as the sum $E = \epsilon + \frac{V^2}{2}$ where $\epsilon$ represents internal energy and $\frac{V^2}{2}$ denotes kinetic energy. Variations in total energy per unit volume $\rho E$ are attributed to the balance of flux $\rho E u$, surface sources $\Pi \cdot u$, and surface heat fluxes $-q \cdot n$. Additionally, volumetric sources can be further decomposed into the work (per unit time) of external forces $\rho f \cdot u$, and volumetric heat sources $Q_w$. Finally, the energy associated with the mass source $Q_m$, is considered, assuming it is introduced with the same local total energy $E$ as the current. If it is introduced with the same velocity, it will possess the same kinetic energy and will also have the same internal energy $\epsilon$, which depends on temperature. The quasi-linear conservative differential form of the energy equation is derived as follows:

$$\rho \frac{\partial E}{\partial t} + \rho u \cdot \nabla E = \nabla \cdot (\Pi \cdot u) - \nabla \cdot q + \rho f \cdot u + Q_w \tag{2.4}$$

Using the quasi-linear form, it can be observed that $Q_m$ is eliminated from the momentum and energy equations, remaining solely in the continuity (mass balance) equation.

### 2.1.4 Constitutive relations

The stress tensor $\Pi$ is decomposed into the sum of an isotropic component and a non-isotropic component.

$$\Pi = -pI + \tau \Longrightarrow \sigma_{ij} = -p\delta_{ij} + \tau_{ij} \tag{2.5}$$

where the pressure $p$ represents the average value of the normal components $\sigma_{ij}$ of the stress tensor

$$p \equiv -\frac{1}{3}(\sigma_{11} + \sigma_{22} + \sigma) = -\frac{1}{3}\sum_i \sigma_{ii} \tag{2.6}$$

Since the stress state at each point reflects the mutual interactions of adjacent fluid elements, it is logical to correlate the viscous stresses with the local kinematic properties. A linear relationship exists between the symmetric stress tensor $\tau$ and the symmetric part $D$ of the tensor $\nabla u$ in the case of an isotropic fluid, which is expressed as follows:

$$\tau = 2\mu D + \lambda(\nabla \cdot u)I \tag{2.7}$$

$$\tau_{ij} = \mu(\frac{\partial u_i}{\partial x_j} + \frac{\partial u_j}{\partial x_i}) + \lambda\delta_{ij}\frac{\partial u_k}{\partial x_k} \tag{2.8}$$

According to Newton's law, there is a direct proportionality between shear stress and the velocity gradient. When the system is stationary, the equation is represented as $\Pi = -pI$. However, if there are gradients in $u$ both $\sigma$ and $\tau$ are present; otherwise, only the isotropic component $-p$ exists, which is always present in the fluid.

**Aeroacoustic prediction methods** The method utilized to assess aerodynamic noise caused by turbulence is known as Computational AeroAcoustics (CAA) [16, 17]. Initially, one must consider the fluid dynamic field, where motion is non-stationary, as stationary motion would not generate noise.
In the realm of computational aeroacoustics, several challenges must be addressed. In the realm of acoustic analogy, the CFD simulation is performed first, followed by the acoustic analysis. There are more or less costly methods. The Large Eddy Simulation requires very fine grids near the walls and has a moderate computational cost. RANS or URANS (Reynolds-Averaged Navier Stokes) use Reynolds-averaged equations along the wall and have a low computational cost for a coarse grid.
. Many aeroacoustic issues in the industry involve flow fields with low Mach numbers, which present a significant disparity between hydrodynamic and acoustic waves. Computational aeroacoustics calculations utilize a hybrid method, as seen in Figure 2.3, consisting of solving the flow fields near the body first and then analyzing the results in the far field through wave propagation. This process requires substantial computational resources, a numerical scheme with low dissipation, a large but finite domain, and non-reflective boundary conditions.

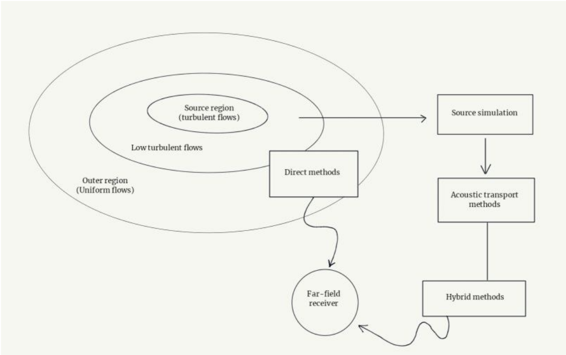


Figure 2.3: *CAA procedure*

The noise associated with propellers can be classified into two categories: tonal and broadband noise [18]. Broadband noise is random, non-periodic, and excites all frequencies. Conversely, tonal noise is related to the periodic motion of the blade and excites only one frequency.
The noise of an isolated propeller is determined by three factors: the thickness, the periodic movement of air due to the rotation of the blade surfaces at a certain blade pass frequency ($BPF = \frac{B\Omega}{60}$; $B$ is the number of the blade, $\Omega$ is the rotation rate). It also includes the aerodynamic load distributed along the propeller blades and the quadrupole noise generated by the interactions between the sound waves emitted by the blades and the turbulence present in the surrounding airflow.
In this thesis project, the numerical aeroacoustic investigation of the VX4 propeller will not be carried out. However, as previously stated, it is necessary to determine the force distribution on the propeller to calculate the far-field noise and investigate its directivity. This challenge could be addressed in future work following this thesis.

c

## 2.2 Vortex Particle Method

This study will address the reformulated Vortex Particle Method (rVPM) utilized by the FLOWUnsteady software to discretize the flow field of the propeller. Vortex methods [19, 20] are a class of meshless Computational Fluid Dynamics (CFD) techniques that solve the Navier–Stokes equations in their velocity–vorticity form. This approach utilizes a Lagrangian scheme. This approach tracks fluid particles over time.
The Vortex Particle Method (VPM) uses particles to discretize these equations [21], with particles representing radial basis functions (RBFs) to construct a continuous vorticity field. While not optimal for all problems, VPM is well-suited for wake-

dominant flows in unbounded domains. Its advantages include:

1. It does not suffer from the Courant–Friedrichs–Lewy condition;
2. It has minimal numerical dissipation ;
3. Its velocity field derivatives are calculated analytically rather than approximated through a stencil;
4. When used with a fast multipole method (FMM), it is computationally efficient;

Despite its popularity, VPM is known for numerical instability near the turbulent regime. In his paper, doctoral student Edoardo Alvarez [21] proposed a stable and meshless VPM formulation. Stability is achieved by modeling VPM as a Large-Eddy Simulation (LES) and capturing Subgrid-Scale (SGS) effects. This new formulation, the Reformulated Vortex Particle Method (rVPM), is implemented in the open-source software FLOWVPM.

### 2.2.1 Fundamentals of the VPM

A new set of VPM governing equations is derived from the LES-filtered Navier-Stokes equations in their vorticity form.

**Vorticity Form of the Navier-Stokes Equation** The vorticity equation [21–23] for an incompressible fluid is obtained by taking the curl of the Navier–Stokes linear momentum equation:

$$\frac{D}{Dt}\omega = (\omega \cdot \nabla)u + \nu\nabla^2\omega \tag{2.9}$$

In this equation: $D$ is the total of material derivative, $u(x,t)$ is the velocity field, $\nu$ is the kinematic viscosity and $\omega(x,t) = \nabla \times u(x,t)$ represents the vorticity field. The evolution of the vorticity field, as shown on the right-hand side, is driven by vortex stretching (first term) and viscous diffusion (second term).

**LES equation** Let's derive the filtered vorticity Navier–Stokes equation , known as the LES equation [21], is derived using a filter kernel $\zeta_\sigma$. The filtered field is represented by an overline and is defined as follows:

$$\overline{\phi}(x) \equiv \int_{-\infty}^{\infty} \phi(y)\zeta_\sigma(x-y)dy \tag{2.10}$$

where $\zeta_\sigma(x) \equiv (\frac{1}{\sigma^3})\zeta(\frac{||x||}{\sigma})$ , where $\zeta$ represents a Radial basis function with $\int_{-\infty}^{\infty} \zeta_\sigma(y)dy = 1$.
To derive the LES version of the vorticity equation, is re-written in tensor notation and then filtered. We obtain the LES vorticity equation:

$$\overline{\frac{\partial \omega_i}{\partial t}} + \overline{u_j \frac{\partial \omega_i}{\partial x_j}} = \overline{\omega_j}\ \overline{\frac{\partial u_i}{\partial x_j}} + \nu \overline{\nabla^2 \omega_i} - \frac{\partial T'_{ij}}{\partial x_j} + \frac{\partial T_{ij}}{\partial x_j} \tag{2.11}$$

The term $\frac{\partial T'_{ij}}{\partial x_j}$ accounts for the contributions from the subgrid scale (SFS) advection, while $\frac{\partial T_{ij}}{\partial x_j}$ pertains to contributions from vortex stretching.
$T_{ij}$ is linked to the SFS vorticity stress, encapsulating the interactions between large-scale and subgrid-scale dynamics.
For convenience, we write the LES vorticity equation in vector notation as

$$\frac{d}{dt}\overline{\omega} = (\overline{\omega} \cdot \nabla)\ \overline{u} + \nu \nabla^2 \overline{\omega} - E_{adv} - E_{str} \tag{2.12}$$

where $(E_{adv})_i \equiv \frac{\partial T'_{ij}}{\partial x_j}$ is the SFS vorticity advection and $(E_{str})_i \equiv -(\frac{\partial T_{ij}}{\partial x_j})$ is the SFS vortex stretching.

**The Vortex particle** The $\omega$ field is particularly suited for a Lagrangian description due to the conservative nature of vorticity. Each particle represents a fluid volume convected by the velocity field, carrying an integral quantity of vorticity.
The unfiltered $\omega$ field is discretized with singular vortex particles of positions $x_p$ and coefficients $\Gamma_p$, approximating $\omega$ as

$$\omega_{x,t} \approx \sum_p \Gamma_p(t)\delta(x - x_p(t)) \tag{2.13}$$

where $\delta$ is the Dirac delta. Each particle travels with the local velocity as

$$\frac{d}{dt} x_p = u(x_p) \tag{2.14}$$

$x_p$ is the position of the *p-th* particle, $\Gamma_p$ represents the average vorticity carried within the volume of each particle. The approximation of the filtered velocity field is:

$$\omega(x) \approx \sum_p \Gamma_p \zeta_P(x - x_p) \tag{2.15}$$

The filtering process distributes the vortex strength over space, thereby smoothing out the singularity introduced by the Dirac delta.

**General VPM governing equations** Starting from the inviscid part of the LES-filtered vorticity equation:

$$\frac{d}{dt}\overline{\omega} = (\overline{\omega} \cdot \nabla)u - E_{adv} - E_{str} \tag{2.16}$$

By employing the singular particle approximation, $\omega(Y) \approx \sum_q \Gamma_q \delta(y - x_q)$ both integrals simplify:

$$\frac{d}{dt}(\sum_p \Gamma_q \zeta_{\sigma_q}(x - x_q)) = \frac{d}{dt}(\sum_p \Gamma_q \zeta_{\sigma_q}(x - x_q)) \cdot \nabla]u(x) - E_{adv}(x) - E_{str}(x) \tag{2.17}$$

The terms $M$ establish interdependence between particles:

$$\begin{aligned}\frac{d\Gamma_p}{dt} &= (\Gamma_P \cdot \nabla)u(x_p) + 3\Gamma_p \frac{1}{\sigma_p}\frac{\partial \sigma_p}{\partial t} + \frac{1}{\zeta_{\sigma_p}(0)}(-M_p^0 + M_p^1 + M_p^2) \\ &- \frac{1}{\zeta_{\sigma_p}(0)}(E_{adv}(x_p) + E_{str}(x_p))\end{aligned} \tag{2.18}$$

The variation in vortex strength $\Gamma$ is determined by vortex stretching (first term), particle expansion or contraction (second term), interactions with other particles and SFS contributions.

### 2.2.2 Classic VPM governing equations

This equation is referred to as the classic VPM [21].

$$\frac{d\Gamma_p}{dt} = (\Gamma_p \cdot \nabla)u(x_p) \tag{2.19}$$

Over the years, various modifications have been introduced:

$$\begin{aligned}\frac{d\Gamma_p}{dt} &= (\Gamma_p \cdot \nabla)u(x_p) + 3\Gamma_p \frac{1}{\sigma_p}\frac{\partial \sigma_p}{\partial t} \\ &+ \frac{1}{\zeta_{\sigma_p}(0)}(-M_p^0 + M_p^1 + M_p^2)\end{aligned} \tag{2.20}$$

This approximation of localized vorticity is valid without significant particle overlap. However, the assumption $\frac{\partial \sigma_p}{\partial t} = 0$ is not clear and is hypothesized to be the cause of the numerical instability that pervades the cVPM.

### 2.2.3 Reformulated VPM

The Navier-Stokes equation for vorticity represents the conservation of angular momentum in a spherical fluid element:

$$(\omega \cdot \nabla)u = -\frac{\omega}{I}\frac{d}{dt}I \tag{2.21}$$

The term $\omega \cdot \nabla u$ is called vortex stretching because it considers the deformation induced by the velocity field on the fluid element, amplifying the vorticity in the direction in which the element is stretched.
The classic cVP violated the conservation of angular momentum by assuming $(\frac{d}{dt})_\sigma = 0$, and this was the reason for the generation of numerical instability.

### 2.2.4 SFS model

The focus is on the SFS stresses [21] associated with advection $E_{adv}$ and vortex stretching $E_{str}$. A structural model of SFS vortex stretching with a dynamic model coefficient $C_d$ has been developed.
The advective term is neglected, and the focus is on the term $E_{Str}$.

**Dynamic procedure** SFS vortex stretching is modeled as:

$$E_{str} \approx -[\overline{(\omega \cdot \nabla)u} - (\overline{\omega} \cdot \nabla)\overline{u}] \tag{2.22}$$

Introducing a dynamic model coefficient $C_d(x,t)$:

$$C_d E_{str} = -[\overline{(\omega \cdot \nabla)u} - (\overline{\omega} \cdot \nabla)\overline{u}] \tag{2.23}$$

However, this relation is not useful to us because it includes exactly what we are trying to model with $E_{str}$.
Nonetheless, we differentiate this equation with respect to the filter width, recalling various definitions, evaluating it at $x = x_p$ and through the assumption of localized vorticity, becomes:

$$C_d(x_p)\frac{1}{\zeta_\sigma(0)}\frac{\partial E_{str}}{\partial \sigma}(x_p) = \frac{3}{\sigma}(\Gamma_p \cdot \nabla)(u(x_p) - \overline{u}(x_p)) + (\Gamma_p \cdot \nabla)\frac{\partial \overline{u}}{\partial \sigma}(x_p) \tag{2.24}$$

or

$$C_d m = L \tag{2.25}$$

**Enstrophy-production balance** It is necessary to impose a balance of enstrophy production between the true and modeled SFS contributions. After several mathematical steps, using the singular particle approximation, $\omega(x) \approx \Gamma_p \delta(x - x_p)$, the integrals reduce to:

$$\sum_p \Gamma_p \cdot (\frac{d}{dt}\overline{\omega})^{SFS\ model}_{(x_p)} = \sum_p \Gamma_p \cdot (\frac{d}{dt}\overline{\omega})^{true\ SFS}_{(x_p)} \tag{2.26}$$

Following the same steps of definitions and assumptions from the previous paragraph, the enstrophy balance becomes:

$$C_d \Gamma_p \cdot m = \Gamma_P \cdot L \tag{2.27}$$

and $C_d$ can be dynamically calculated as:

$$C_d = \frac{\Gamma_p \cdot L}{\Gamma_p \cdot m} \tag{2.28}$$

Thus, this $C_d$ calculated at the position of each particle is the coefficient that, by approximating the derivative balance, satisfies the local balance of enstrophy production between the model and the true SFS contribution.

In summary, the proposed scheme uses a reformulation of the VPM and a novel SFS vortex stretching model to achieve a meshless LES.

# Chapter 3

# Computational Fluid dynamics Methods

Understanding computational fluid dynamics is essential for simulating turbulent motions and the various vortical structures generated by the objects under analysis. The primary aspects of turbulence and the fundamental equations underlying the RANS and LES numerical models, which are employed to resolve turbulence and model the wake, will be presented.

### 3.0.1 Components of a numerical solution method

- These mathematical methods [24, 25] consist of a set of partial differential equations or integro-differential equations that describe the physical model. To locally approximate these equations using a system of algebraic equations for the variables, we rely on *discretization methods*:

1. *Finite differences (FD)*
2. *Finite volumes (FV)*
3. *Finite elements (FE)*

In fluid dynamics, finite volumes are mainly used, and sometimes finite differences and finite elements (in the structural field).

- A system of *cartesian, cylindrical, or spherical coordinates* is set up
- A *numerical grid*, is defined to place these discrete points in space. The grid can be organized in various ways: - structured: the points are ordered and uniquely identifiable with one or more indices - unstructured: there is no index

ordering, and the point is simply identified through a map that associates the point with a cell

- *Solution method*: the solution method of the nonlinear algebraic system produced by the discretization process of the differential system
- *Convergence criterion*: the criteria adopted to decide when to stop the iterative process embedded in the solution method.

### 3.0.2 The two most common discretization approaches in fluid dynamics

The *finite difference* discretization [26] method, Figure 3.1 based on personal notes, is used for differential equations. It approximates derivatives and is characterized by grid nodes.
The nodes can be internal, with an unknown value of the variables to be calculated, or boundary nodes, where boundary conditions must be imposed. The selection of boundary conditions is the part that requires the most attention.

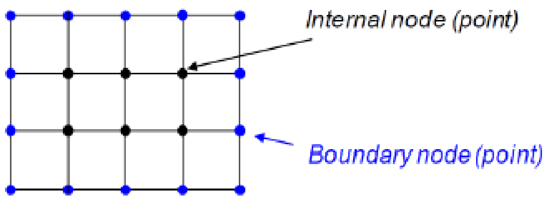


Figure 3.1: *Finite differences*

The finite volume discretization method, Figure 3.2 based on personal notes, is used to approximate integrals and is characterized by cells (where the integral mean of the cell is symbolically concentrated at the cell center) and boundary surfaces, where boundary conditions will be imposed.

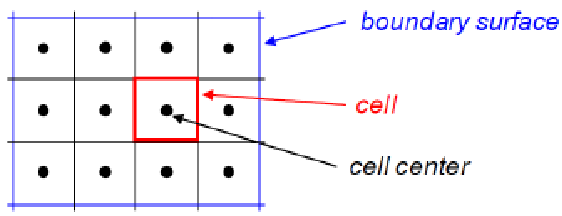


Figure 3.2: *Finite volumes*

On the red faces, the fluxes will be calculated, while on the blue faces, the fluxes depending on the boundary conditions will be determined.

### 3.0.3 Cell reconstruction

After correctly imposing these conditions, it is necessary to ensure the most accurate representation of the domain and variables within the cells.
To achieve an accurate representation of the variables within the cells of the computational domain, various reconstruction techniques are used to improve the accuracy of simulations.

- *Piecewise constant reconstruction*: in this approach, each variable is considered constant within each cell. The accuracy may be low, especially in the presence of significant gradients.
- *Piecewise linear reconstruction*: in this approach, each variable is approximated with a linear function within each cell (slope). This method offers greater accuracy compared to piecewise constant reconstruction, but requires more computational effort.

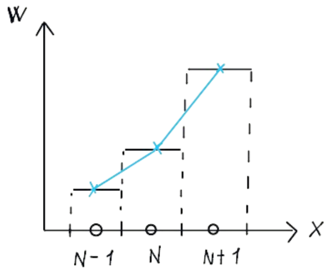


Figure 3.3: *Cell reconstruction*

### 3.0.4 REA method

The reconstruction step is the first step of the *REA method (Reconstruct-Evolve-Average)* [27,28], used to solve transport equations in CFD simulations. The three fundamental steps of the method are:

1. *Reconstruct*: At the beginning of each time solution, the solution is reconstructed from the cell averages $w_N^K$. In this context, $w$ represents the conservative variables, the quantities that are conserved (mass per unit volume, momentum per unit volume, and energy per unit volume) averaged within each cell of the computational domain. These averages are used to construct a piecewise polynomial function $\widetilde{w}(x, t^K)$ (constant or linear) defined for all

values of $x$. In the simplest case, it is a piecewise constant function that takes the value $w_N^K$ of the grid cell, that is,

$$\widetilde{w}(x, t^K) = w_N^K \tag{3.1}$$

for all $x \in C_N$, con $\widetilde{w}(x, t^K)$ representing the cell reconstruction. The reconstruction impacts the spatial accuracy of the system; the higher the reconstruction order, the more spatially accurate the scheme becomes.

2. *Evolve*: the reconstructed data is evolved exactly (or approximately) over time according to the hyperbolic equation $w_t + \overline{a}w_x = 0$ (with $\overline{a}$ being the signal speed) to obtain $\widetilde{w}(x, t^{K+1})$ at the next time $\Delta t$.
3. *Average*: the evolved solution is averaged over each grid cell to obtain new cell averages.

$$w_N^{K+1} = \frac{1}{\Delta x} \int_{x_{N-\frac{1}{2}}}^{x_{N+\frac{1}{2}}} \widetilde{w}(x, t^{K+1}) dx \tag{3.2}$$

The critical step is the second one because at the beginning of each time step, the solution is reconstructed using piecewise data that create a discontinuity at the cell edges.
In particular, the focus is on the interfaces between two contiguous cells, as the goal is to evaluate the fluxes at the interfaces. The evolution process is carried out using the theory of *Riemann problems*.

The REA method ensures high accuracy in simulations, but to achieve the best results, it is essential to have a quality mesh. Its shape directly affects the accuracy and effectiveness of the REA algorithm.
A well-constructed mesh allows for solving transport equations with greater precision, improving the representation of physical phenomena.

## 3.1 Understanding turbulent flow dynamics

In turbulent flow dynamics, it's crucial to understand how flows behave. Turbulence [29] rapidly spreads energy, momentum, and phases. Though a fully satisfying definition of turbulent flows has yet to be found, one possible definition is *dynamic situations of flow fields that do not strictly adhere to boundary conditions* [30]. Here are some key points about turbulence:

- *Random Process*: Turbulence is random; we know the fundamental laws and the system from a physical-mathematical perspective, but analytical solutions for all situations are complex. Hence, statistical analysis is used

- *Multiscale*: turbulence involves many scales, from the largest to the smallest. These scales overlap in the flow, with smaller scales existing within larger ones.
- *Small-Scale Random Vorticity*: each scale in a turbulent flow has its vorticity, even the smallest scales. Spatial and temporal fluctuations can be much quicker than velocity fluctuations, especially at smaller scales.
- *High Reynolds Numbers (Re)*: turbulence occurs at high Reynolds numbers due to the instability of laminar flow at these values. A laminar flow exceeding the critical Reynolds number becomes unstable and, thus turbulent.
- *Energy Dissipation*: at high *Re*, small-scale formation triggers an inertial cascade phenomenon, where energy is dissipated at the smallest scales due to viscous action. The fragmentation across scales results in increasing gradients, leading to intense gradients at the smallest scales.
- *Continuum Phenomenon*: small-scale turbulence fully satisfies the continuum hypothesis, as these scales are much larger than the mean free path, and their size depends on viscosity.
- *Inherently Three-Dimensional*: Turbulent structures are always three-dimensional. 2D turbulence only makes statistical sense, as it would imply smaller structures merge to form larger ones, which contradicts the 3D case.
- *Highly Diffusive*: Turbulence has a significant capacity to diffuse energy, momentum, and concentration, far greater than molecular diffusion.

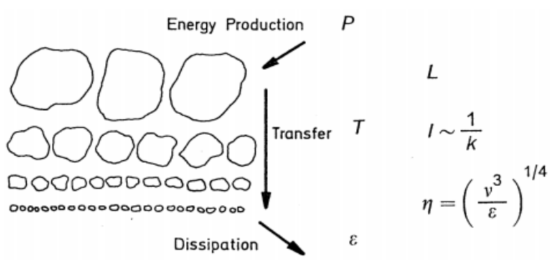


Figure 3.4: *Inertial cascade*

### 3.1.1 Numerical methods for studying turbulent flows

Modeling turbulence is essential in Computational Fluid Dynamics (CFD) because turbulent flows have complex fluctuations that require significant computational power to fully simulate.
To simplify calculations, the governing equations can be modified to remove small-

scale fluctuations, which necessitates turbulence models to close these modified equations. There are two extremes in turbulence modeling:

- *RANS (Reynolds-Averaged Navier-Stokes)*: Manages all scales of vortices without directly resolving them.

- *DNS (Direct Numerical Simulation)* resolves all vortices but requires extremely high computational resources for high Reynolds numbers. In general, the computational cost is very high for any type of simulation. A practical compromise is *LES (Large Eddy Simulation)*, which resolves only large-scale vortices, making it more manageable from a computational standpoint, although still more demanding than a URANS. Often, the choice of turbulence models is limited by the available or accessible computational resources needed to run the simulations. This limitation is crucial when aiming to accurately capture turbulence and its structure, as it forces the selection of one method over another based on the resources at hand.

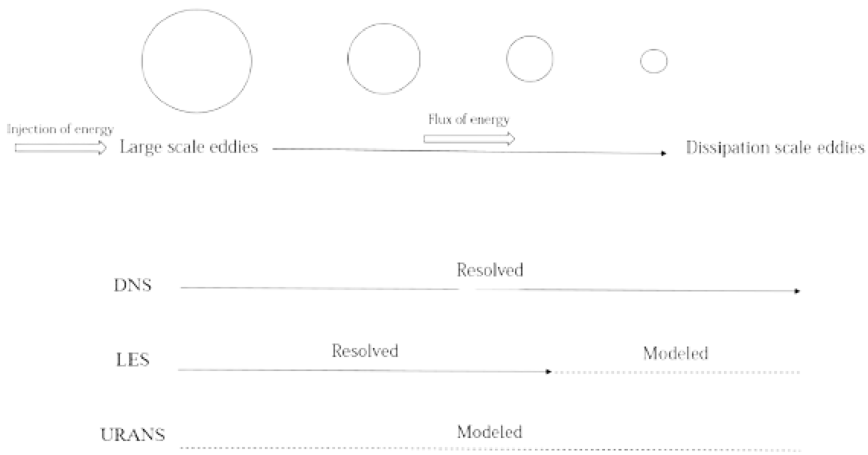


Figure 3.5: *Numerical methods for turbulence*

**LES (Large Eddy Simulation)** In turbulent flows with [31] a high enough Reynolds number, it's assumed that the small-scale motion statistics have a universal form, independent of boundary conditions. Therefore, flow quantities can be decomposed into large-scale and small-scale contributions using a spatial filter. Large-scale contributions are explicitly calculated on a relatively coarse grid, while the effects of small-scale contributions on the large-scale flow are modeled. The filtering operation is defined to decompose the velocity $u_i(\overrightarrow{x},t)$ into a filtered (or resolved) component $\hat{U}_i(\overrightarrow{x},t)$ and a residual (or sub-grid scale, SGS) component $u_i^{'}(\overrightarrow{x},t)$

$$u_i(\overrightarrow{x},t) = \hat{U}_i(\overrightarrow{x},t) + u_i^{'}(\overrightarrow{x},t) \tag{3.3}$$

In the future, an LES simulation will be conducted for the eVTOL VX4 propeller, but with an adequate computational resource budget.

## 3.2 RANS (Reynolds-averaged Navier-Stokes)

Following the Reynolds decomposition [32] into mean and fluctuating parts

$$u_i = U_i + u_i^{'} \tag{3.4}$$

$$p = P + p^{'} \tag{3.5}$$

the mean flow equations are the continuity equation and the momentum equation:

$$\frac{\partial U_i}{\partial x} = 0 \tag{3.6}$$

$$\frac{\partial U_i}{\partial t} + U_j \frac{\partial U_i}{\partial x_j} = -\frac{1}{\rho}\frac{\partial P}{\partial x_i} + \nu \frac{\partial^2 U_i}{\partial x_j \partial x_j} - \frac{\partial \overline{u_i^{'} u_j^{'}}}{\partial x_j} \tag{3.7}$$

the Reynolds stress tensor $-\rho\overline{u_j^{'} u_j^{'}}$ represents the mean flow of momentum due to turbulent fluctuations, and its divergence appears as a volumetric forcing in the mean flow.
The Reynolds stresses, which appear as unknowns in the Reynolds equations [33], are determined by a turbulence model (closure problem), or through: • the hypothesis of turbulent viscosity • the modeled transport equations of Reynolds stresses

RANS allows the calculation of only the mean flow and not the fluctuations.

**TVH turbulent viscosity hypothesis (Boussinesq)** According to Boussinesq's hypothesis of turbulent viscosity (tvh) [34], analogous to the stress-rate-of-strain relationship, the Reynolds stresses are given by

$$-\rho\overline{u_i^{'} u_j^{'}} + \frac{2}{3}\rho k \delta_{ij} \equiv -\rho \cdot a_{ij} = \rho \nu_T (\frac{\partial U_i}{\partial x_j} + \frac{\partial U_j}{\partial x_i}) \equiv 2\rho\nu_T \overline{S_{ij}} \tag{3.8}$$

where $k = \frac{\overline{u_i^{'} u_i^{'}}}{2}$ is the turbulent kinetic energy per unit mass, $\overline{S_{ij}}$ is the mean strain rate tensor, , $a_{ij}$ is the anisotropy tensor, and $\nu_T(\overrightarrow{x},t)$ is the turbulent viscosity or

eddy viscosity. The TVH implies that the tensor $a_{ij}$ is aligned with the tensor $\overline{S_{ij}}$. Assuming TVH, the Reynolds equations have the same form as the Navier-Stokes equations.
It is worth noting the similarity with LES: the eddy viscosity represents the influence of turbulence on the mean flow, while the sub-grid viscosity expresses the influence of sub-grid scales on resolved scales in specific flow realizations.
Having adopted the turbulent viscosity hypothesis for the Reynolds stress tensor, it is necessary to assume a defined expression for $\nu_T(\overrightarrow{x}, t)$ (turbulence modeling) to complete the closure of the Reynolds equations and perform the numerical simulation.

### 3.2.1 Mixing Length Model

Assuming this algebric model, the turbulent viscosity is given by:

$$\nu_T = l_m^2 \sqrt{2\overline{S}_{ij}\overline{S}_{ij}} \equiv l_m^2 \overline{S} \tag{3.9}$$

such as the Smagorinsky model, or by

$$\nu_T = l_m^2 \sqrt{\overline{\Omega}_{ij}\overline{\Omega}_{ij}} \equiv l_m^2 \overline{\Omega} \tag{3.10}$$

such as the Baldwin or Lomax model, where $l_m(\overrightarrow{x})$ is the mixing length (considering spatial evolution while neglecting temporal evolution) and $\Omega$ is the mean rotation rate

$$\overline{\Omega}_{ij} \equiv \frac{1}{2}(\frac{\partial U_i}{\partial x_j} - \frac{\partial U_j}{\partial x_i}) \tag{3.11}$$

The mixing length model is applicable to all turbulent flows. The main disadvantage is that the mixing length $l_m(\overrightarrow{x})$ must be specified (inevitably based on the flow geometry).

### 3.2.2 Turbulent Kinetic Energy Model (One-Equation Model)

Analogous to the kinetic theory of gases where the kinematic viscosity is given by $\nu \approx \frac{\overline{C}\lambda}{2}$ (with $\overline{C}$ representing the average molecular velocity and $\lambda$ the mean free path) , the turbulent viscosity [35] can be expressed as the product of a velocity and a length:

$$\nu_T(\overrightarrow{x}, t) = u^*(\overrightarrow{x}, t) \cdot l^*(\overrightarrow{x}, t) \tag{3.12}$$

the task of specifying $\nu_T$ is addressed through the specifications of $u^*$ and $l^*$. In the turbulent kinetic energy model (one equation model)

$$l^* = l_m \qquad u^* = ck^{\frac{1}{2}} \tag{3.13}$$

with $k$ as the turbulent kinetic energy and $c$ a costant. Thus, the turbulent viscosity becomes:

$$\nu_T = c\sqrt{k}l_m \tag{3.14}$$

$k(\overrightarrow{x}, t)$ must be known or estimated. Kolmogorov and Prandtl suggested achieving this by solving a model transport equation for $k$. The turbulent kinetic energy is written as:

$$\frac{\partial \frac{1}{2}\overline{q^2}}{\partial t} = \underbrace{-\overline{u_i^{'}u_j^{'}}\frac{\partial U_i}{\partial x_j}}_{produzione} - \underbrace{\bar{\epsilon}}_{dissipazione\ turbolenta} + \underbrace{T}_{trasferimento\ di\ energia\ turbolenta} \tag{3.15}$$

Transporting the convection term using the mean flow term to the first member, applying the continuity equation, and denoting $I_i$ as the diffusion term and $\Pi$ as the production term, we obtain:

$$\frac{\partial k}{\partial t} + U_i\frac{\partial k}{\partial x_i} = \Pi - \epsilon - \frac{\partial I_i}{\partial x_i} \tag{3.16}$$

with $k = \frac{1}{2}q$. $I_i$ is modeled as the diffusion of the scalar quantity $k$, that is

$$I_i = -\frac{\nu_T}{\sigma_k}\frac{\partial k}{\partial x_i} \tag{3.17}$$

with $\sigma_k$ being a constant. The dissipation rate $\epsilon$ is seen to be proportional to $\frac{u_0^3}{l_0}$ where $u_0$ and $l_0$ are the velocity and length scales of the energy-containing motions (large-scale vortices). Consequently, it is reasonable to model $\epsilon$ as:

$$\epsilon = C_D\frac{k^{\frac{3}{2}}}{l_m} \tag{3.18}$$

with $C_D$ a constant.

**Concluding Model of the One-Equation Model** The continuity equation is:

$$\frac{\partial U_i}{\partial x_i} = 0 \tag{3.19}$$

The Reynolds equations are:

$$\frac{\partial U_i}{\partial t} + U_j \frac{\partial U_i}{\partial x_j} = -\frac{1}{\rho}\frac{\partial P}{\partial x_i} + \nu \frac{\partial^2 U_i}{\partial x_j \partial x_j} - \frac{\partial \overline{u_i' u_j'}}{\partial x_j} \tag{3.20}$$

The TVH hypothesis is:

$$-\overline{u_i' u_j'} + \frac{2}{3} k \delta_{ij} = 2\nu_T \overline{S}_{ij} \tag{3.21}$$

with $\nu_T = ck^{\frac{1}{2}} l_m$. The turbulent kinetic energy equation is:

$$\frac{\partial k}{\partial t} + U_i \frac{\partial k}{\partial x_i} = \Pi - \epsilon - \frac{\partial I_i}{\partial x_i} \tag{3.22}$$

with

$$\Pi = -\overline{u_i' u_j'} \frac{\partial U_i}{\partial x_j} \tag{3.23}$$

$$\epsilon = C_D \frac{k^{\frac{3}{2}}}{l_m} \tag{3.24}$$

$$I_i = -\frac{\nu_T}{\sigma_k} \frac{\partial k}{\partial x_i} \tag{3.25}$$

Costants $c = 0.55$ and $C_D = c^3$ produce correct behavior in the log-law region, and , $\sigma_k$ is generally $\sigma_k = 1$.
This one-equation model offers a modest advantage in terms of accuracy compared to the mixing length model. The main disadvantage is that $l_m(\overrightarrow{x})$ must be specified. The primary advantage lies in having a greater number of constants to adjust.

### 3.2.3 Model (Two-Equation Model)

The $k - \epsilon$ model [36, 37] is the most comprehensive turbulence model used, but it is also the most demanding, as it requires the values of multiple constants to be utilized; the specifications of $l_m(\overrightarrow{x})$ are not required. The starting point, as in the one-equation model, is

$$\nu_T = u^*(\overrightarrow{x}, t) \cdot l^*(\overrightarrow{x}, t) \tag{3.26}$$

As in the one-equation model, the reference velocity $u^*$ is considered the square root of the turbulent kinetic energy.

$$u^* \approx \sqrt{k} \tag{3.27}$$

and the length scale can be calculated from $k$ and $\epsilon$ as

$$l^* \approx \frac{\sqrt{k}}{\epsilon} \tag{3.28}$$

| | |
|---|---|
| $C_\mu$ | 0.09 |
| $C_{\epsilon_1}$ | 1.44 |
| $C_{\epsilon_2}$ | 1.92 |
| $\sigma_k$ | 1.0 |
| $\sigma_\epsilon$ | 1.3 |

Table 3.1: *Numerical Constants*

Thus, the turbulent viscosity is assumed to be

$$\nu_T = C_\mu \frac{k^2}{\epsilon} \tag{3.29}$$

with $C_\mu$ being one of the five constants of the model. Experiments have determined that $C_\mu = 0.09$ everywhere except near flow boundaries, where it is difficult to manage. At this point, two model transport equations for $k$ and $\epsilon$. The model equation for $k$ has already been written:

$$\frac{\partial k}{\partial t} + U_i \frac{\partial k}{\partial x_i} = \Pi - \epsilon - \frac{\partial I_i}{\partial x_i} \tag{3.30}$$

with

$$\Pi = -\overline{u_i^{'} u_j^{'}} \frac{\partial U_i}{\partial x_j} \tag{3.31}$$

$$I_i = -\frac{\nu_T}{\sigma_k} \frac{\partial k}{\partial x_i} \tag{3.32}$$

An exact equation for $\epsilon$, can also be derived, but it is not useful as it pertains to processes in the dissipative range. It is more appropriate to view $\epsilon$ as the rate of energy flow in the energy cascade, determined by large-scale motions.
In any case, empiricism would be introduced into the exact equation for closure requirements. Rather than relying on the exact equation, it is better to consider the standard model equation for $\epsilon$ as entirely empirical:

$$\frac{\partial \epsilon}{\partial t} + U_i \frac{\partial \epsilon}{\partial x_i} = C_{\epsilon 1} \frac{\epsilon}{k} \Pi - C_{\epsilon_e} \frac{\epsilon^2}{k} + \frac{\partial}{\partial x_i} \left( \frac{\nu_T}{\sigma_\epsilon} \frac{\partial_\epsilon}{\partial x_i} \right) \tag{3.33}$$

The standard values of the five constants involved in the $k - \epsilon$ model are obtained through empirical fitting of predictions and experiments:

**Concluding Model of the Two-Equation Model $k-\epsilon$** The continuity equation is:

$$\frac{\partial U_i}{\partial x} = 0 \tag{3.34}$$

The Reynolds equation are:

$$\frac{\partial U_i}{\partial t} + U_j \frac{\partial U_i}{\partial x_j} = -\frac{1}{\rho}\frac{\partial P}{\partial x_i} + \nu \frac{\partial^2 U_i}{\partial x_j \partial x_j} - \frac{\partial \overline{u_i' u_j'}}{\partial x_j} \tag{3.35}$$

The TVH hypothesis is:

$$-\overline{u_i' u_j'} + \frac{2}{3} k \delta_{ij} = 2\nu_T \overline{S}_{ij} \tag{3.36}$$

with $\nu_T = C_\mu \frac{k^2}{\epsilon}$ The model equation for turbulent kinetic energy is:

$$\frac{\partial k}{\partial t} + U_i \frac{\partial k}{\partial x_i} = \Pi - \epsilon - \frac{\partial I_i}{\partial x_i} \tag{3.37}$$

with

$$\Pi = -\overline{u_i' u_j'} \frac{\partial U_i}{\partial x_j} \tag{3.38}$$

$$I_i = -\frac{\nu_T}{\sigma_k} \frac{\partial k}{\partial x_i} \tag{3.39}$$

The model equation for the rate of dissipation is:

$$\frac{\partial \epsilon}{\partial t} + U_i \frac{\partial \epsilon}{\partial x_i} = \underbrace{C_{\epsilon_1} \frac{\epsilon}{k} \Pi}_{>0} - \underbrace{C_{\epsilon_e} \frac{\epsilon^2}{k}}_{<0} + \frac{\partial}{\partial x_i}\left(\frac{\nu_T}{\sigma_\epsilon} \frac{\partial_\epsilon}{\partial x_i}\right) \tag{3.40}$$

with the various constants defined in the previous table. The $k - \epsilon$ model has been applied to a wide range of problems, including heat transfer, combustion, and multiphase flows.
The $k - \epsilon$ model is incorporated into most commercial CFD codes and is computationally inexpensive when used in conjunction with wall functions, which introduce analytical and empirical "patch" functions (poor from a mathematical standpoint).

### 3.2.4 Reynolds Stress Transport Equations Model ($R_{ij} - \epsilon$ model)

Closure is provided to the Reynolds equations through model transport equations [38] for the individual Reynolds stress $\overline{u_i' u_j'}$ and for the dissipation rate $\epsilon$.
The evolution equation for $\varphi$ used in the $k - \epsilon$ model can be adopted with some

rearrangements. The exact transport equations for the Reynolds stresses have been derived from the Navier-Stokes equations:

$$\frac{\partial \overline{u_i' u_j'}}{\partial t} + U_k \frac{\partial \overline{u_i' u_j'}}{\partial x_k} = -\overline{u_i' u_k'} \frac{\partial U_j}{\partial x_k} - \overline{u_j' u_k'} \frac{\partial U_i}{\partial x_k} - \frac{\partial \overline{u_i' u_j' u_k'}}{\partial x_k} - \frac{1}{\rho} \left( \overline{u_i' \frac{\partial p'}{\partial x_j}} + \overline{u_j' \frac{\partial p'}{\partial x_i}} \right) + \nu \left( \overline{\frac{\partial^2 u_i'}{\partial x_k \partial x_k}} + \overline{\frac{\partial^2 u_j'}{\partial x_k \partial x_k}} \right) \tag{3.41}$$

The exact transport equation can (as usual) be rewritten as:

$$\frac{\partial R_{ij}}{\partial t} + U_k \frac{\partial R_{ij}}{\partial x_k} = P_{ij} + \Psi_{ij} - \epsilon_{ij} - \frac{\partial D_{kij}}{\partial x_k} \tag{3.42}$$

with $R_{ij} = \overline{u_i' u_j'}$, $P_{ij}$ the production tensor

$$P_{ij} = -\frac{\partial U_j}{\partial x_k} R_{ik} - \frac{\partial U_i}{\partial x_k} R_{jk} \tag{3.43}$$

and $\Psi_{ij}$ is the pressure-strain tensor, which redistributes energy among the Reynolds stresses

$$\Psi_{ij} = \Pi_{ij} - \frac{1}{3} \Pi_{ij} \delta_{ij} \tag{3.44}$$

where

$$\Pi_{ij} = -\frac{1}{\rho} \overline{(u_i' \frac{\partial p'}{\partial x_j} + u_j' \frac{\partial p'}{\partial x_i})} \tag{3.45}$$

Furthermore $\epsilon_{ij}$ is the dissipation tensor

$$\epsilon_{ij} = 2\nu \overline{\frac{\partial u_i'}{\partial x_k} \frac{\partial u_j'}{\partial x_k}} \tag{3.46}$$

and $\frac{\partial D_{ijk}}{\partial x_k}$ is the diffusion, with

$$D_{kij} = \overline{u_i' u_j' u_k'} + \frac{2}{3} \frac{1}{\rho} \delta_{ij} \overline{u_k' p'} - \nu \frac{\partial R_{ij}}{\partial x_k} \tag{3.47}$$

the flux of Reynolds stresses. The last three terms require closure as they cannot be precisely expressed in terms of the basic model variables, $\overline{U_i}$, $R_{ij}$, and $\epsilon$.

### 3.2.5 URANS (Unsteady Reynolds-averaged Navier Stokes equations)

The URANS method [39,40] is capable of capturing unsteady effects and large-scale instabilities. However, this technique cannot resolve small-scale flow oscillations due to high diffusivity, which is an inherent feature of URANS closure models.
The time-averaged vortex structure is well reproduced in URANS simulations. The equations are:

$$\frac{\partial \overline{U_i}}{\partial x_i} = 0 \tag{3.48}$$

$$\frac{\partial \overline{U_i}}{\partial t} + \overline{U_j}\frac{\partial \overline{U_i}}{\partial x_j} = -\frac{1}{\rho}\frac{\partial \overline{P}}{\partial x_i} + \nu\frac{\partial^2 \overline{U_i}}{\partial x_j^2} - \frac{\partial \overline{U_i' U_j'}}{\partial x_j} \tag{3.49}$$

In RANS, the flow properties are decomposed into their mean and fluctuating components, and time integration (i.e., time-averaging) is performed.
The difference between RANS and URANS is that an additional unsteady term is present in the URANS momentum equation. However, URANS simulations are computationally more expensive than steady-state RANS simulations.
The precise increase in numerical cost depends heavily on the flow in question and is usually lower than that of LES.

# Chapter 4

# Numerical Setup for CFD Simulations

In the following chapter, the numerical setup used for the computational fluid dynamics simulation on *Star-CCM+* is considered. The geometry used is the result of theoretical backgrounds and adaptations to better capture the flow in areas of interest and investigate the evolution of the tip vortex through refinement. Two numerical setups will be used:

1. Single propeller configuration

2. Side-by-side configuration of two adjacent propellers to investigate the interaction of the tip vortex and the tip vortex evolution.

Subsequently, the process and steps employed by FLOWUnsteady to generate the low-order simulation through VPM are examined.

## 4.1 Geometry

The CAD used is related to the company Vertical Aerospace, represented in Figure 4.1b, specifically the *VX4 aircraft*. The propeller is a scaled version of the VX4 and comprises 5 blades attached to the central hub. The rotor has a diameter of 0.26 m and a hub diameter of 0.04 m. The CAD was provided by the company, as seen in Figure 4.1a, with holes present on the central part of the spinner, which are sealed to prevent the passage of air that could influence the simulation results. The blade chord has a length of 0.032 m. The provided geometry does not include the propeller motor.

(a) *Propeller VX4* (b) *VX4 vehicle*

Figure 4.1: *Geometry CAD*

## 4.2 Domain

In the *Star-CCM+* software, a computational domain [41, 42] was constructed around the propeller geometry . For the large outer domain, a bullet-shaped domain was used to avoid reflection phenomena that could distort the flow and to achieve greater numerical stability. The outer domain faces were divided into: *domain inlet*, *domain outlet* and *domain side.*
Using the diameter as the characteristic length $L$ the outer domain is $100L$ downstream. The propeller is located at the center of the large domain, contained within the rotating region, which is necessary to evaluate the propeller's rotation. It was verified that the Mach number at the tip of the blades is $M < 0.3$, reflecting the incompressibility.

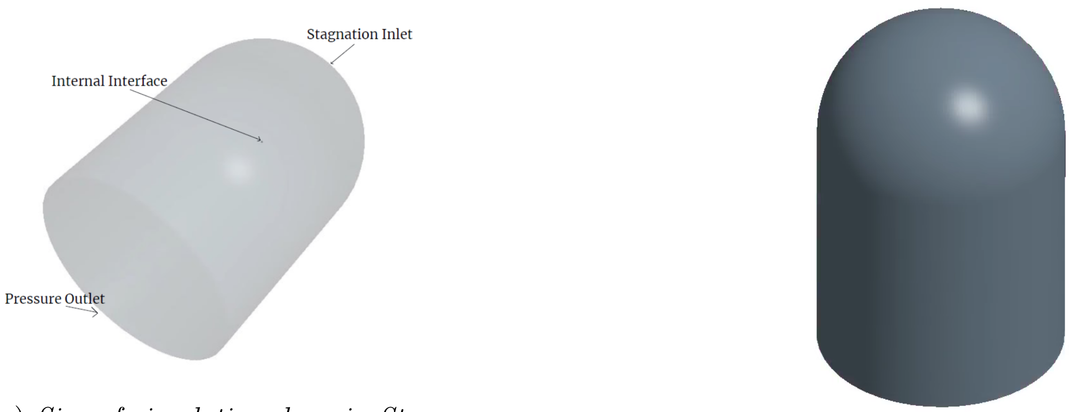


(a) *Size of simulation domain Star-CCM+* (b) *Simulation domain*

Figure 4.2: *StarCCM+ domain*

## 4.3 Rotating region

To simulate the rotation of the propeller, it was necessary to insert a rotating region that included the propeller., as seen in Figure 4.3. In the simulation for the isolated propeller, the rotating region consists of a simple cylinder that encompasses it, with an interface at the edges of this cylinder with the rest of the outer domain.
In the side-by-side configuration, there are two rotating regions, one for each propeller (and the cartesian reference system is positioned equidistant from the two propellers' centroids).
The set rotation rate is *6000 RPM*, and the movement is counterclockwise. The rotating region will be characterized by a high number of cells to better capture the vortices present. The faces are 3: *rotate inlet*, *rotate outlet* e *rotate side*.
The distance between the blade tip and the sliding mesh is considered to be approximately $\frac{2\%D}{3}$.

Figure 4.3: *Rotating region*

## 4.4 Boundary conditions

To set the boundary conditions in the simulation, it is necessary to transition from the parts created by the geometry to the regions. Two regions were created for this simulation: *Fluid* and *Rot*.
The boundary conditions set for the *Fluid*, region concern the large outer domain and the part of the rotating region included in the large domain.

For the *Rot* region, the boundary conditions are set for the rotating region and the propeller surfaces.
The boundary conditions reflect the hover conditions of the propeller as well as forward flight conditions. Initially hover conditions were set for the various faces of the outer domain, the *stagnation inlet* was set on the domain inlet, the *stagnation inlet* on the domain side, and the *outlet* on the domain outlet.
Subsequently, interfaces were created between the rotating region in the *Rot* region and the region in the *Fluid* region.
The boundary conditions on the propeller faces are *no-slip* conditions (Wall). For the forward flight condition, it is necessary to establish different boundary conditions. An inlet velocity of $V = 20.8m/s$ corresponding to an advance ratio $J = 0.8$.
For the inlet part of the domain, the boundary condition is set as a *velocity inlet*, where the velocity inlet into the domain is defined in the physical model of the simulation. For the side part of the domain, a *freestream* boundary condition is imposed, and for the outlet of the domain, an *outlet* boundary condition is applied

## 4.5 Physics models and solvers

The physical model [43–45] used in the simulation reflects the physics of the problem and it is presented in the Table 4.1. It is based on the use of the *ideal gas* model, which reflects the behavior of the fluid, and *three dimensional* model, which considers all three spatial dimensions to accurately capture flow characteristics in all directions.
*Coupled flow*, means that the energy equation is solved in conjunction with the other equations, unlike *segregated flow*, which solves them separately.
The turbulence model used includes the *K-Omega* model and the *SST (Shear Stress Transport) K-$\omega$* model, which combines the advantages of the *K-epsilon* and *K-$\omega$* models for greater accuracy in turbulence simulations.
*Implicit unsteady*, implies the use of an implicit approach to solving unsteady problems, allowing for greater stability in simulations. The implicit unsteady requires specifying a *time step* and *order of discretization*.
The time step indicates the time interval for marching in time, while the order of discretization indicates how the slope is reconstructed for each cell. Choosing to reconstruct as *piecewise constant* (first order) or *piecewise linear* (second order), impacts the oscillations that will be damped or not, using slope limiters for stability.
Regarding the solvers, the *time step* to be used based on the simulation was specified, the *inner iterations* between one time step and the next to ensure that the residuals converge, the *order of discretization* to best approximate the slope in the

cells, the *maximum physical time* and the *rotation rate* of the propeller.

| | URANS |
|---|---|
| Dimension | Three dimensional |
| Turblunce Model | k-$\omega$ SST |
| Flow Regime | Turbulent Flow |
| Equation of State | Ideal Gas |
| Solver | Coupled Flow |
| Time-Dependent | Unsteady |
| Time-Step Size | 2.77777778 x $10^{-5}$ s |
| Time Discretization | $2^{nd}$ |
| Inner Iterations | 10 |
| Maximum physical time | 5 s |
| Propeller rate | 6000 RPM |

Table 4.1: *Physics model*

## 4.6 Mesh generation

The next step after defining the physical model and the boundary conditions is the generation of the actual mesh and the cells that surround the geometry, as shown in Figure 4.4. Essentially, the choice of mesh can fall on two models:

- *polyhedral unstructured mesh*
- *block-structured trimmed mesh*

The *Star-CCM+* help center [43] suggests that using a polyhedral mesh leads to more accurate results and fewer numerical instabilities compared to the trimmed mesh.

There are two meshes present in the simulation: *Fluid mesh* and *Rot mesh.* The first mesh refers to the larger part of the computational domain, including only the boundary surfaces of the rotating region. The second mesh refers to the rotating region and the treatment of the interface between the two meshes.

The interface between [46, 47] the mesh in the rotating region and the remaining mesh of the computational domain must be appropriately treated so that at each time step, when the mesh rotates, the cell size of the mesh in the rotating region matches the cell size of the mesh in the remaining computational domain.

The quality of a good mesh is seen in the smooth transition of the generated cells. If the transition between the various cell sizes is good, then the simulation is likely to be problem-free.

The *Fluid mesh* includes, in addition to the large domain, an outer cylinder [48,49] that encompasses the various refinements of the propeller and the rotating region. The *Rot mesh* includes various parts of the propeller, the rotating region, and the various refinements used to accurately capture the tip-tip interaction and the tip vortex evolution.
The density and size of the cells were chosen to achieve an optimal compromise between a mesh capable of accurately capturing vortices and computational cost. The two meshes are generated by choosing the polyhedral mesh model, using the *prism layer mesher,* which is a layer of prisms to correctly capture the boundary layer.
The number of prism layers used is $N = 15$, to ensure proper development of the boundary layer thickness.
There are many parameters that influence the refinement and generation of the mesh.

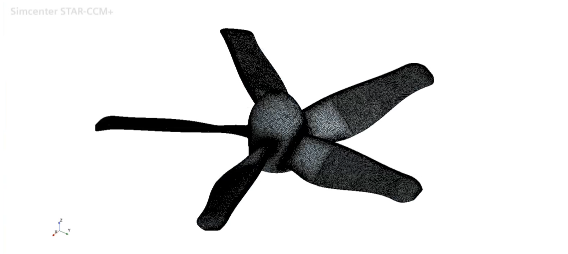


Figure 4.4: *Mesh*

Understanding the *Courant–Friedrichs–Lewy* ($CFL$) number was crucial in ensuring the lowest possible $CFL$ at the blade tip, to achieve accurate capturing of the generated tip vortices. Regarding $y+$ which measures the discretization quality of the boundary layer, it is ideally kept below 1. In our simulation, the maximum value observed was around 2. This indicates that using 15 prism layers, appropriate stretching of these layers outward, and a correct height of 1 mm allowed us to achieve values close to 1.

### 4.6.1 Mesh refinements

For the investigation of tip-tip interaction and tip vortex evolution, refinements [46,47,50,51] were generated in the geometry to create zones with higher cell density, better capturing the turbulent structures of interest.

- *Ring refinement*: this includes the final part of the blade, the tip. The length, starting from the sliding mesh, extends 2% of $D$ towards the tip and 2% of $D$ outside the sliding mesh.

- *Wake refinement*: these are hollow cylinders whose length extends from 60% of the tip radius $R$ to the exterior of the sliding mesh. The length extension is $3D$.

- *Cake refinement*: this refinement is positioned inside the hollow cylinders to best capture the wake under the propeller. The length extension is $1D$.

Everything is included in Figure 4.5 and the parameters used are listed in Table 4.2.

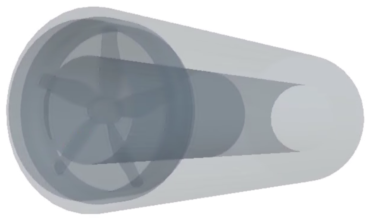

Figure 4.5: *Mesh refinements*

| Custom controls (target surface size %) | Fluid mesh | Rot mesh |
|---|---|---|
| Wake refinement | 0.3 | 0.3 |
| Ring refinement | 0.2 | 0.2 |
| Cake refinement | 0.3 | 0.3 |
| Domain | 200 | |
| External cylinder | 1.5 | |
| Propeller's surface | | 0.3 |
| Rotating region (RotInlet, RotOutlet, RotSide) | 0.3 | 0.3 |

Table 4.2: *Custom Controls*

### 4.6.2 Coarse and refine mesh

To achieve a proper mesh with the correct number of cells and computational cost, a coarse mesh was first created. This less refined mesh provided an initial visualization and allowed for further refinements in necessary areas to capture the tip vortex, represented in Figures 4.6a and 4.6b.
The coarse mesh had a different base size $BS$ and lower computational cost to observe the mesh generation behavior, as seen in Table 4.3.

| | Fluid mesh | Rot mesh |
|---|---|---|
| Base size | 1.2 | 1.2 |
| Target surface size | 200 | 0.3 |
| Minimum surface size | 0.1 | 0.1 |
| Number of prism layers | 15 | 15 |
| Prism layer stretching | 1.3 | 1.3 |

Table 4.3: *Coarse mesh*

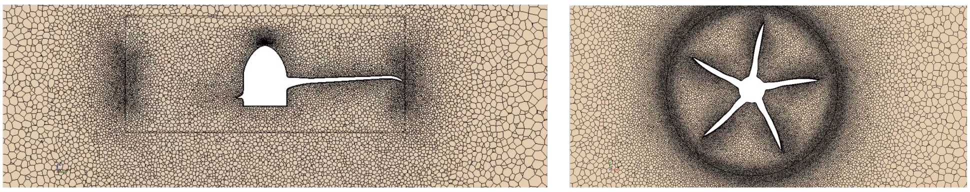

(a) *X-Axis view of the coarse mesh* (b) *Z-Axis view of the coarse mesh*

Figure 4.6: *Coarse mesh*

From the coarse mesh, valuable observations were derived to better adapt the refined mesh for accurate simulation and to refine the appropriate points for the tip vortex generation and evolution.

| | Fluid mesh | Rot mesh |
|---|---|---|
| Base size | 0.5 | 0.5 |
| Target surface size | 200 | 0.3 |
| Minimum surface size | 0.1 | 0.1 |
| Number of prism layers | 15 | 15 |
| Prism layer stretching | 1.3 | 1.3 |

Table 4.4: *Refine mesh*

The number of cells between the two meshes is different, as one uses a coarser resolution before transitioning to a refined mesh, with a higher number of cells and a significant computational cost, as shown in Table 4.5.

| | Fluid mesh | Rot mesh | Total cells |
|---|---|---|---|
| Coarse mesh | 4.25 M | 1.26 M | 6 M |
| Refine mesh | 28.7 M | 5 M | 32 M |

Table 4.5: *Number of cells*

The refined mesh, in Figures 4.7a and 4.7b, on the other hand, features smaller

cell sizes compared to the coarse mesh to better capture the generated turbulent structures.
An increase in the number of cells results in a higher computational cost for the simulation. It is noted that the considerable increase in the number of cells and higher accuracy have allowed for a smooth interface between the internal and external rotating regions. This is necessary to achieve satisfactory results in the simulation when the mesh rotates

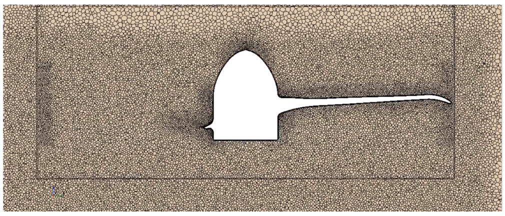

(a) *X-Axis view of the refined mesh*

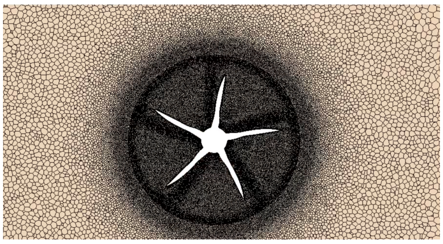

(b) *Z-Axis view of the refined mesh*

Figure 4.7: *Refine mesh*

**Mesh interface** Next, the continuity of the mesh at the interface is analyzed for both velocity magnitude and Z-velocity, highlighting the consistency of values across the cells and their smoothness, as seen in Figures 4.8a and 4.8b. This assessment is crucial as it confirms the absence of numerical artifacts in the mesh structure, which could otherwise compromise the accuracy of the numerical results.

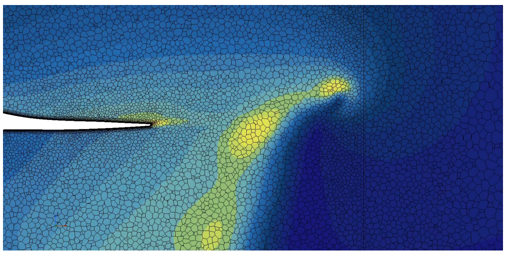

(a) *Velocity Magnitude view*

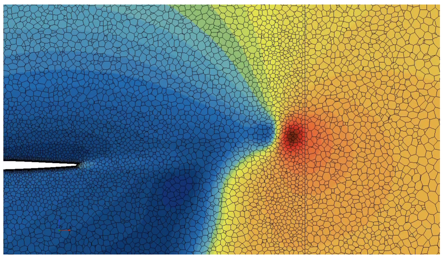

(b) *Z-Velocity view*

Figure 4.8: *Mesh interface*

## 4.7 Side-by-side mesh

For the side-by-side mesh configuration in Star-CCM+, the distance between the respective sliding meshes containing the two VX4 propellers is $2\%D$
The geometry was designed considering a distance of $\frac{2\%D}{3}$, between the tip of the

first propeller and its sliding mesh, another $\frac{2\%D}{3}$, between the two sliding meshes, and the last third for the second propeller and its sliding mesh.
The mesh structure was built with the same philosophy as the mesh for the single propeller. On this occasion, there are two sliding meshes presented in Figures 4.9a and 4.9b, to accommodate the rotation of the propellers, one for each propeller. The custom control refinements previously defined are applied to both reference sliding meshes.
The domain surrounding the two propellers is a single large bullet-shaped domain, within which there is a single outer rectangle that encloses all the various refinements and sliding meshes.
The issue at the sliding interface was resolved by achieving an appropriate cell size between the inner and outer parts of the two sliding meshes to avoid problems during rotation.

| | Fluid mesh | Rot1, Rot2 mesh |
|---|---|---|
| Base size | 0.5 | 0.5 |
| Target surface size | 200 | 0.3 |
| Minimum surface size | 0.1 | 0.1 |
| Number of prism layers | 15 | 15 |
| Prism layer stretching | 1.3 | 1.3 |

Table 4.6: *Side-by-side mesh*

The total number of cells has significantly increased this time due to the presence of two rotating zones. The refinement and cell density have been maintained in line with the approach used for the single propeller.

| | Fluid mesh | Rot1, Rot2 mesh | Total cells |
|---|---|---|---|
| Side-by-side mesh | 52 M | 9 M | 62 M |

Table 4.7: *Number of cells*

The boundary conditions chosen are the same as for the single propeller for hover configuration and forward flight configuration. The physical model used is also the same as previously indicated for the single propeller simulation. It was necessary to define two different rotational movements for each propeller, each around its own axis. Therefore, two additional reference systems had to be defined, in addition to the one already defined by Star-CCM+.

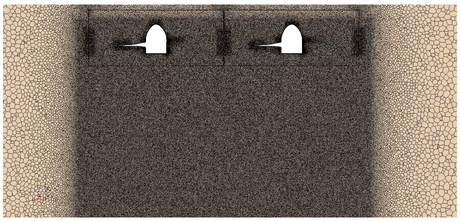

(a) *Y-Axis view of the side-by-side mesh*

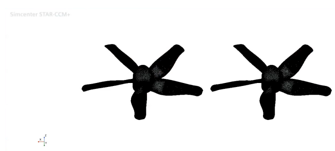

(b) *Side-by-side configuration*

Figure 4.9: *Side-by-side mesh*

## 4.8 FLOWUnsteady setup simulation

FLOWUnsteady is an open-source framework based on the reformulated vortex particle method [47,52]. Per generare la geometria della pala VX4, occorre passare per gli step di definizione del propeller.

### 4.8.1 Propeller definition

As the first step, the software requires a .csv file that constitutes the geometry of the rotor. This file, as seen in Figure 4.10, will contain various .csv files that define the different geometric parameters of the rotor and the blade.

| | A | B | C | D |
|---|---|---|---|---|
| 1 | property,file,description | | | |
| 2 | Rtip,0.13, (m) Radius of blade tip | | | |
| 3 | Rhub,0.022, (m) Radius of hub | | | |
| 4 | B,5, Number of blades | | | |
| 5 | blade,VX4blade.csv, Blade file | | | |
| 6 | | | | |

Figure 4.10: *File rotor.csv*

To run the simulation, FLOWUnsteady uses the Julia environment, where various packages needed to run the input code are installed.
Therefore, you need to create an input script in .jl format, Figure 4.11, with all the necessary parametric specifications to correctly execute the simulation.

```
# Generate rotor
    rotor = uns.generate_rotor(rotor_file;
                                        pitch=pitch,
                                        n=n, CW=CW, blade_r=r,
                                        altReD=[RPM, J, mu/rho],
                                        xfoil=xfoil,
                                        ncrit=ncrit,
                                        data_path=data_path,
                                        verbose=false,
                                        verbose_xfoil=false,
                                        plot_disc=false
                                        );
```

Figure 4.11: *Script generate rotor*

All input parameters are defined by the user in the Julia file. They include:

- $n$ : number of blade elements needed to discretize the blade..
- $CW$: indicates whether the propeller rotation will be clockwise or counter-clockwise.

- $r$: parameter that discretizes the elements
- $RPM$: indicates the propeller's rotation speed
- $J$: defines the advance ratio value
- $\mu$, $\rho$ : define the dynamic viscosity and density
- *xfoil*: this parameter indicates whether the xfoil package should be used during the simulation
- *ncrit*: indicates the turbulence criterion for xfoil
- *data path*: specifies the path to read the .csv files needed to recreate the rotor and blade geometry

To generate the correct geometry, it is necessary to have well-defined .csv files for the rotor and the blade, and to insert them into the FLOWUnsteady database so that when they are called in the input script, they will be selected from the database The FLOWUnsteady database folder consists of two sub-folders:

- *airfoils*
- *rotors*

It is important to correctly insert the various .csv files, Figure 4.12 needed to define the geometry into the appropriate sub-folders.

| | A | B | C | D | E | F |
|---|---|---|---|---|---|---|
| 1 | property,file,description | | | | | |
| 2 | chorddist,VX4chorddist.csv, Chord distribution | | | | | |
| 3 | pitchdist,VX4pitchdist.csv, Pitch distribution | | | | | |
| 4 | sweepdist,VX4sweepdist.csv, LE sweep distribution | | | | | |
| 5 | heightdist,VX4heightdist.csv, LE height distribution | | | | | |
| 6 | airfoil_files,VX4airfoils.csv, Airfoil distribution | | | | | |
| 7 | spl_k,5, Spline order | | | | | |
| 8 | spl_s,5.0e-6, Spline smoothing | | | | | |

Figure 4.12: *File blade.csv*

The various .csv files related to the geometry of the propeller should be placed in the *rotors* sub-folder, while the files related to the airfoils should be placed in the *airfoils* sub-folder.
The *blade.csv* file contains a series of files related to the blade geometry. These files must be placed in the *rotors* folder and include:

- *chorddist.csv*
- *pitchdist.csv*
- *sweepdist.csv*

- *heightdist.csv*

The last two lines refer to the order of the spline and the smoothing used for the blade generation. The file *chorddist.csv* contains data regarding the chord distribution. The first column refers to the non-dimensional radial position $\frac{r}{R}$, while the second column has the non-dimensional chord $\frac{c}{R}$ of that radial position.
The same column positioning philosophy applies to the other files related to the rotor blade geometry. The file *pitchdist.csv* contains data regarding the pitch distribution, which is the angle of attack relative to the plane of rotation.
The file *sweepdist.csv* contains data accounting for the inclination of the aerodynamic profile relative to the axis of rotation.
*Heighdist.csv* contains data on the height distribution between the aerodynamic profile and the plane of rotation.
Instead, the file *airfoils.csv* contains the airfoil files corresponding to each radial position. This includes the contour files of the wing profile and the polar files. This file must be placed in the airfoils sub-folder.
Once all the files are correctly placed in the database, the rotor can be generated along with the other parameters.

### 4.8.2 Simulation definition

| Parameter | Mid-low fidelity | Mid-high fidelity | High fidelity | Description |
|---|---|---|---|---|
| `n` | `20` | `50` | `50` | Number of blade elements per blade |
| `nsteps_per_rev` | `36` | `72` | `360` | Time steps per revolution |
| `p_per_step` | `4` | `2` | `2` | Particle sheds per time step |
| `sigma_rotor_surf` | `R/10` | `R/10` | `R/80` | Rotor-on-VPM smoothing radius |
| `sigmafactor_vpmonvlm` | `1.0` | `1.0` | `5.5` | Expand particles by this factor when calculating VPM-on-VLM/Rotor induced velocities |
| `shed_starting` | `false` | `false` | `true` | Whether to shed starting vortex |
| `suppress_fountain` | `true` | `true` | `false` | Whether to suppress hub fountain effect |
| `vpm_integration` | `vpm.euler` | RK3* | RK3* | VPM time integration scheme |
| `vpm_SFS` | None† | None† | Dynamic‡ | VPM LES subfilter-scale model |

- **RK3:* `vpm_integration = vpm.rungekutta3`
- †*None:* `vpm_SFS = vpm.SFS_none`
- ‡*Dynamic:* `vpm_SFS = vpm.SFS_Cd_twolevel_nobackscatter`

Figure 4.13: *Solver parameters*

Based on the solver parameters set in the simulation's input script, the number of particles generated for the simulation varies. An increase in the number of particles leads to higher fidelity in the simulation, as represented in Figure 4.13.
A number of particles around 100 thousand indicates a low-mid fidelity simulation, a number of particles over 200 thousand indicates a mid-fidelity simulation, and a number of particles over one million indicates a high-fidelity simulation, in which

vortices are visualized with greater accuracy. In the simulation script, parameters can be set to better capture turbulence and suppress numerical fluctuations that could cause the simulation to fail to converge. Depending on the desired fidelity of the simulation, various parameters that model turbulence can be adjusted.
The output files contain load distributions, values of $C_T$, $C_Q$, $\eta$ and the generated particle fields.
Additional simulation scripts are provided to simulate the velocity and vorticity flow fields and for the side-by-side configuration.
Parameters can be defined based on the desired distance between the two rotors and the grid discretization to be achieved.

# Chapter 5

# CFD results and Analysis

This chapter presents the results of CFD simulations conducted for both hover and forward flight configurations, covering both single propeller and side-by-side setups. The first research question of this thesis is addressed through detailed graphs and examples, which elucidate the underlying aerodynamic phenomena.

## 5.1 Isolated propeller VX4

### 5.1.1 Flow field of an isolated propeller

To understand the aerodynamic phenomena that define the side-by-side configuration and their impact on performance, it is crucial to first analyze the flow fields of a single propeller and compare the differences between the hover and forward flight conditions. The flow field of the VX4 single propeller, obtained from the uRANS simulation on Star-CCM+, is presented. The simulation settings parameters were as follows:

- *time step* = 2.77777777778e-5 s
- *maximum steps* = 3600
- *inner iterations* = 10
- *number of revolutions* = 10
- *RPM* = 6000

These simulation parameters allowed achieving an appropriate $CFL$ number, combined with the previously refined mesh size, to capture the turbulent structures formed by the propeller's rotation. To ensure the development of the wake, 10 revolutions were considered with a small time step to account for the tip vortex

generation phenomena.
First, a general overview of the wake structure of a single propeller in both configurations is presented, providing insight into wake evolution and the characteristics of velocity and vorticity fields in hover and forward flight conditions.

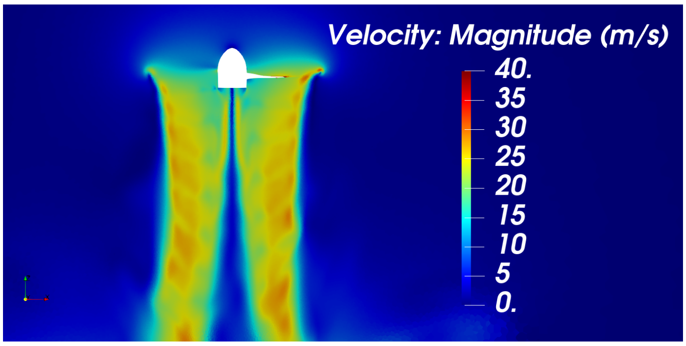


Figure 5.1: *Hover configuration: Velocity Magnitude (m/s)*

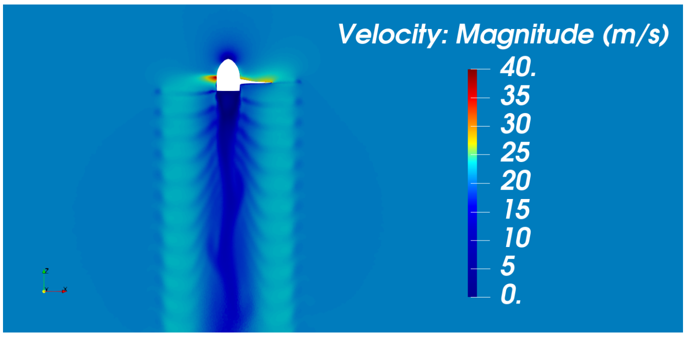


Figure 5.2: *Forward Flight configuration: Velocity Magnitude (m/s)*

As illustrated in the flow field Figures 5.1 and 5.2, the evolution of the flow differs between the hover and forward flight configurations.
In the hover configuration, the flow velocity is $V_\infty = 0$, meaning that only the blade rotation generates the wake. The flow is primarily axial and symmetric, exhibiting a higher contraction rate. Vortices formed at the blade tip quickly accelerate and contract. In this case, the wake is directed downward, producing thrust and forming a highly concentrated region. Strong velocity gradients develop at the wake boundary, where the accelerated induced flow interacts with the nearly stationary surrounding air. In hover, viscous forces act locally, causing energy dissipation and leading to a concentrated but less energetic wake over distance. Inertial forces play a minor role in this scenario.
In the forward flight configuration, the incoming flow velocity is $V_\infty = 20.8\ m/s$ directed towards the propeller along the negative $Z$-axis . The advance ratio is set

to $J = \frac{V}{nD} = 0.8$, representing high advance ratio conditions.
The flow field in this configuration differs significantly from the hover case. The wake is tilted backward and takes on an asymmetric shape. Vortex concentration is lower, and the wake extends further in the longitudinal direction behind the propeller, showing minimal contraction. A portion of the thrust is generated by accelerating an already moving air mass, resulting in lower wake velocities compared to the surrounding flow. Inertial forces, driven by the vehicle's forward motion, become more significant, leading to an elongated wake and periodic tip vortex formation. Viscous forces have a reduced influence on the overall wake structure.

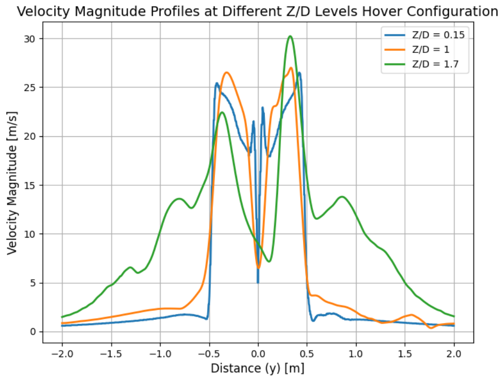


(a) *Hover*

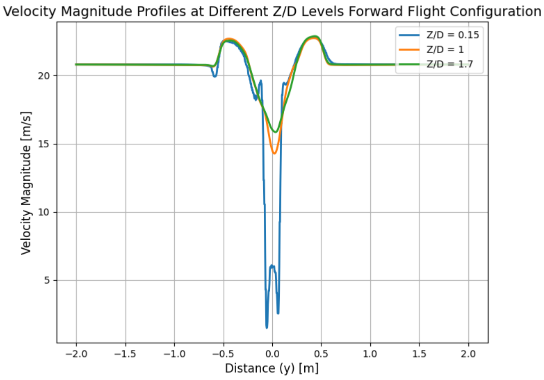


(b) *Forward Flight*

Figure 5.3: *Velocity profile Hover and Forward Flight*

From the analysis of velocity profiles at different $Z/D$ sections shown in the Figure 5.3a and Figure 5.3b, the differences in wake behavior between the two configurations become evident.
In the hover configuration, velocity profiles initially show $V = 0$, as the surrounding air is stationary. As the wake develops, two pronounced lateral peaks emerge, corresponding to tip vortices that indicate strong velocity gradients at the wake boundary. With increasing $Z/D$, the wake evolves rapidly, expanding significantly and dissipating energy. In the central region of the velocity profiles, oscillations suggest turbulence and flow interaction, which are characteristic of hover conditions. The wake appears unstable and diffused, with well-defined vortex structures along its edges.
In forward flight, the velocity profiles reveal a wake that is more elongated and narrow. Outside the wake, the imposed freestream velocity is clearly visible, while a velocity deficit forms at the central core.
As $Z/D$ increases, this velocity depression gradually diminishes, approaching the

freestream velocity, while the wake progressively spreads. Compared to the hover case, wake contraction is significantly reduced, with less acceleration of the flow and a noticeable deceleration at the central core.

### 5.1.2 Vorticity field single propeller

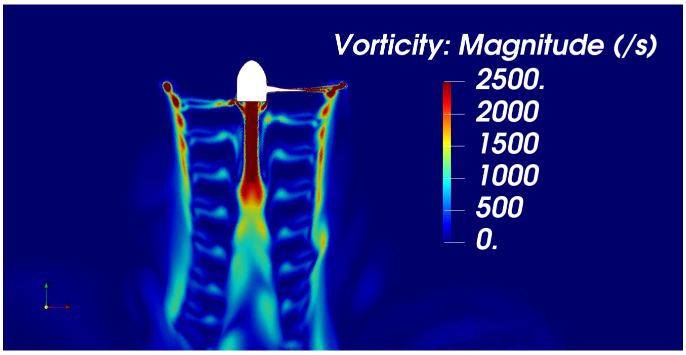


Figure 5.4: *Hover: Vorticity Magnitude (/s)*

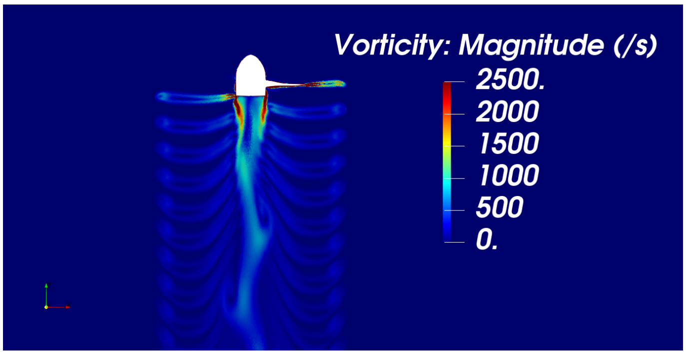


Figure 5.5: *Forward Flight: Vorticity Magnitude (/s)*

The vorticity visualizations highlight the main vortex structures that characterize the two configurations. In both cases, the propeller generates a vortex system, but the geometry and interaction of these vortices differ significantly. .
In hover, displayed in Figure 5.4 each propeller blade produces a tip vortex. These vortices gradually wrap into a wake that extends downward with strong contraction. A nearly cylindrical helical structure can be observed forming beneath the rotor. Under steady-state conditions [53] studies have shown that some vortices can persist near the propeller, potentially leading to vortex re-ingestion by the rotor. This phenomenon could generate unsteady effects that affect performance.
In forward flight, Figure 5.5, vorticity is generated similarly with each blade pas-

sage, but the entire vortex structure is carried downward by the free-stream flow and inertial forces. Just behind the propeller, the tip vortices of each blade move away at an angle rather than forming a vertically stacked pattern. The three-dimensional shape of the wake evolves into an elongated helical spiral, where tip vortices remain distinct even at large distances from the propeller.
In summary, the wake in hover exhibits stronger contraction, higher concentration, and lower energy dissipation at a distance. In forward flight, the wake is more elongated and less concentrated, with inertial forces playing a dominant role in its development.

The following sections will address the first research question, focusing on performance and the aerodynamic mechanisms that influence thrust.

## 5.2 Thrust distribution and trend

The analysis compares the thrust behavior of a single propeller with that of propellers in the side-by-side configuration, highlighting the differences between the two setups and examining the thrust distribution across the individual blades.

### 5.2.1 Hover conditions

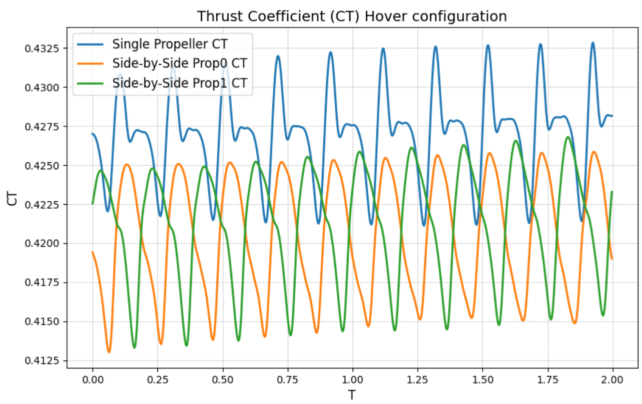


Figure 5.6: *$C_T$ distribution hover configuration*

The graph in Figure 5.6 presents the thrust coefficient $C_T$ on the $y$-axis calculated as $C_T = \frac{T_h}{\rho n^2 D^4}$ where $T_h$ is the thrust, $\rho$ is the air density, $n$ is the rotational speed of the propeller and $D$ is the diameter of the propeller. The $x$-axis represents the

normalized time $T$, which corresponds to the time scaled by the rotational period. It is expressed as $T = \frac{t}{t_+}$, where $t$ is the simulation time and $t_+$ is the revolution period associated with the rotation rate used in the simulations.
The analysis considers the last two propeller revolutions $(8 - 10)$ to evaluate the convergence behavior of the thrust and to avoid the transient effects of the initial revolutions. Observing the trends for both propellers, a characteristic thrust drop is evident in the side-by-side configuration [54]. A comparison between the single propeller and the side-by-side configuration shows a 2% decrease in thrust, indicating that the proximity and interaction between the two propellers negatively impact performance. The following sections will examine the aerodynamic effects responsible for this performance loss.
According to the literature [55] thrust fluctuations in the side-by-side configuration are greater than in the single-propeller case due to interactions between the two units, which generate flow regions with increased induced velocities and localized turbulence. However, when comparing the mean thrust values, both configurations remain within the same order of magnitude (0.64% for the single propeller and 0.88% for the side-by-side configuration) as seen in Table 5.1.
For the single propeller in hover, these pronounced fluctuations may indicate that the short spacing between consecutive tip vortices leads to blade reingestion of undissipated vortices, causing blade unsteadiness. Another possibility is that the computational mesh introduces numerical artifacts at the interface between the stationary and rotating regions, which, after several revolutions, may start to affect the results.

| Hover | $C_T$ | $T$ $[N]$ | Fluctuation (%) |
|---|---|---|---|
| Single propeller | 0.427 | 23.02 $[N]$ | 0.6% |
| Side-by-side (Prop0) | 0.418 | 22.6 $[N]$ | 0.88% |
| Side-by-side (Prop1) | 0.42 | 22.7 $[N]$ | 0.84% |

Table 5.1: *Thrust values hover configuration*

To investigate the effect of this pronounced unsteadiness observed in the last two revolutions, we analyzed the thrust generated by each propeller blade for both the single-propeller hover case and the side-by-side configuration.

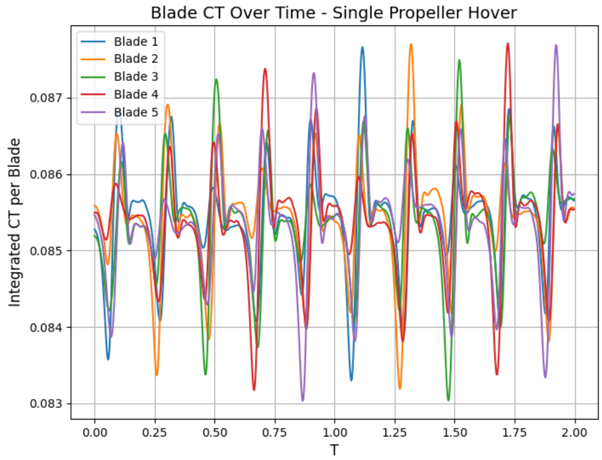


Figure 5.7: *Differents Blades $C_T$: Single propeller hover*

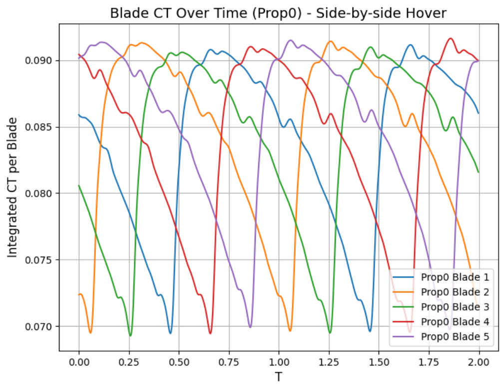


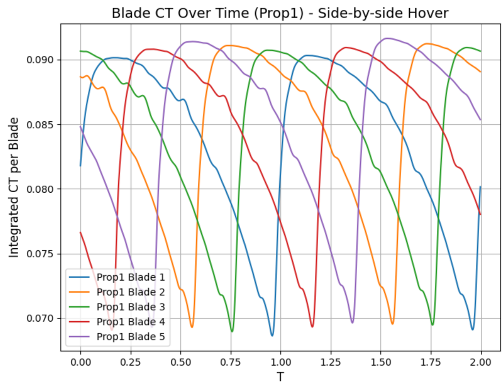


Figure 5.8: *$C_T$ Prop0 Side-by-side hover* Figure 5.9: *$C_T$ Prop1 Side-by-side hover*

The peaks observed in the thrust of the single propeller blades Figure 5.7 exhibit periodicity, suggesting that the fluctuations may result from the blades periodically interacting with a vortex generated by their own rotation. A further analysis of the tip vortex trajectory will provide additional insight into this phenomenon.
In the side-by-side configuration, each blade encounters the wake of the other blades once per revolution, leading to oscillations in the thrust graph, where an alternating up-and-down pattern is visible. This periodic behavior appears twice in the last two revolutions as seen in Figure 5.8 and in Figure 5.9. The five narrower peaks observed in the graph correspond to the interaction of each blade with the vortex at specific points during its rotation.

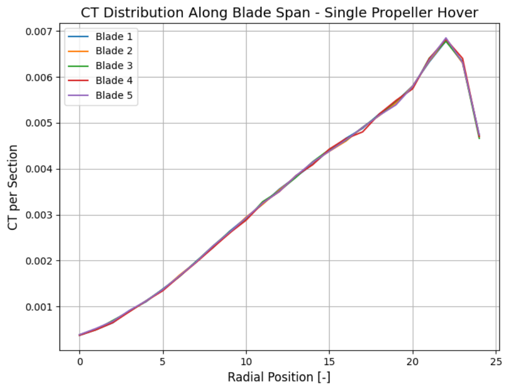


Figure 5.10: $C_T$ *distibution along blade span- Single propeller hover*

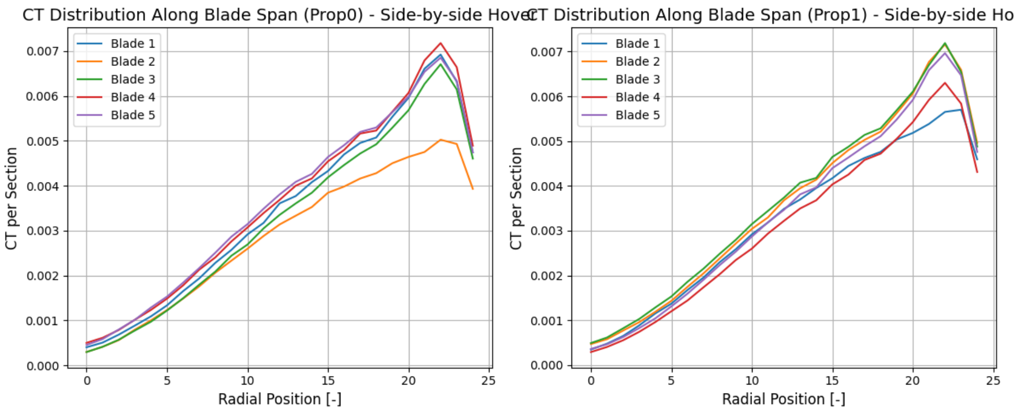


Figure 5.11: $C_T$ *distibution along blade span - Side-by-side hover*

As seen in the thrust distribution graphs along the blade in Figure 5.10, in the single-propeller case, all blades exhibit the same behavior, as the propeller operates freely in still air. The thrust curves for all blades overlap, indicating the absence of external aerodynamic disturbances affecting individual blades. The thrust coefficient $C_T$ gradually increases along the blade span, reaching a peak around $80\% - 90\%$ of the radial length before dropping sharply near the tip.

In contrast, in the side-by-side configuration Figure 5.11, rotor interaction effects become evident, causing variations in thrust distribution among the blades. In $Prop_0$, blade 2 exhibits a significantly lower $C_T$ value compared to the other blades, suggesting a disturbance caused by the proximity of the second propeller. In $Prop_1$, interaction effects with the other propeller are still present, unlike in the single-propeller case, but they are less pronounced than in $Prop_0$.

This graph was generated by discretizing the blade span into 25 elements and calculating the thrust distribution across these elements.

### 5.2.2 Forward Flight conditions

Next, the thrust graphs for the forward flight case are analyzed. Since the flow is less accelerated compared to the hover case, it generates significantly lower thrust.

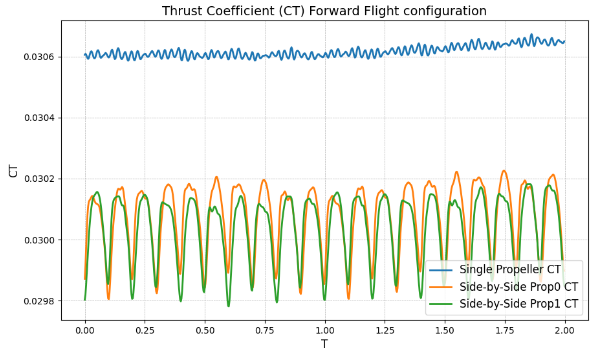


Figure 5.12: *$C_T$ distribution Forward Flight configuration*

Some information from the manufacturer Vertical Aerospace identifies the $VX4$ propeller as not specifically designed for forward flight. To improve its performance in this condition, a pitch angle is added to increase thrust production.
By examining the reference $C_T$ values for both the single-propeller and side-by-side configurations in Figure 5.12, it becomes evident that the generated thrust is very low. In a way, it is as if the propeller is spinning without effectively producing thrust.

| Forward Flight | $C_T$ | $T$ $[N]$ | Fluctuation % |
|---|---|---|---|
| Single propeller | 0.0306 | 1.65 $[N]$ | 0.06% |
| Side-by-side prop0 | 0.03 | 1.62 $[N]$ | 0.36% |
| Side-by-side prop1 | 0.03 | 1.62 $[N]$ | 0.36% |

Table 5.2: *Thrust values Forward Flight configuration*

Analyzing the fluctuations, there is an increase in the percentage fluctuation in the side-by-side configuration, indicating that the mutual influence between the two propellers triggers unsteady fluctuations as seen in Table 5.2. However, in terms of its impact on the thrust coefficient ($C_T$), this does not lead to a significant change, as each propeller continues to generate very low thrust. .
This aligns with the fact that, in forward flight, the required thrust is lower since

the incoming airflow is already moving and does not need to be accelerated as much as in hovering. In the single-propeller case, it is observed that toward the end of the last revolution, thrust begins to increase. This suggests that the simulation may not have fully converged after 10 revolutions. Compared to the single-propeller thrust trend in hover, the thrust profile in forward flight does not exhibit fluctuations. This is because inertial forces transport vortices away, making it unlikely for a vortex to be re-ingested by the rotating propeller.
In the side-by-side configuration, the fluctuating thrust trend highlights the minimum peaks, which correspond to blade interactions between the two propellers.

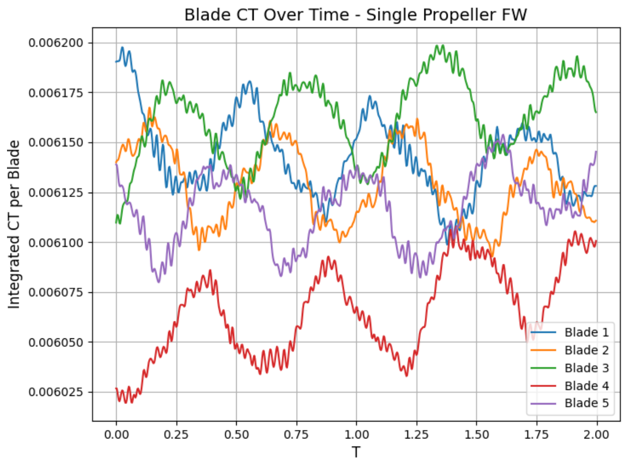


Figure 5.13: *Differents Blades $C_T$: Single propeller FF*

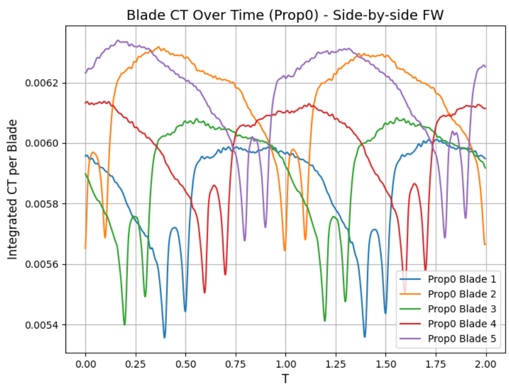


Figure 5.14: *$C_T$ Prop0 Side-by-side FF*

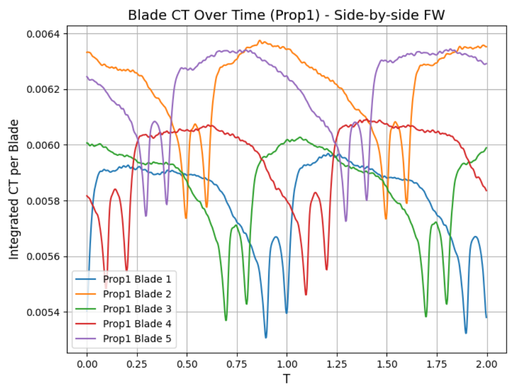


Figure 5.15: *$C_T$ Prop1 Side-by-side FF*

The thrust trends in the single-propeller and side-by-side forward flight configura-

tions exhibit clear differences. In the single-propeller case Figure 5.13, all blades follow a similar pattern, with regular oscillations.
In the side-by-side configuration Figure 5.15 and Figure 5.14, interactions between the blades of the two propellers become evident, particularly at the points of minimum thrust, where a blade encounters the wake of the other. This interaction causes a noticeable dip in thrust. Between these interactions, during the rising phases, the blade moves through undisturbed airflow, allowing thrust to increase until it meets the wake again.
The oscillations in the side-by-side configuration are more pronounced and asymmetric due to uneven aerodynamic loading on the blades. This asymmetry results from disturbances in the airflow generated by the nearby propeller.

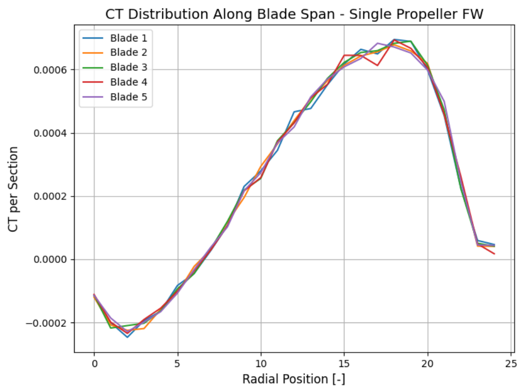


Figure 5.16: $C_T$ *distibution along blade span- Single propeller FF*

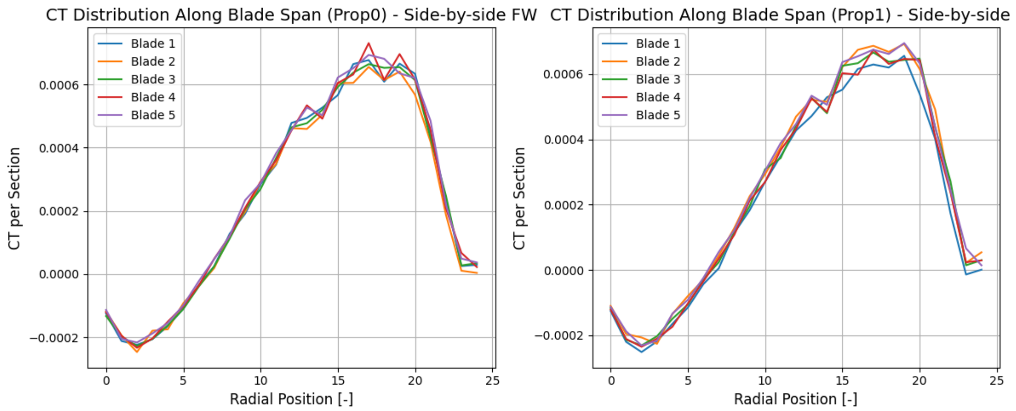


Figure 5.17: $C_T$ *distibution along blade span- Side-by-side FF*

The difference in thrust distribution along the blade span is minimal between the

single-propeller and side-by-side configurations. This reinforces the small variation observed in the total thrust produced by the single propeller compared to the propellers in the side-by-side setup.
In the single-propeller configuration Figure 5.16, the thrust curves of all blades are nearly overlapping, indicating a well-balanced aerodynamic load distribution. The peak $C_T$ occurs around $70\% - 80\%$ of the blade's radial length.
In the side-by-side configuration Figure 5.17, slight variations between the blades are observed, caused by the interaction between the wakes of the two rotors. These interactions can locally affect the thrust distribution along the blades.

### 5.2.3 Thrust disk distribution

This subsection focuses on the analysis of the azimuthal distribution of thrust over a disk. The generated disks represent both the azimuthal thrust distribution and the unsteady thrust. The latter is calculated as the thrust oscillation around the mean value, identifying interactions with vortices or blade passages. The methodology for calculating unsteady thrust is based on integrating the pressure over the blades. The blade is divided into small sections distributed along the span. At each time step, the local thrust force $T(\theta)$ on each patch is computed by integrating the pressure. This process generates a table of pressure values with time and azimuthal position as reference variables. The data are averaged over the considered rotor revolutions to obtain the mean thrust value at each point of the rotor disk. This step allows the reconstruction of the mean thrust disk $\overline{T}(\theta)$, representing the global thrust distribution under steady conditions. To isolate only the thrust variations $T'(\theta)$, the azimuthal mean component is removed for each patch along the blade span. The resulting unsteady thrust disk $T'(\theta) = T(\theta) - \overline{T}$ exclusively displays local thrust oscillations relative to the mean value, highlighting variations caused by vortex phenomena or wake interactions. A positive value indicates regions where the local thrust is temporarily higher than the mean, while a negative value corresponds to areas where the thrust is temporarily lower than the mean. Disks were generated for the single and side-by-side hover configurations, as well as for the single and side-by-side forward flight configurations, to evaluate how thrust oscillation appears in the interaction between the two rotors.

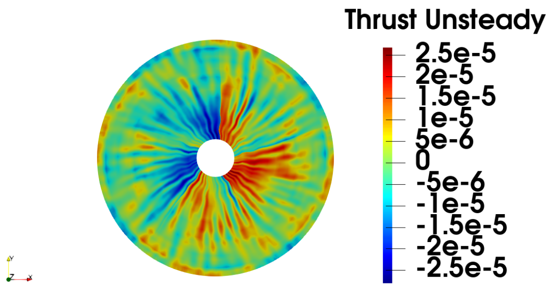


Figure 5.18: *Unsteady thrust distribution of single prop FF*

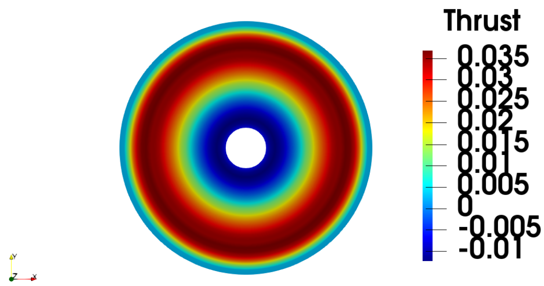


Figure 5.19: *Azimuthal distribution of thrust single prop FF*

The visualization of the thrust distribution aligns with the theoretical behavior of the propeller in forward flight. The load is evenly distributed azimuthally in Figure 5.19, indicating the absence of unsteadiness in this configuration. As seen in the unsteady thrust distribution Figure 5.18, the very small values suggest only numerical noise, making the unsteadiness in this case negligible

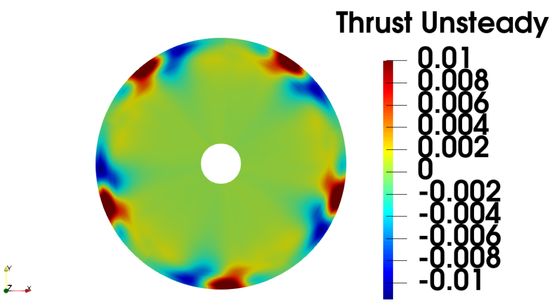


Figure 5.20: *Unsteady thrust distribution of single prop hover*

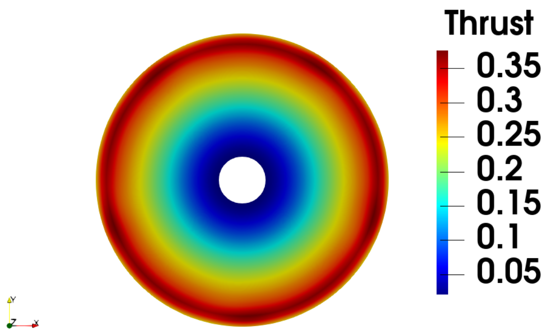


Figure 5.21: *Azimuthal distribution of thrust single prop hover*

In the hover case, the azimuthal thrust distribution is uniform along the azimuth but varies radially from the hub to the blade tip. The Figure 5.21 shows that at each radius, a certain level of thrust is generated. The central region near the hub exhibits lower values because the blade's peripheral velocity is lower, resulting in reduced loading. The blade tip, having the highest peripheral velocity, produces the greatest thrust. Regarding the unsteady shown in Figure 5.20, since the surrounding air is stationary, the flow is expected to be the same for each blade, leading to minimal azimuthal variations. The red and blue regions near the blades on the disk likely correspond to vortex phenomena, such as tip vortices or wake interactions, generated by the blades in hover. As there is no inertial force rapidly carrying the wake away, these vortices remain near the rotor plane for a certain period, causing local oscillations in the loading. In fact, when considering the unsteady thrust disk, there is no strong reason to observe such effects with the same number of blades that are as large in amplitude as those seen in the side by side case. This could be a motivation for future work using a higher fidelity model.

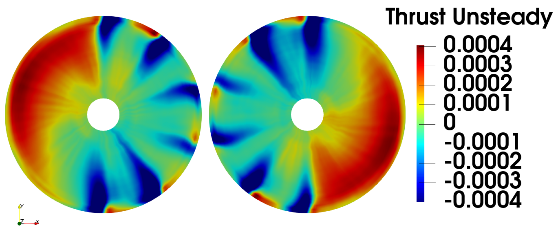


Figure 5.22: *Unsteady thrust distribution for side-by-side FF*

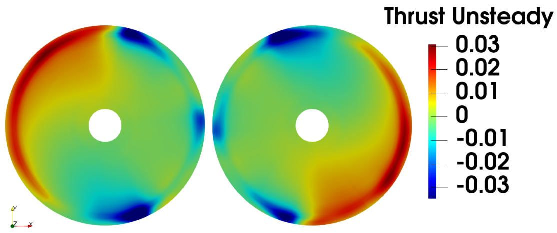


Figure 5.23: *Unsteady thrust distribution for side-by-side hover*

In the azimuthal distributions of unsteady thrust for the side-by-side configuration, the hover case, Figure 5.23, shows unsteadiness values that are two orders of magnitude higher than those in forward flight. This indicates that thrust fluctuations around the mean value in hover are significantly larger, driven by stronger aerodynamic interactions between the wakes of the two propellers. On the thrust disk, an interaction zone can be observed where the two descending airflow fields and the vortices from both rotors remain under the blades for an extended period, allowing further interaction. The close proximity of the two propellers results in negative thrust oscillations relative to the mean value, confirming that the thrust drop observed in the side-by-side configuration is caused by this interference. This trend of excessive unsteadiness caused by propeller interaction is observed in the literature in [9]. Conversely, on the side farther from the interaction, where no interference occurs, the blades generate higher thrust than the mean value. In forward flight Figure 5.22, unsteadiness values remain low, indicating that while a minimal influence exists due to the interaction between the two propellers, it has only a small impact on the overall thrust, as also observed in the thrust trend analysis. Due to the inertial force of the incoming flow, the interaction is present but has an almost negligible effect on the thrust generated by the propellers in the side-by-side configuration. Similarly, on the disk region closest to the minimum separation between the two propellers, negative thrust oscillations are present, though with much smaller values. On the opposite side, farther from the interaction, the oscillations are positive, and the blades generate higher thrust.

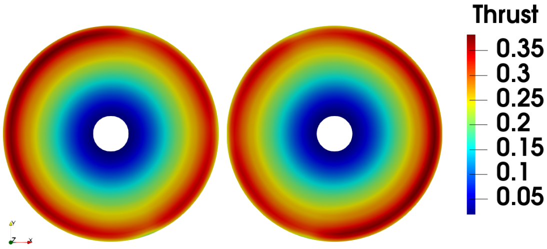


Figure 5.24: *Thrust distribution side-by-side hover*

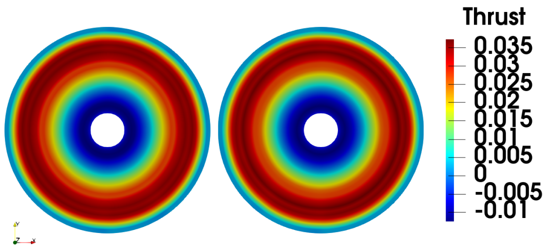


Figure 5.25: *Thrust distribution side-by-side FF*

The azimuthal thrust distributions reflect the behavior observed in the unsteady thrust disks. In the side-by-side hover case in Figure 5.24, the interaction between the two propellers leads to lower thrust values in the disk region near the minimum distance between the propellers, while higher thrust is observed in the areas farther from the interaction. In forward flight, shown in Figure 5.25, due to the presence of inertial effects from the incoming flow, the interactions between the propellers are nearly negligible. As a result, the azimuthal distribution remains entirely unaffected by this interaction.

## 5.3 Tip Vortex Trajectory and Z-Vorticity

This section addresses the first research question posed in the introduction of this thesis by analyzing the Z-vorticity scenes and the tip vortex trajectory, which provide valuable insights into the thrust drop observed in the hover side-by-side configuration.

### 5.3.1 Z-Vorticity

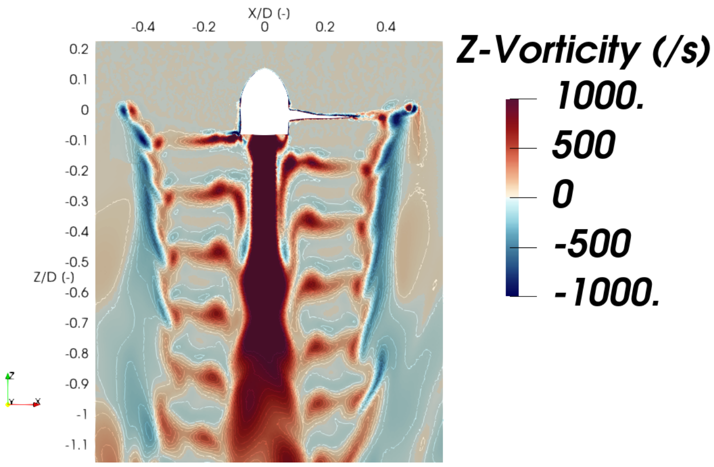


Figure 5.26: *Single propeller Hover: Z-Vorticity*

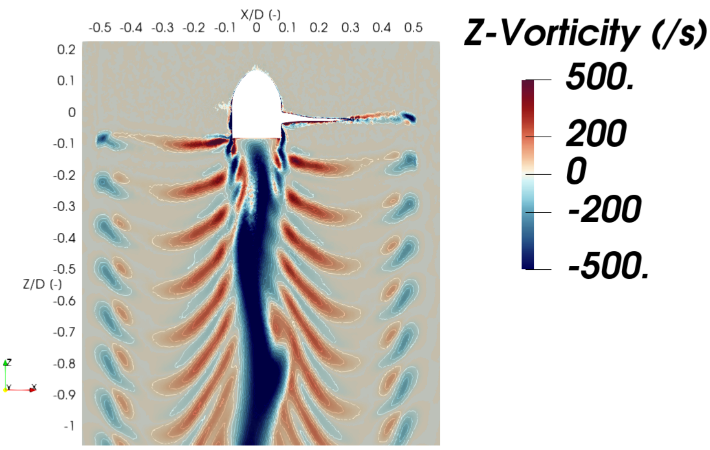


Figure 5.27: *Single propeller Forward Flight: Z-Vorticity*

To provide a physical explanation for the thrust drop observed in the hover side-by-side configuration, it is essential to first examine the flow physics of both configurations. For the single propeller in hover conditions, as discussed in the first section, thrust production is significantly higher than in forward flight. This is because the wake contraction is greater, leading to more accelerated tip vortices, which in turn generate high velocity gradients at the wake boundary.
In forward flight, wake contraction is much weaker, resulting in significantly lower thrust production. The key reason behind this reduced thrust lies in the fact that the flow in this configuration does not accelerate effectively. The influence of the freestream airflow is so strong that the propeller essentially operates with minimal efficiency, almost as if it were spinning without generating effective thrust.
The Z-vorticity scenes illustrate the differences between these two flow fields. In hover Figure 5.26, the wake appears more compact, where viscous forces dominate over inertial forces. The tip vortices are initially well-defined but gradually dissipate and merge into turbulent structures relatively close to the propeller.
In forward flight, as seen in Figure 5.27, the vortices are carried far away from the propeller and remain well-defined even at greater distances. This transport of vortices away from the propeller is primarily driven by the influence of inertial forces.

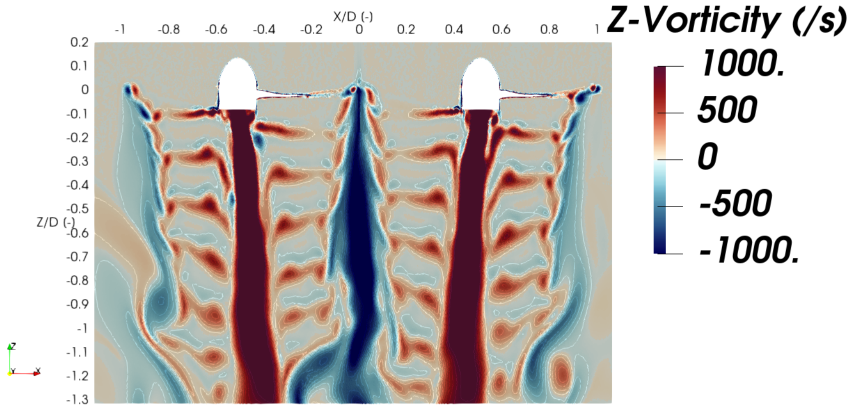


Figure 5.28: *Side-by-side propeller Hover: Z-Vorticity*

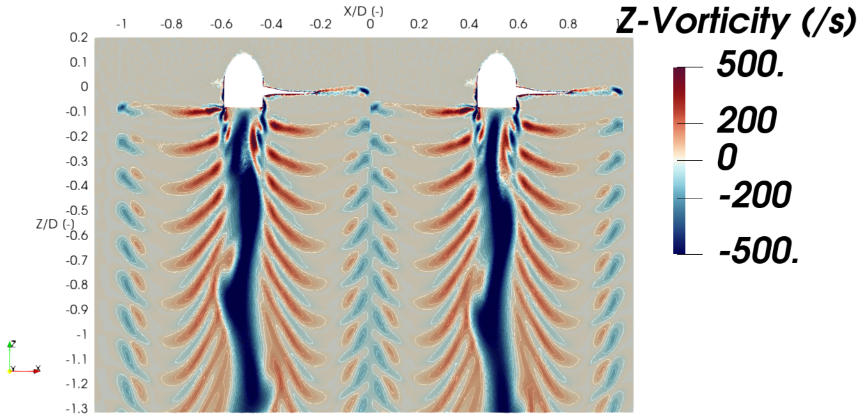


Figure 5.29: *Side-by-side propeller Forward Flight: Z-Vorticity*

In the side-by-side configuration, the vorticity field analysis provides valuable insights into the thrust drop observed in hover. During the ten revolutions in side-by-side hover in Figure 5.28, the interaction between the two propellers generates a central vortex region, known as the "fountain effect", where the flow reverses direction. At $Z/D = 1$, the tip vortices begin to merge into this central region, increasing interference. This stronger interaction between the tip vortices in hover is directly linked to thrust reduction, and this visualization effectively captures the dynamics behind this phenomenon. Questo trend viene confermata dalla letteratura [11, 12, 14].

Compared to the single-propeller case, the overall flow fields appear largely similar, both exhibiting significant wake contraction. However, the central vortex region, where tip vortices merge at a certain distance from the propeller, is a distinctive feature of the side-by-side configuration.

While one might logically expect greater flow acceleration in hover to result in higher thrust, the merging of tip vortices in the central region instead leads to a thrust drop and enhances unsteady fluctuations between the two propellers in the side-by-side setup.

In forward flight Figure 5.29, the interaction between the two propellers is minimal, and the wake remains mostly unaffected. Tip vortices are still generated by both propellers, but they are transported away with little to no interaction. This explains why the thrust drop in forward flight is significantly smaller, as the weaker vortex interaction in the side-by-side configuration has a negligible impact on overall performance.

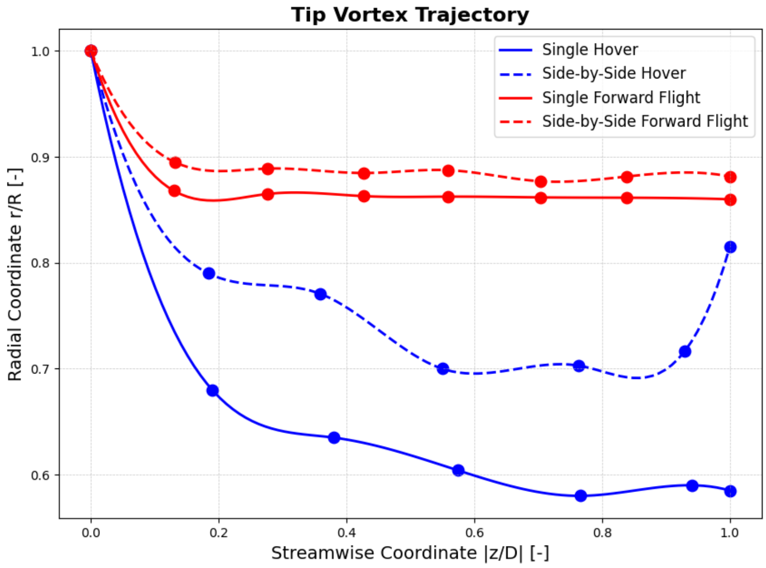


Figure 5.30: *Tip Vortex Trajectory*

In Figure 5.30, this graph further reinforces the previous explanation. The data represent the cores of the tip vortices along their trajectory across the four cases taken at the same final instant .

On the $y$-axis, the radial distance $r/R$ is represented, where $r/R = 1$ corresponds to the blade tip. The x-axis represents the vertical distance $Z/D$, tracking the wake evolution along its trajectory. In the hover configuration, a greater wake contraction is observed in the single-propeller case, while the side-by-side configuration shows reduced contraction. Since higher vortex contraction corresponds to increased thrust production, this further explains the thrust drop in the side-by-side case. In this configuration, at $Z/D = 1$ the vortices begin to shift radially toward the tip region, where the central turbulent zone is located, eventually merging with it. The key difference between the single and side-by-side configurations in hover, beyond the variation in wake contraction, is precisely the presence of this central turbulent region.

In forward flight, both the single and side-by-side cases exhibit linear trends, reflecting the minimal difference in thrust produced between the two configurations. Once again, the minimal interaction between tip vortices results in only a negligible impact on thrust.

## 5.4 Induced Velocity

To better highlight the aerodynamic phenomena responsible for the thrust drop in the hover side-by-side configuration compared to forward flight, this section analyzes the induced velocity generated by the propeller blades.
When the propeller rotates, it pushes a certain mass of air downward, creating a pressure and velocity difference across the rotor disk. The portion of velocity induced by the propeller, relative to the undisturbed flow, is crucial in determining thrust and propeller efficiency. Visualizing $V_{ind}$ helps to understand how the flow is accelerated by the propeller, compare the single-propeller case with the side-by-side configuration, and identify aerodynamic interference effects.

### 5.4.1 Meridional View of Induced Velocity

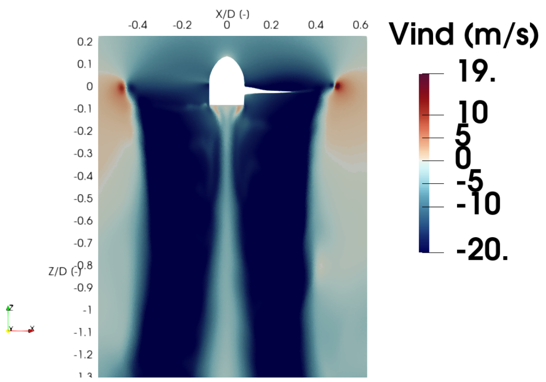


Figure 5.31: $V_{ind}$ *Single hover*

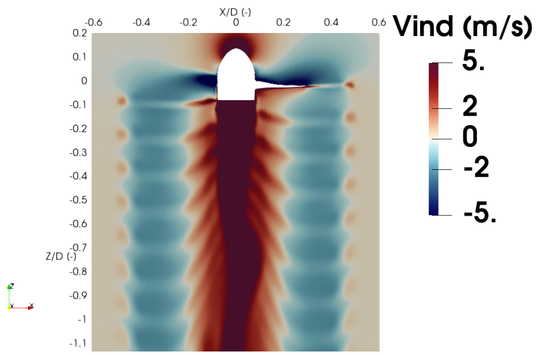


Figure 5.32: $V_{ind}$ *Single FF*

The induced velocity in these visualizations is analyzed differently for the two cases under consideration. In hover conditions, Figure 5.31, the induced velocity corresponds to the axial component of velocity since the surrounding air is stationary. This means the only velocity component considered is the one induced by the propeller blades, expressed as $V_{ind} = U_{axial}$.
In forward flight, Figure 5.32, however, the incoming freestream velocity also contributes to the total velocity above the propeller. To isolate the induced velocity, the freestream velocity must be subtracted from the axial velocity component, giving $V_{ind} = U_{axial} - V_{\infty}$. This allows for a clear assessment of the effect induced solely by the propeller blades. In hover, the induced effect of the propeller blades generates a wake with strong contraction, directed downward, indicating a high concentration of descending velocity in the central flow region. In forward flight, the propeller wake

exhibits a less intense downward velocity component. Additionally, tip vortices generated by the blades remain present at greater distances from the propeller, visible along the wake edges.

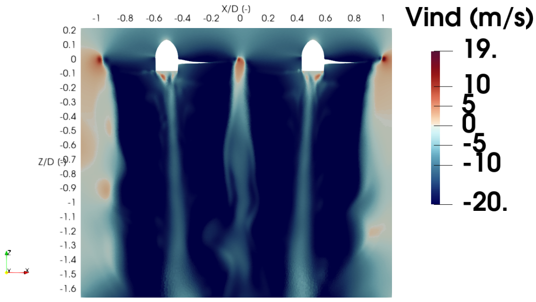


Figure 5.33: $V_{ind}$ *Side hover*

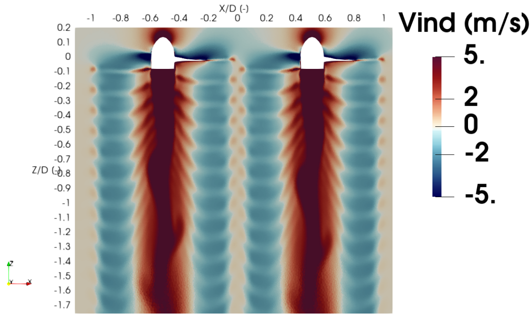


Figure 5.34: $V_{ind}$ *Side FF*

The thrust drop in the hover side-by-side configuration, as seen in Figure 5.33 occurs because, despite the high contraction rate indicating accelerated wake flow and increased thrust production, the wakes of the two propellers tend to merge. This interaction is particularly evident in the central turbulent region, where the wakes interfere with each other. This confirms that the primary cause of thrust loss and reduced efficiency is the mutual interaction of the two wakes.
In forward flight, shown in Figure 5.34, the wake remains largely unaffected, showing minimal changes. In the side-by-side configuration, the thrust produced by each propeller is nearly the same as in the isolated case. Although the meridional view suggests limited spacing between the tip vortices of the two propellers, this has little impact on thrust. The stronger inertial effects of the airflow reduce the tendency of the wakes to merge. Additionally, the two propellers continue generating vortices over long distances, with minimal interaction between them.

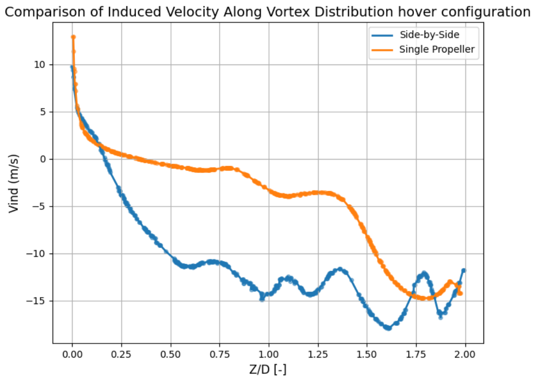


Figure 5.35: $V_{ind}$ *along* $Z/D$ *hover*

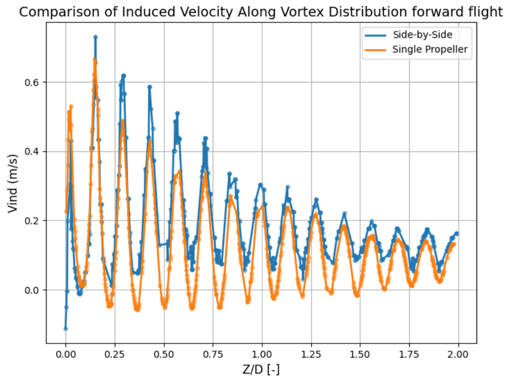


Figure 5.36: $V_{ind}$ *along* $Z/D$ *FF*

These two graphs were obtained by placing a vertical line at the blade tip in both configurations at the same final instant, at a radial distance of $r/R = 1$, and capturing the vortex distribution along the vertical $Z/D$ axis .
The trends in the two graphs show noticeable differences. The forward flight graph, presented in Figure 5.36, exhibits greater periodicity compared to the hover graph. This is because the vertical line was placed at the same position in both cases, and in forward flight, it precisely captures all the tip vortices as they form. In hover, Figure 5.35, due to stronger wake contraction, an ideal approach would require a curved line to accurately follow the contraction of the tip vortices.
As a result, in the forward flight graph, the peaks correspond to the vortex cores, while the regions between them show little to no vortex presence. This further emphasizes the minimal difference between the single and side-by-side configurations. In contrast, in the hover graph, the data represent the turbulent region that forms between the two propellers. The difference between the presence of this interaction in the side-by-side configuration and its absence in the single-propeller case is clearly visible.

### 5.4.2 Induced Velocity at different $Z/D$ sections

**Hover conditions** To further investigate the interaction between the two propellers, different $Z/D$ sections of the hover and forward flight cases are analyzed to highlight the regions of aerodynamic interference.

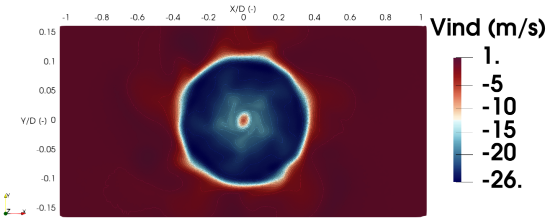


Figure 5.37: *Section $Z/D = -0.4D$ hover*

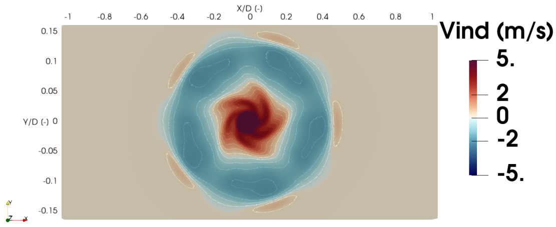


Figure 5.38: *Section $Z/D = -0.4D$ FF*

The presented scenes correspond to the $Z/D = -0.4D$ section, located below the propeller, and depict the single-propeller cases in hover and forward flight. In hover, represented in Figure 5.37, a predominant downward velocity component is observed, driven by wake contraction. Since the surrounding air is nearly stationary relative to the rotor, the wake develops in a vertical direction. At this wake height, the induced velocity is high to generate the required thrust.
In forward flight, displayed in Figure 5.38, the external tip vortices are more clearly visible. The lower values indicate a wake with less contraction and lower thrust production. The blue ring represents a descending flow, while the red region may indicate a tendency toward a slightly ascending velocity.

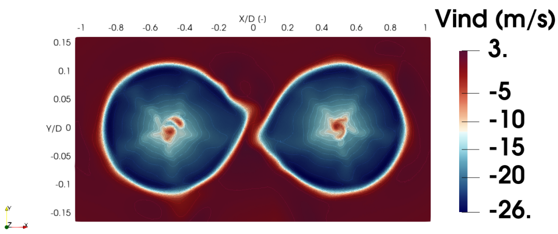


Figure 5.39: Section $Z/D = -0.2D$ hover

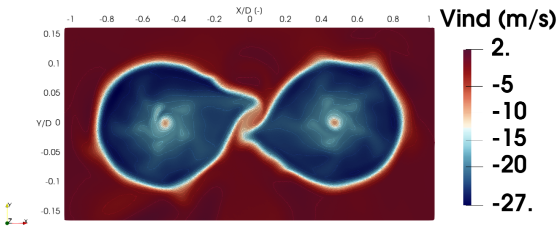


Figure 5.40: Section $Z/D = -0.4D$ hover

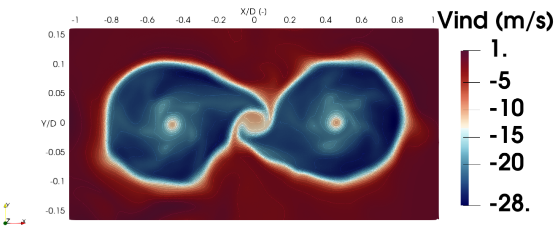


Figure 5.41: Section $Z/D = -0.7D$ hover

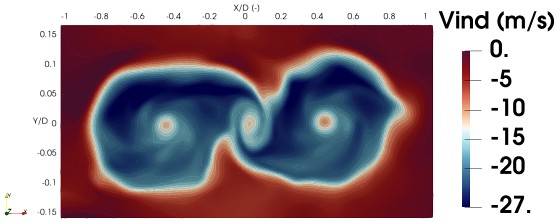


Figure 5.42: Section $Z/D = -1D$ hover

As seen in the top-view scenes of induced velocity in the hover side-by-side configuration represented in Figures 5.39, 5.40, 5.41 and 5.42, the wakes of the two propellers gradually merge as they evolve vertically. This merging process develops

progressively: in the initial part of the wake at $Z/D = -0.2D$ and $Z/D = -0.4D$, only an attraction between the wakes is visible, while at later stages, full merging occurs. At $Z/D = -1D$ the aerodynamic interaction becomes so strong that it generates a vortex at the center. This aerodynamic interference is undoubtedly the main cause of the thrust drop observed in hover, come visto anche in letteratura in [10, 12]. Despite the high contraction of the wakes, they tend to merge rather than remain separate.
This effect is also evident in the velocity profiles of the single-propeller and side-by-side cases, shown graphically in Figure 5.43. The single propeller configuration in the side-by-side case was mirrored symmetrically. The profiles of the isolated propeller and a single propeller from the side-by-side configuration were compared to highlight the effects caused by the interaction with the neighboring propeller, as in the paper [56]. As $Z/D$ increases, the central peak between the two propellers becomes increasingly negative, indicating stronger mutual induction. In contrast, the single-propeller velocity profile maintains a similar shape throughout. Beyond $Z/D = 0.7D$, as the hover wake remains compact and energetic, it starts to dissipate, creating a turbulent flow region. It can be observed that the peaks of the induced velocity profile of a single propeller taken from the side-by-side hover case gradually shift to the right compared to those of the single propeller as the wake sections evolve. This effect is due to the increasing interaction with the wake of the other propeller as the flow develops. At higher $Z/D$ distances, it becomes clear that the wakes tend to merge, causing the peak to move rightward. In the graphs, thanks to the zoomed-in view, this peak shift is noticeable, whereas it is less visually evident in the $V_{ind}$ field visualizations.

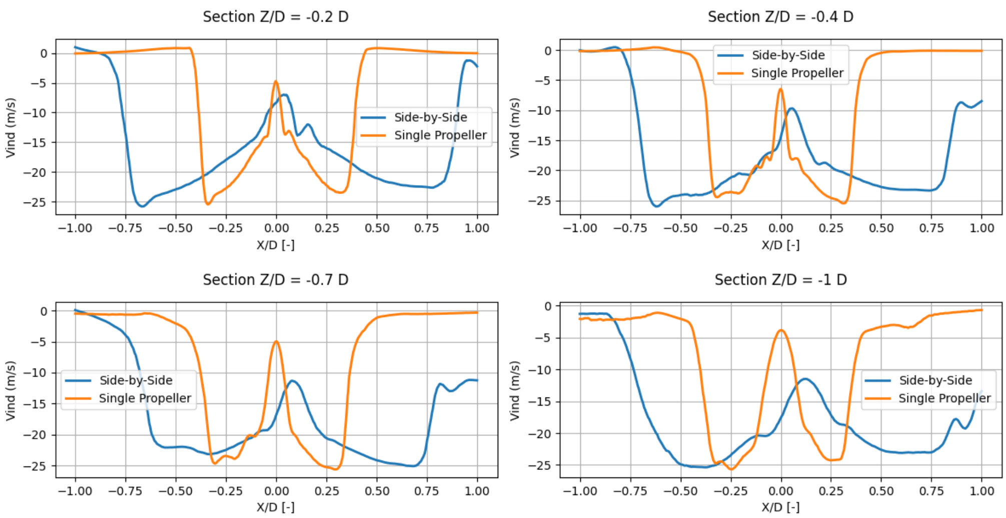


Figure 5.43: *Hover: Induced Velocity profiles single propeller vs side-by-side*

**Forward Flight conditions** The forward flight case clearly highlights that the thrust produced by the propellers remains almost the same in both the isolated and side-by-side configurations. As seen in the top-view visualizations of induced velocity in Figures 5.44, 5.45, 5.46 and 5.47, the spacing between the tip vortices generated by the two propellers is relatively small. However, the stronger inertial effect of the airflow prevents the wakes from merging. As $Z/D$ increases, the wake structure remains nearly unchanged, and the external tip vortices remain clearly visible, indicating that vortices continue to develop even at large distances from the propeller. By tracking the cores of these external tip vortices, their trajectory can be reconstructed.
The velocity profiles, depicted in Figure 5.48, further confirm that the interaction between the two propellers is minimal. This is reflected in the thrust values, which remain nearly identical for the side-by-side and isolated cases. The comparison is between the single propeller and one propeller from the side-by-side configuration, to highlight the influence of the nearby propeller. The two wakes evolve as if they were undisturbed. Here as well, the single propeller configuration in the side-by-side case was mirrored symmetrically. In this case, however, the peaks of the single propeller from the side-by-side configuration are not shifted to the right compared to the single propeller. This is because the influence and interaction between the two wakes is minimal, and even as the $Z/D$ sections increase, the wakes remain undisturbed, showing signs of very limited interaction.

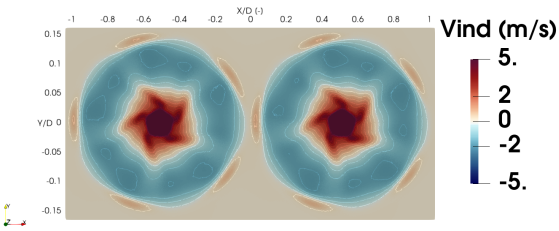


Figure 5.44: Section $Z/D = -0.2D$ FF

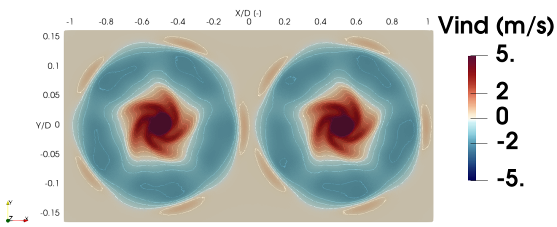


Figure 5.45: Section $Z/D = -0.4D$ FF

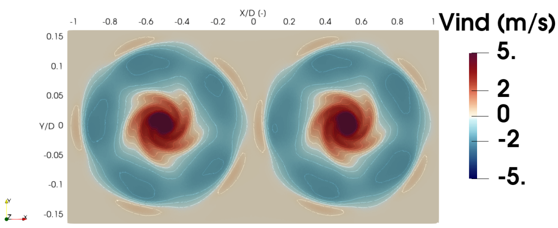


Figure 5.46: Section $Z/D = -0.7D$ FF

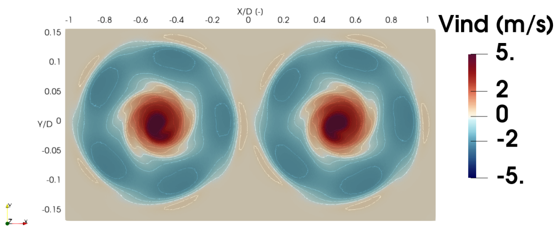


Figure 5.47: Section $Z/D = -1D$ FF

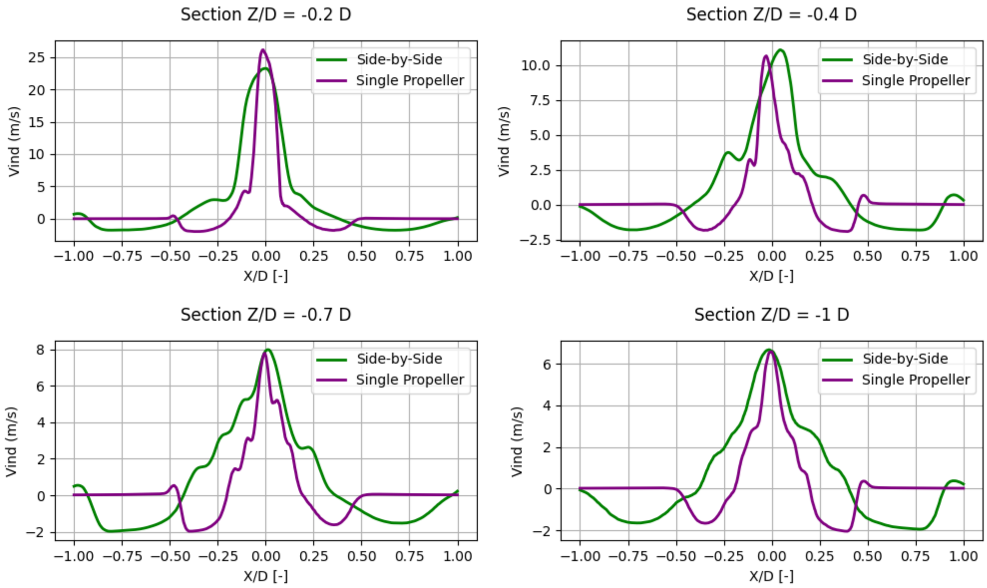


Figure 5.48: *FF: Induced Velocity profiles single propeller vs side-by-side*

## 5.5 Q-criterion

To clearly identify the vortex structures in the wake, including the tip vortices and their evolution, a 3D visualization is necessary. This can be achieved using Q-criterion isosurfaces. The Q-criterion is defined by the rotation tensor $\Omega$ and the strain-rate tensor $S$. It allows the visualization of vortex regions and aerodynamic interactions, such as those occurring in the side-by-side hover configuration. By applying the Q-criterion, it is possible to highlight the central turbulent region that forms and observe how the tip vortices merge into it.

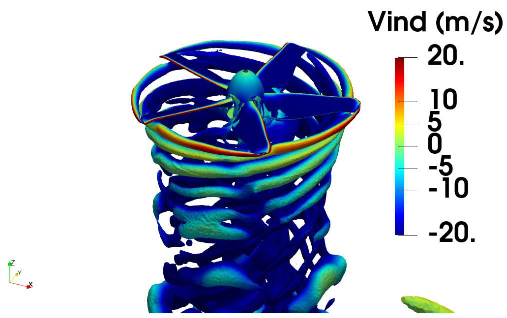


Figure 5.49: *Q-criterion hover single propeller*

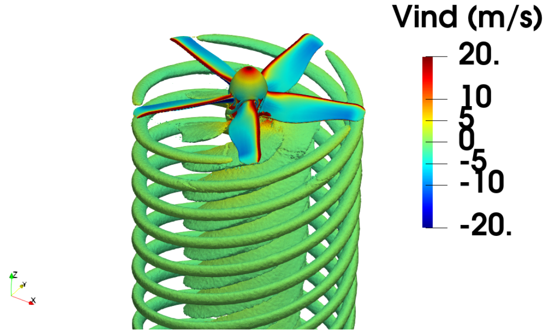


Figure 5.50: *Q-criterion forward flight single propeller*

The visualization of the single propeller highlights the differences in wake contraction discussed in this chapter, as well as the evolution of the tip vortices. In forward flight, represented in Figure 5.50, the wake remains well-preserved even at a distance, whereas in hover, Figure 5.49, it is more compact and dissipates into turbulent chaos relatively close to the propeller.
Since the Q-criterion requires setting velocity thresholds to properly visualize vortex structures, the Q-criterion values were set to 30,000 for the side-by-side hover and single-propeller simulations, and 4,000 for the single and side-by-side forward flight simulations.

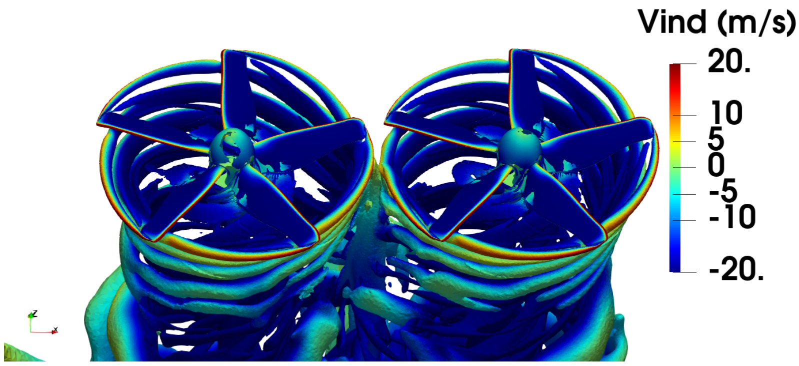


Figure 5.51: *Q-criterion hover side-by-side*

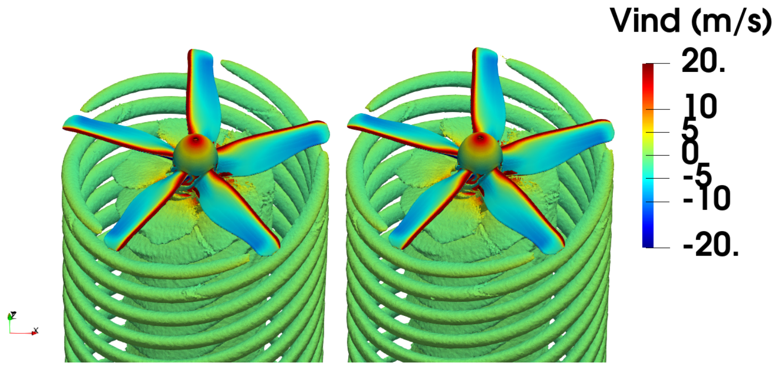


Figure 5.52: *Q-criterion forward flight side-by-side*

The central vortex region formed between the two propellers in hover is clearly identifiable in Figure 5.51. Further downstream, the tip vortices merge into this central region, creating aerodynamic interaction. In forward flight, although the spacing between the tip vortices is relatively small, the wakes of the two propellers evolve as if undisturbed, showing no significant influence from the neighboring propeller, as seen in Figure 5.52.

This finding directly addresses the research question posed in the introduction. The strong aerodynamic interaction between the two propellers in hover leads to a thrust drop, whereas the minimal interaction in forward flight results in only a slight difference in thrust between the isolated and side-by-side configurations. In the Q-criterion visualization for forward flight, one can observe that the tip vortex does not immediately form at the blade tip but begins to consolidate after a certain distance. This distance is referred to as the formation length.

From a physical perspective, each blade section releases vorticity based on its circulation, as described by the Kutta–Joukowski theorem. Unlike a fixed wing, a propeller rotates, and the centrifugal force causes the vorticity filaments shed along the blade to progressively converge toward the tip. This process ultimately produces a single, particularly strong vortex filament at the blade tip.

However, the formation of a coherent vortex is not instantaneous. It requires a fraction of a rotation for the released vorticity filaments along the blade to roll up and merge into a compact core. This spatial or angular interval is what we call the formation length.

In Q-criterion plots, we see this formation length for the vortex: it has to exceed a certain threshold in the vorticity criterion before appearing as a distinct, unified core. Consequently, the point at which the vortex becomes clearly visible in the Q-criterion iso-surfaces corresponds to the formation length required for the vorticity filaments to fully roll up.

In summary, the formation length represents the space or rotational angle needed for the vorticity initially released along the blade to coalesce into a stable, intense tip vortex, which then becomes apparent through measures such as the Q-criterion.

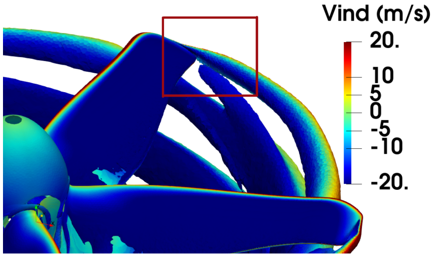


Figure 5.53: *Tip Vortex hover single prop*

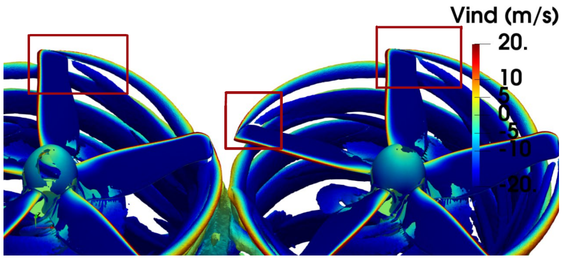


Figure 5.54: *Tip Vortex hover side-by-side*

These two images zoom in on a phenomenon that could be the cause of the periodic fluctuations observed in the thrust graph of the single propeller in hover. While this remains a hypothesis, it appears that the second vortex shedding from the tip below, as highlighted in the red rectangles in the figure, collides with the vortex produced by the adjacent blade. This interaction could be responsible for the periodic fluctuations.
The visualizations show that this phenomenon occurs in both the single and side-by-side hover configurations, represented in Figures 5.53 and 5.54 suggesting that it may contribute to the excessive unsteadiness observed in the thrust graph during the last two revolutions of the single propeller in hover.

## 5.6 Final remarks

This chapter focused on addressing the first research question posed in Chapter 1, Introduction. The research question aimed to investigate the thrust drop in the side-by-side hover configuration compared to the forward flight configuration and the aerodynamic phenomena associated with this behavior. Through the post-processing of URANS simulation data, the following assessments were made:

- The greater vortex contraction in hover compared to forward flight corresponds to significantly higher thrust production. The stronger vortex acceleration and higher velocity gradients at the wake boundary lead to increased thrust generation [10, 11]. In contrast, the presence of inertial effects from the incoming flow in forward flight transports the vortices farther away, resulting in very low thrust production, as if the propeller were spinning with minimal effect [11, 13]. The two wakes exhibit distinct characteristics: in hover, the wake is compact and energetic, dominated by local viscous forces, while in forward flight, it is more elongated, with inertial forces playing a dominant role.
- The thrust trend graphs highlight the thrust drop in the side-by-side hover case and the presence of periodic fluctuations in the single-propeller hover case [12, 14] , likely caused by vortex interactions, as observed in the Q-criterion visualization. The thrust distributions show that in forward flight, the thrust values for the isolated propeller and the side-by-side configuration are nearly identical, suggesting minimal aerodynamic interaction between the two propellers. The analysis of the azimuthal distributions of thrust and unsteady thrust highlights the unsteadiness present in the side-by-side hover case and the minimal oscillations in the forward flight case.
- The analysis of the Z-vorticity graphs, tip vortex trajectories, and induced velocity $V_{ind}$ reveals that, despite the stronger wake contraction in the single-propeller hover case, which would typically lead to higher thrust production, the wakes in the side-by-side configuration merge, forming a central turbulent region between the propellers. As the wakes develop vertically, their contraction decreases until the tip vortices merge into this turbulent area. In forward flight, the interaction between the two wakes is minimal, even though they are relatively close to each other. The inertial effects of the flow prevent the wakes from merging and instead carry the vortices further downstream.
  The aerodynamic interaction between the two wakes is the primary cause of the thrust drop in the side-by-side hover configuration, despite the high wake contraction, which would otherwise suggest higher thrust production.

# Chapter 6

# Comparison between Low-Order and High-Fidelity Model

This chapter focuses on the second research question introduced in Chapter 1, Introduction. It analyzes the comparison between the URANS simulations, presented in the previous chapter, and the reformulated Vortex Particle Method simulations obtained using the open-source software FLOWUnsteady. The primary objective is to assess whether the low-order method simulations effectively capture the wake evolution, tip vortex contraction in hover and forward flight conditions, and the aerodynamic interaction mechanisms.

## 6.1 Comparison between rVPM and URANS Simulations

One of the main aspects of using a low-order method is the computational cost of the simulation. A low-order method reduces the simulation runtime, allowing results to be obtained in a shorter time. As seen in Chapter 2, the rVPM method introduces additional equations to determine the velocity uuu instead of computing it directly using Biot-Savart laws. Another key advantage is that, being a meshless method, the time required to set up the simulation is significantly reduced. Since no mesh is generated, the setup consists only of configuring the necessary parameters in the script to achieve the desired configuration.
Because the method is based on the direct discretization of vorticity using particles, flow phenomena are represented more naturally, reducing numerical diffusion compared to traditional methods. The Lagrangian approach tracks particles and their vorticity by following the movement of the fluid.

However, there are also several disadvantages to using the rVPM method. The fidelity of low-order simulations and the simulation time depend on the number of particles used. For example, in high-fidelity low-order simulations with more than one million particles, the simulation time becomes nearly equivalent to running a URANS simulation with a coarse mesh, despite being a low-order method.
The main drawback is that achieving high accuracy in describing boundary layers near solid walls requires a very large number of particles, which can lead to even longer simulation times than a URANS simulation. Additionally, URANS includes well-established and reliable turbulence models, making it generally more robust for certain aerodynamic applications. The computational hours required to run the simulations are shown, along with the number of elements/cells used in each simulation in Table 6.1.

| Method | Software | Computational hours | Computational elements |
|---|---|---|---|
| rVPM | FLOWUNsteady | 16-20 hours (on laptop) | 1M vortex elements (high fidelity) |
| URANS (coarse mesh) | STAR-CCM+ | 24-30 hours (on cluster) | 6 M grid cells |
| URANS (refine mesh) | STAR-CCM+ | 72 hours (on cluster) | 30 M grid cells |

Table 6.1: *Description of CFD solvers*

In the next section, the thrust behavior obtained with FLOWUnsteady is analyzed to assess similarities and differences. The simulations in FLOWUnsteady were run with a larger time step compared to URANS, $\Delta t = 0.0001s$, but with fewer iterations per revolution, 100 iterations over 10 revolutions. This choice was made because, being a low-order method, using the same time step and number of iterations as in URANS would have required excessive computational time (a disadvantage) and would have prevented adequate simulation convergence. However, to ensure a fair comparison, the total physical simulation time was kept the same at $0.1s$. The propeller was correctly generated by creating .csv files containing the distribution of chord, pitch, twist, height, and airfoil data as seen in Figure 6.1.

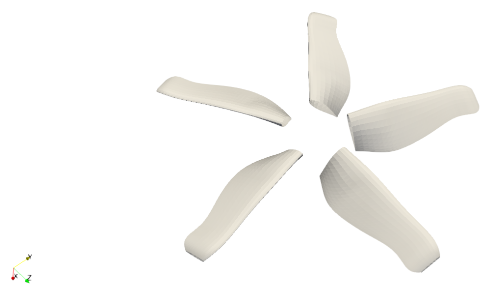

Figure 6.1: *Propeller VX4 in FLOWUNsteady*

### 6.1.1 Thrust Trend

**Hover conditions** For a proper comparison, the y-axis represents the thrust coefficient y $C_T = \frac{T_h}{\rho n^2 D^4}$ as also introduced in the previous chapter, while the $x$-axis represents the normalized time $T$ which corresponds to the time scaled by the rotational period. It is expressed as $T = \frac{t}{t_+}$, where $t$ is the simulation time and $t_+$ is the revolution period associated with the rotation rate used in the simulations.
The graphs include thrust distributions obtained from both Star-CCM+ and FLOWUnsteady to enable a thorough comparison.

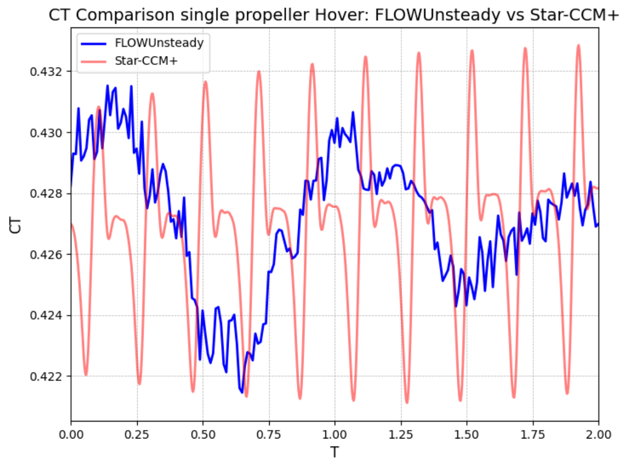


Figure 6.2: *Comparison $C_T$ single propeller hover*

The thrust behavior obtained in using FLOWUnsteady, displayed in Figure 6.2, reflects the oscillatory trend observed in the last two revolutions of the URANS thrust graph for the single-propeller hover case. Although the oscillations are not identical, their presence could confirm the interaction phenomena seen in the previous chapter in the Q-criterion hover visualization, where a second vortex shed from below the blade tip interacted with the wake. Alternatively, the differences could be attributed to variations in simulation settings, such as the turbulence model, mesh, or time step. The thrust coefficient value matches the result from the URANS simulation, indicating that the low-order method, in a shorter simulation time, successfully captures wake contraction and consequently thrust production.
A further observation emerges from analyzing the graphs. The starting position of the propeller in FLOWUnsteady is not the same as in Star-CCM+, as seen from the phase shift between the peaks and valleys in the plots. This is a limitation to keep in mind when performing accurate comparisons. In FLOWUnsteady, the initial phase also shows a transient $C_T$ value, which reaches convergence after 4 to 5 revolutions.

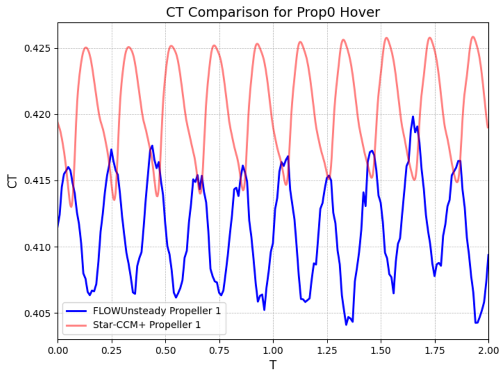


Figure 6.3: *Comparison $C_T$ Side-by-side hover Prop0*

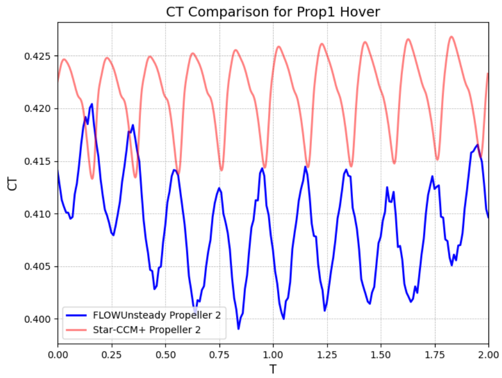


Figure 6.4: *Comparison $C_T$ Side-by-side hover Prop1*

For the side-by-side configuration, represented in Figures 6.3 and 6.4, the thrust values for the two propellers individually are different. The oscillation pattern in FLOWUnsteady matches that observed in Star-CCM+, indicating that the fluctuations caused by the interaction with the neighboring propeller are captured in both simulations. To ensure a proper comparison, the same $2\%D$ spacing between the two propellers was maintained. However, the values obtained differ because, in the side-by-side case, any discrepancies between the two computational methods (such as mesh resolution, turbulence models, time step, and boundary conditions) become even more pronounced due to the added complexity of rotor interaction. Each solver may capture this interaction differently, particularly in aspects such as tip vortices and the complex wake structure forming between the two rotating disks. These differences can lead to variations in both the mean thrust values and the amplitude of $C_T$ oscillations as seen in Table 6.2.

| Hover | $C_T$ (FU) | $C_T$ (Star-CCM+) | $T$ $[N]$ (FU) | $T$ $[N]$ (Star-CCM+) |
|---|---|---|---|---|
| Single propeller | 0.427 | 0.427 | 23 $[N]$ | 23.02 $[N]$ |
| Side-by-side (Prop0) | 0.41 | 0.418 | 22.10 $[N]$ | 22.6 $[N]$ |
| Side-by-side (Prop1) | 0.41 | 0.42 | 22.10 $[N]$ | 22.7 $[N]$ |

Table 6.2: *Thrust values hover configuration*

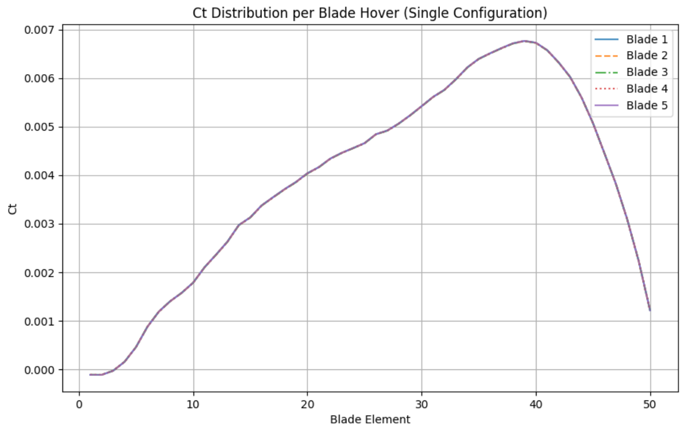


Figure 6.5: *$C_T$ distribution single propeller hover*

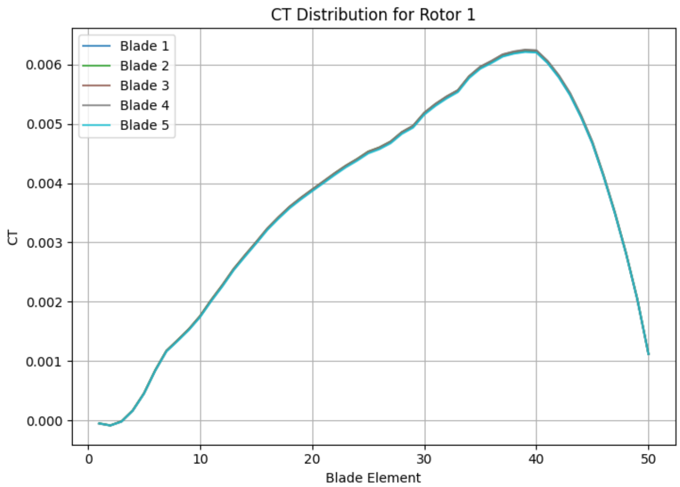


Figure 6.6: *$C_T$ distribution side-by-side hover*

In FLOWUnsteady, the thrust distribution for each blade element was also reconstructed. While the URANS simulation used 25 blade elements, this simulation used 50 elements, consistent with the setup in the simulation script. In Figures 6.5 and 6.6, the thrust distribution along the blade span is shown for both the single and side-by-side cases. Since the behavior of the rotors is identical, only one propeller is presented for the side-by-side configuration. To plot the thrust distribution, the distributed thrust value $N_p$, extracted from the loft.vtk output files, must be multiplied by the radial spacing between blade elements for each time step and each blade. However, the displayed trend does not account for the decreasing spacing between blade elements as you move toward the tip. In the script, the spacing between elements was set to gradually decrease near the blade tip. This approach allows for better resolution of the tip vortices generated in that region. The resulting trend follows a quadratic pattern, increasing to a peak and then decreasing. The minimum after the peak is positioned lower compared to the URANS graphs. This could be due to the inviscid + Prandtl correction approach used in FLOWUnsteady, which may be less detailed in capturing local flow physics compared to the Star-CCM+ solver. Differences are particularly noticeable in regions where three-dimensional and viscous effects play a more significant role, such as near the blade tip.

**Forward flight conditions** Now, we analyze the forward flight configuration and how the thrust distributions are reproduced in FLOWUnsteady.

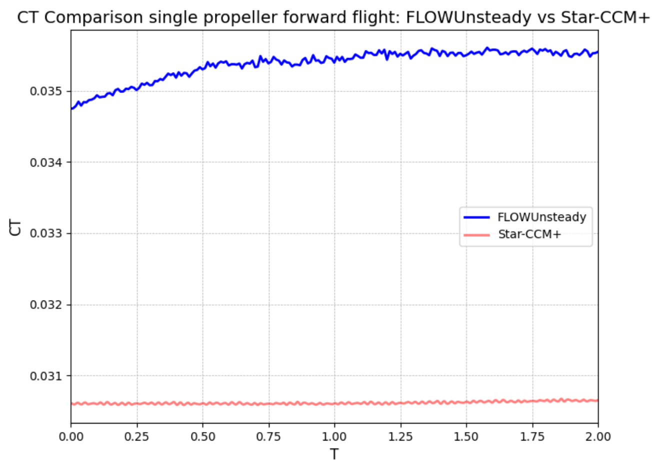


Figure 6.7: *Comparison $C_T$ single propeller FF*

In Figure 6.7, the comparison of $C_T$ for the forward flight case is shown. The thrust values differ between FLOWUnsteady and Star-CCM+. There is a clear discrepancy between the two processed $C_T$ values. The primary reason for this difference is likely the different models used to process the wakes. The rVPM method appears to generate a wake with greater contraction compared to URANS, leading to a higher $C_T$. Another possible explanation is that since FLOWUnsteady employs an inviscid model, it may not fully capture the three-dimensional and viscous effects, which are more significant in forward flight than in hover. However, the amplitude of the oscillations appears to be similar in both cases.

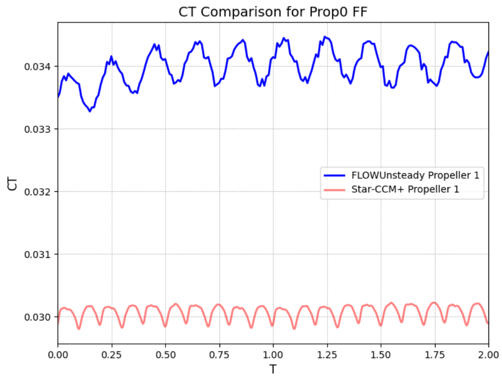


Figure 6.8: *Comparison $C_T$ side-by-side Prop0 FF*

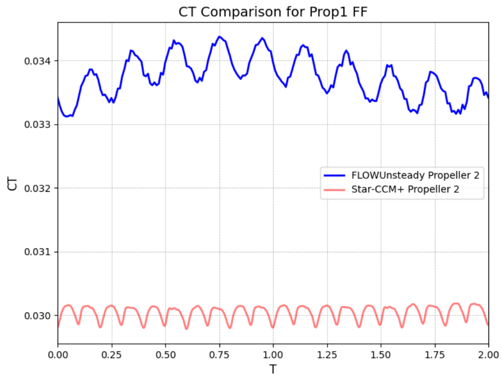


Figure 6.9: *Comparison $C_T$ side-by-side Prop1 FF*

For the side-by-side configuration, there is also a clear discrepancy between the $C_T$ values obtained from the two software, as seen in Figures 6.8 and 6.9. The oscillation amplitude is larger in FLOWUnsteady, and the unsteadiness is more pronounced compared to the single-propeller case. However, as in the previous case, the interaction between the two propellers in forward flight remains significantly lower than in hover. The fluctuations are smaller, with only a minimal change in thrust between the single-propeller and side-by-side configurations, as seen in Table 6.3.

| Hover | $C_T$ (FU) | $C_T$ (Star-CCM+) | $T$ $[N]$ (FU) | $T$ $[N]$ (Star-CCM+) |
|---|---|---|---|---|
| Single propeller | 0.0351 | 0.0306 | 1.89 $[N]$ | 1.65 $[N]$ |
| Side-by-side (Prop0) | 0.0338 | 0.03 | 1.822 $[N]$ | 1.62 $[N]$ |
| Side-by-side (Prop1) | 0.0336 | 0.03 | 1.812 $[N]$ | 1.62 $[N]$ |

Table 6.3: *Thrust values Forward Flight configuration*

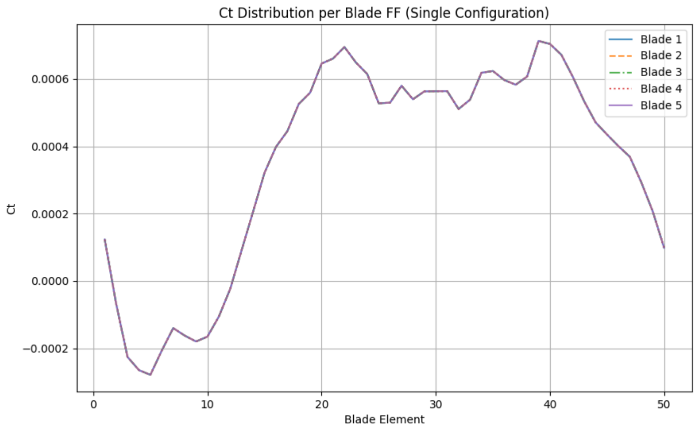


Figure 6.10: $C_T$ *distibution single propeller FF*

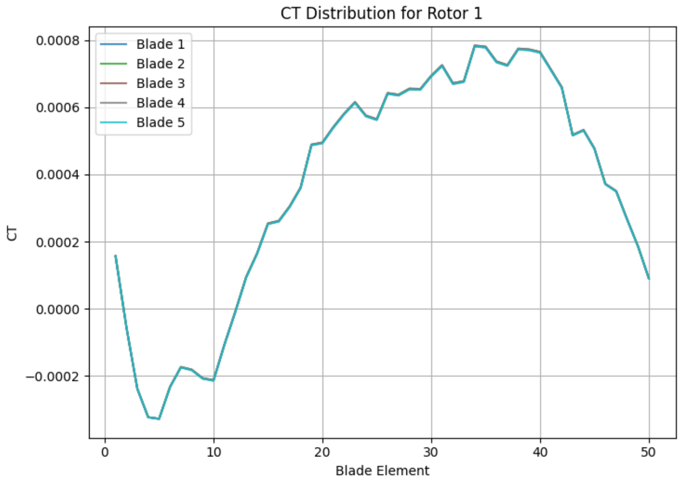


Figure 6.11: $C_T$ *distribution side-by-side FF*

The $C_T$ distribution in forward flight represented in Figures 6.10 and 6.11, follows a quadratic trend similar to that in URANS. However, discrepancies exist between the two due to differences in the simulation models. Since the script was set to inviscid + correction hub/tip loss to reduce lift near the hub and blade tip, viscous effects and flow separation are resolved with lower accuracy. In FLOWUnsteady, the root-to-tip transition may appear more abrupt or exhibit a higher peak due to the inviscid nature of the method and a possible overestimation of $C_T$. Here as well, the trend does not account for the decreasing radial distance between blade elements as they approach the tip, which was set to better capture the tip vortices. In the single propeller case, the trend is not perfectly quadratic as expected. Instead of showing a clear peak, there is a flattened region, which further highlights the fact that in forward flight the propeller is practically spinning unloaded, producing very low thrust.

### 6.1.2 Flow field

**Single propeller** The flow fields obtained in FLOWUnsteady for the single propeller and side-by-side configurations in hover and forward flight are now shown, in order to analyze how they are represented and what similarities they share with the URANS flow fields.

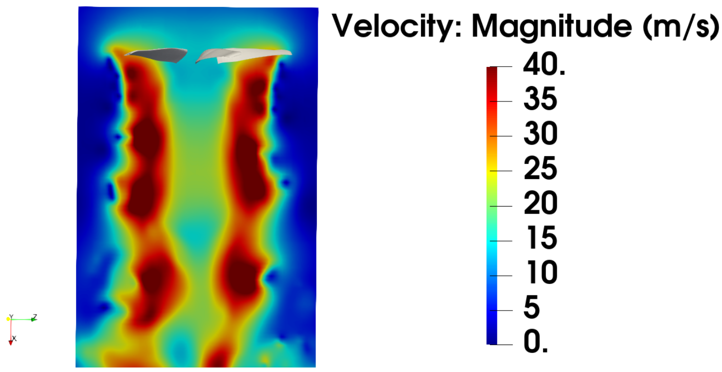


Figure 6.12: *Velocity magnitude single prop (hover)*

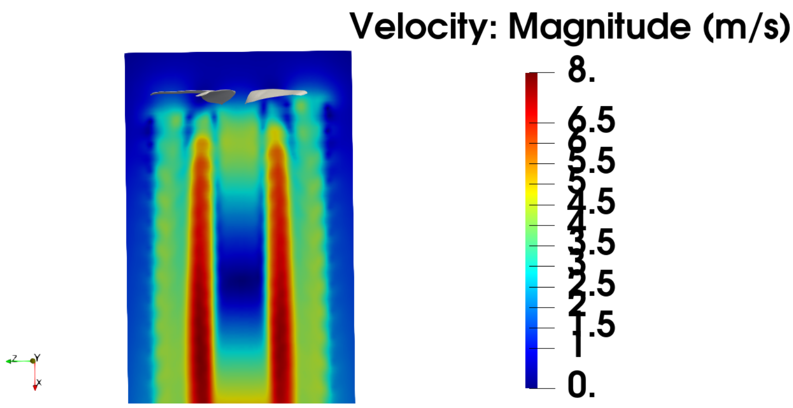


Figure 6.13: *Velocity magnitude single prop (FF)*

From the velocity magnitude scenes processed in ParaView, using the .xmf output file generated by the fluid domain script in FLOWUnsteady, it can be seen in Figures 6.12 and 6.13, that the characteristic shape of the wake in both forward flight

and hover is captured. As observed in the previous chapter, the hover wake shows greater contraction compared to forward flight, the flow is more accelerated, and as confirmed by the thrust graphs, this corresponds to higher thrust production.
However, the visualization also reveals a limited resolution of three-dimensional effects and tip vortices, due to the input script settings and the absence of a proper mesh. In the forward flight scene, only the effect of the blades on the wake is shown, without accounting for the incoming freestream velocity, although it was set in the script to match the URANS case in terms of advance ratio.
Using an inviscid model prevents the capture of boundary layer development and flow separation around the blades. Additionally, the use of a different turbulence model compared to URANS affects the wake structure, limiting the presence of turbulent three-dimensional features. The turbulent structures are not highly resolved, but this trade-off helps reduce computational cost.

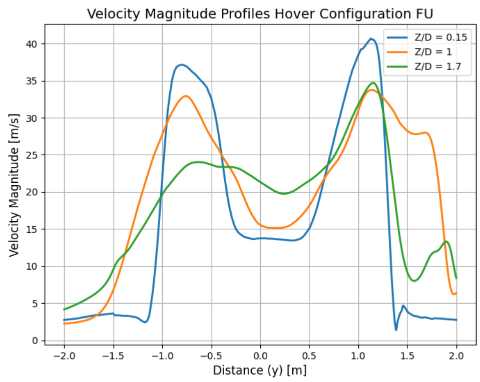


Figure 6.14: *Velocity profiles single prop FF (hover)*

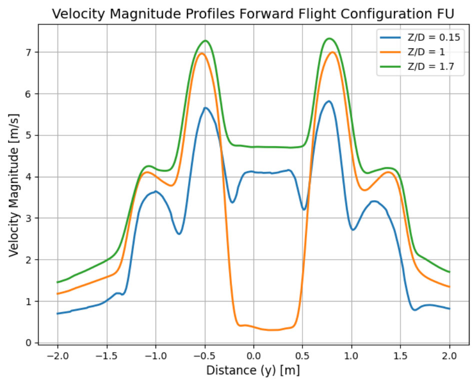


Figure 6.15: *Velocity profiles single prop FF (forward flight)*

The processed velocity profiles presented Figure 6.14 and 6.15, show sharper peaks, as there is no full resolution of the boundary layer and turbulent diffusion is not naturally captured. FLOWUnsteady generally does not predict large regions of low or negative velocity unless specific corrections are introduced in the simulation script. In the forward flight case, the velocity peaks in the initial $Z/D$ sections are less sharp and less deep due to the lack of direct viscous dissipation. In essence, FLOWUnsteady tends to display higher peaks and smaller low-velocity regions because it does not directly resolve viscosity.
These differences become more noticeable in forward flight, where the flow complexity allows a URANS simulation to capture details that the inviscid approach cannot represent as accurately.

**Side-by-side** The side-by-side configurations from FLOWUnsteady are presented to analyze the interaction between the wakes of the propellers.

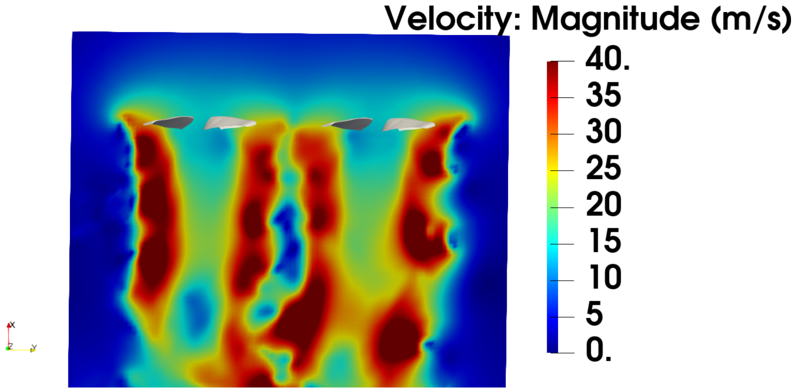


Figure 6.16: *Velocity magnitude side-by-side (hover)*

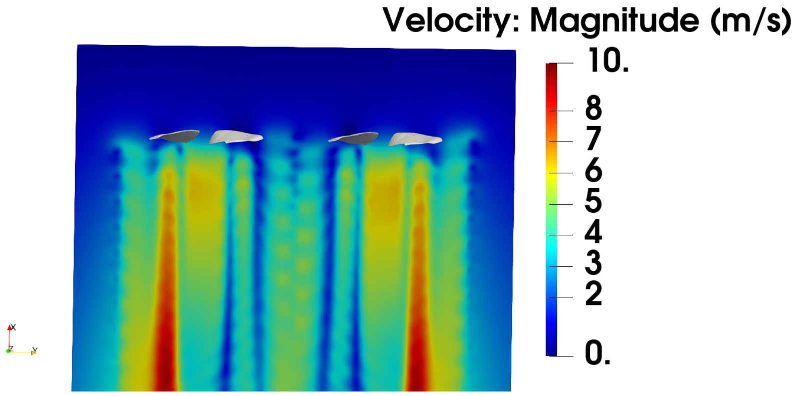


Figure 6.17: *Velocity magnitude side-by-side (FF)*

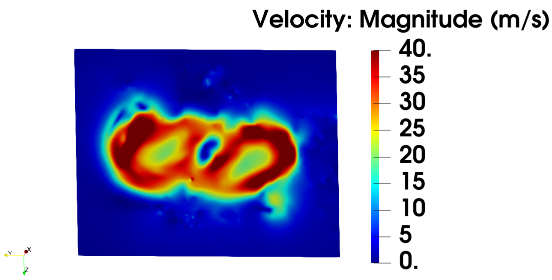


Figure 6.18: *Section flow field hover side*

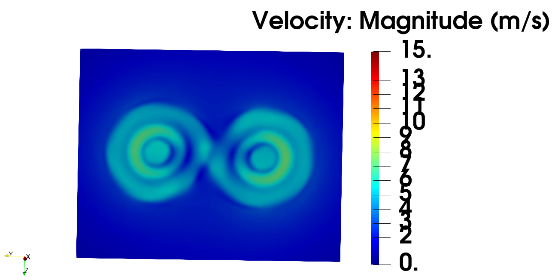


Figure 6.19: *Section flow field FF side*

The velocity magnitude visualizations of the side-by-side propeller configuration in FLOWUnsteady closely reflect the interaction seen in the URANS simulation results.

In the hover case, Figure 6.16, although not as clearly defined, the aerodynamic interaction zone generated between the two propellers is visible and is responsible for the thrust drop observed. Below this interaction, a chaotic and turbulent region forms, similar to what was seen in the URANS simulations.
In the forward flight case, Figure 6.17 the vortex wakes generated by each propeller can be clearly distinguished. Even though the spacing between the vortices is minimal, inertial effects carry the vortices downstream, resulting in very limited interaction between the two wakes. This minimal influence is reflected in the thrust graphs, showing almost no drop in thrust between the isolated propeller configuration and the side-by-side case. Figures 6.18 and 6.19 show, in the hover case, the two wakes merging, and in the forward flight case, the minimal interaction between the wakes.

**Tip vortex trajectory and Z-vorticity** The Z-vorticity scenes are analyzed to highlight how the tip vortices evolve in FLOWUnsteady.

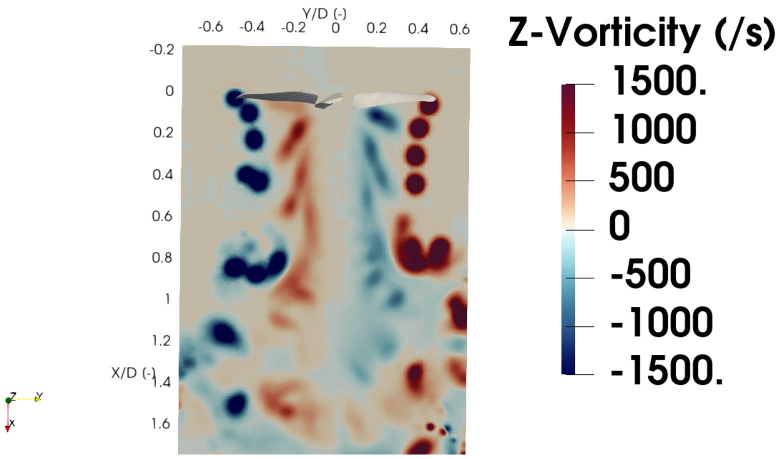


Figure 6.20: *Z-Vorticity single prop (hover)*

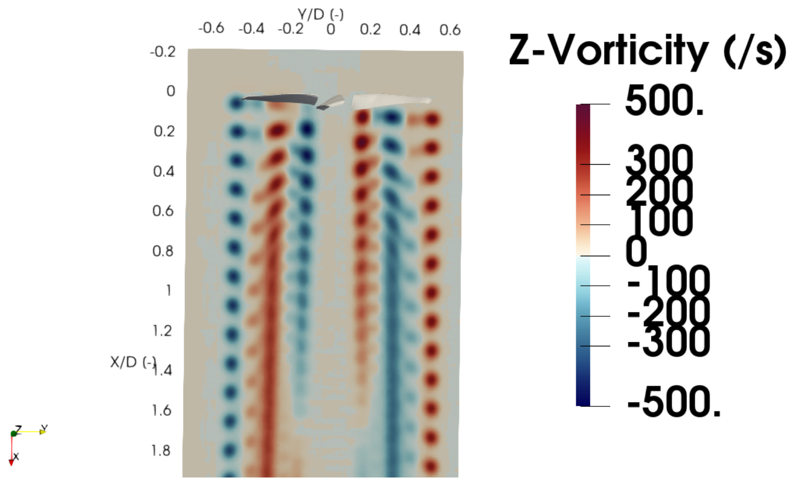


Figure 6.21: *Z-Vorticity single prop (FF)*

In the Z-vorticity plots, the vortices present in the wake can be clearly distinguished. In the hover configuration, displayed in Figure 6.20, the vortices show greater contraction, which is well captured in the visualization. The flow is more strongly accelerated, and the vortices remain visible even far downstream from the propeller. Due to the absence of a viscous model, the wake likely experiences limited diffusion, allowing the vortices to stay well-defined in regions where URANS simulations show energy dissipation.
The forward flight configuration also matches the expected behavior, with well-defined vortices that continue to develop even at large distances from the propeller, as seen in Figure 6.21 The SFS nobackscatter model, set in the input script, damps the unresolved small scales, simulating energy loss due to turbulence without re-injecting it into the resolved scales.
As a result, the small scales are gradually damped in a dissipative manner, and the vorticity field appears smoother and less fragmented by turbulent structures in the visualization.
However, the tip vortices still follow the flow contraction, and the vortex filaments appear well-defined, intense, and less diffused. In hover, differences can be seen in the vertical distribution and intensity of the tip vortices. In forward flight, the actual wake may be more complex than what is represented.

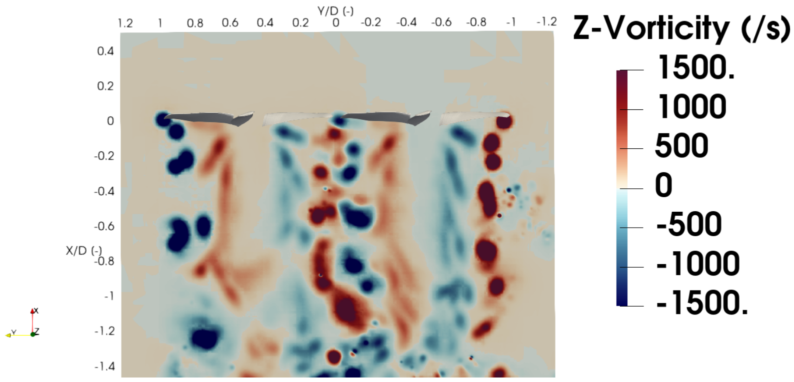


Figure 6.22: *Z-Vorticity single prop (hover)*

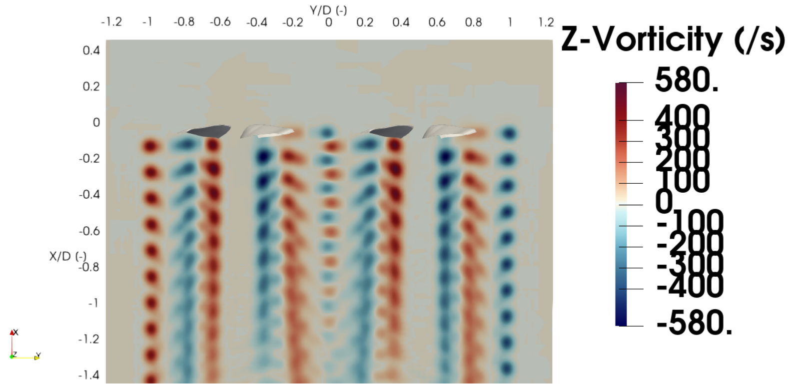


Figure 6.23: *Z-Vorticity single prop (FF)*

The Z-vorticity visualization for the side-by-side configuration, shown in Figures 6.22 and 6.23, confirms the reduced contraction observed in the hover case compared to the isolated propeller. This phenomenon is due to the two wakes merging after a certain distance, forming a turbulent interaction zone that leads to the thrust drop. The vortices are clearly defined, and the merging of two vortices into the underlying turbulent region can be seen.
In the forward flight case, the generated tip vortices are even more clearly distinguishable. However, the inertial forces prevent the vortices from merging, despite the small spacing between them, and instead carry them downstream along the wake.

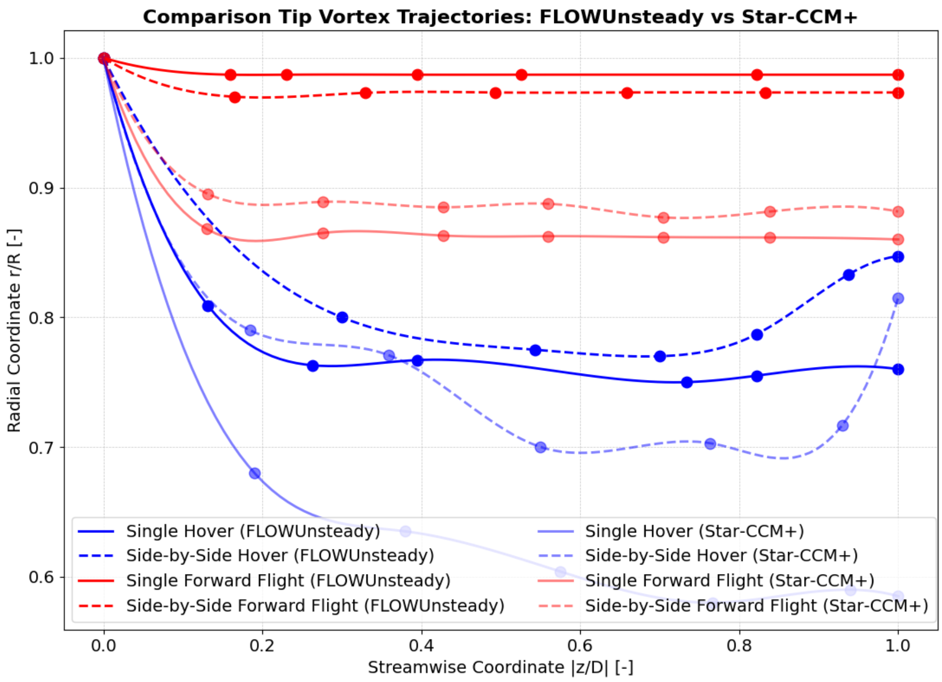


Figure 6.24: *Tip vortex trajectory FU*

The graph in Figure 6.24, clearly highlights the similarities with the URANS case. The vortex evolution trajectories closely match those observed in the URANS simulations. In the single-propeller hover case, the vortices show strong contraction, followed by a stabilization after a certain distance, and then enter the turbulent region downstream. In the side-by-side case, the contraction is noticeably weaker compared to the single-propeller configuration. This is due to the mutual influence of the two wakes, which causes them to merge. As in the URANS case, after approximately $X/D = 0.8$, the vortices merge into the central turbulent region, leading to the observed thrust drop. In forward flight, the tip vortex trajectories are nearly identical in both the single and side-by-side configurations. This is because inertial effects are strong enough to make the interaction between the two wakes negligible, resulting in a behavior very similar to what was seen in the URANS simulations. This graph shows that with FLOWUnsteady, we are still able to clearly capture the trajectory of the tip vortices, which are well discretized by the low-order method. The same trends of wake contraction and aerodynamic interaction observed in the URANS case are also visible here.

**Three-Dimensional Particle Field Visualization** Now we visualize the three-dimensional particle field and how the tip vortices appear in the overall wake generated by the propeller. The scenes of the three-dimensional vorticity magnitude are analyzed to observe the evolution of the tip vortices and the aerodynamic interaction in the side-by-side case, along with the particle field generated by the simulation.

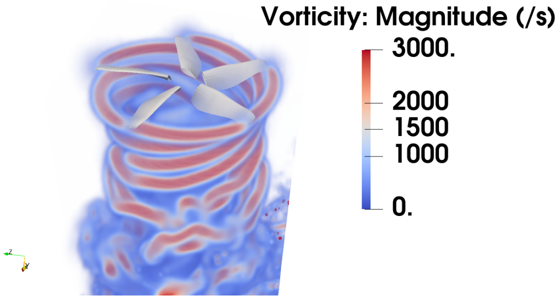


Figure 6.25: *3D Vorticity magnitude hover single*

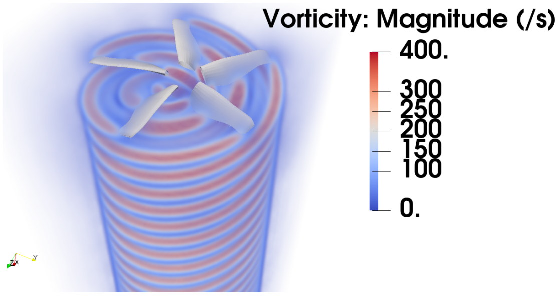


Figure 6.26: *3D Vorticity magnitude FF single*

As seen in the three-dimensional visualizations of vorticity magnitude for the single propeller case, the wake is well aligned with the Q-criterion representation from the URANS simulations. While it lacks the accuracy in capturing small turbulent structures, the evolution and behavior of the tip vortices are consistent with what is reported in the literature. In the hover case, represented in Figure 6.25, the flow shows greater contraction, stronger acceleration of the tip vortices, and the formation of a dissipative turbulent region at a long distance from the propeller. In forward flight, depicted in Figure 6.26, the presence of inertial effects is evident, as the wake remains coherent even at large distances from the propeller. FLOWUnsteady is able to capture the essential physical phenomena of the problem, although it lacks precision in the resolution of turbulent structures, as seen in the URANS simulations.

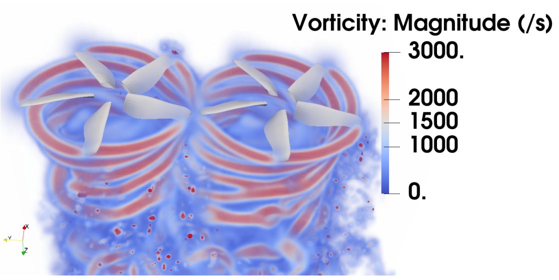


Figure 6.27: *3D Vorticity Magnitude hover side*

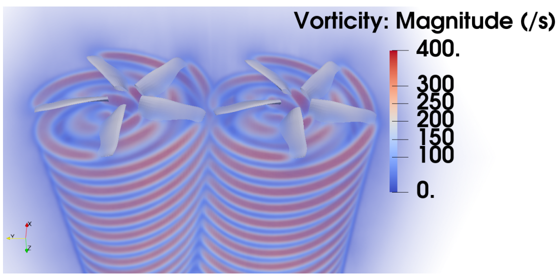


Figure 6.28: *3D Vorticity Magnitude FF side*

For the side-by-side configuration, the wake shape is once again consistent with what is reported in the literature. In the hover case, the two wakes influence each other, creating a turbulent region between them, as seen in Figure 6.27. Although this region is not clearly defined in the FLOWUnsteady visualization, it still impacts the generated thrust. At a certain point, the tip vortices break down and merge into the aerodynamic interaction zone between the two propellers. In the forward flight case, represented in Figure 6.28 even though the spacing between the tip vortices generated by each propeller appears very small, the inertial effects once again prevent the wakes from merging. As a result, the thrust produced by each propeller in the side-by-side configuration is almost the same as that of the isolated propeller. It is important to emphasize that FLOWUnsteady, overall, is able to reproduce the expected wake physics described in the literature, although its level of accuracy differs from that of a URANS model.

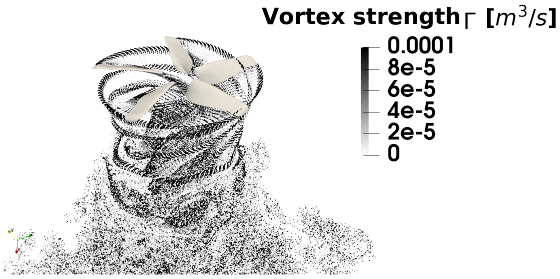


Figure 6.29: *Particle field hover single*

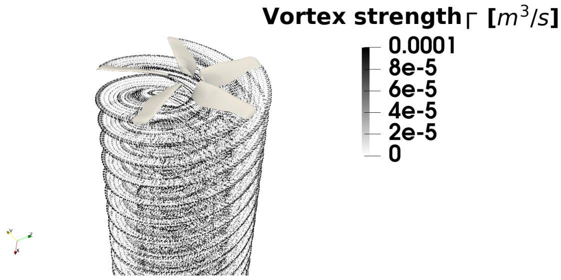


Figure 6.30: *Particle field FF single*

To visualize the particle field generated by the simulation, FLOWUnsteady uses Γ, which represents the vortex strength and is assigned to each particle or vortex element to indicate the amount of vorticity it carries. This parameter is essential for displaying the full field produced by the particles. The particle fields for the single propeller are shown in the Figures 6.29 and 6.30. The wake evolution and interaction mechanisms are the same as those previously observed in the vorticity magnitude visualizations. The flow fields are well discretized by the particles, as seen in Figures 6.31 and 6.32 , closely resembling those seen in the URANS simulations. This visualization is intended solely to show the particle field produced by the simulation, as FLOWUnsteady is based on the vortex particle method.

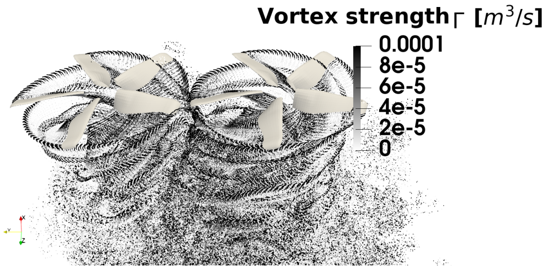


Figure 6.31: *Particle field hover side-by-side*

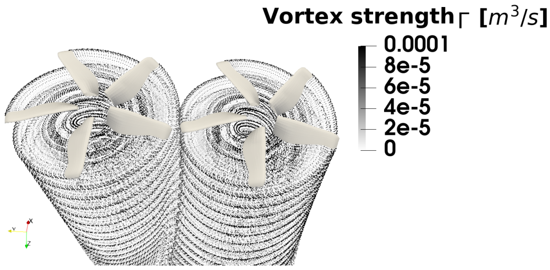


Figure 6.32: *Particle field FF side-by-side*

### 6.1.3 Final remarks

In this section, a comparison was made between the FLOWUnsteady and Star-CCM+ software, using two different approaches: a low-order method based on the reformulated vortex particle method, and a high-fidelity method based on URANS simulations. Similarities and differences were highlighted in both performance trends and flow field visualizations. The trends observed in this chapter, based on how the aerodynamics of propellers in a side-by-side configuration is modeled are consistent with those found in the literature, particularly in the papers by [21–23, 57]. The answer to the second research question, introduced in Chapter 1, Introduction, can be summarized as follows:

- The advantage of running a URANS simulation lies in having a high-fidelity solution where turbulent structures are represented in the most accurate way. To achieve a similar level of accuracy using the low-order rVPM method, a very high number of particles would be required, resulting in a significantly longer simulation time. This runtime could be comparable to that of a URANS simulation with a coarse mesh. Therefore, it is ultimately necessary to run a URANS simulation to better capture turbulent structures and provide more accurate and detailed representations of the flow and the results. Another important aspect to consider is the availability of computational resources. FLOWUnsteady offers a good compromise for obtaining results quickly with limited computational resources (such as a laptop), whereas URANS requires more powerful hardware and greater computational capacity.
- The advantage of FLOWUnsteady lies in its ability to run a high-fidelity simulation (with more than 1 million particles) in a single day on a personal laptop. Having access to preliminary simulations and reference data in a short time can be a key benefit. Through the various input settings in FLOWUnsteady, the wake is modeled according to the literature, and the main phenomena such as contraction and tip vortex evolution are accurately reproduced. Aerodynamic interaction effects within the configuration are also correctly captured. However, the main limitation concerns the accuracy and level of detail in the visualization of turbulent structures. The model used in this work is the SFS backscatter, which damps small-scale turbulence. In the future, new models could be introduced to provide a more accurate and detailed representation of these turbulent features.

To conclude, the low-order method FLOWUnsteady is well suited for obtaining preliminary results and initial estimates in a short time with minimal computational resources. While the different turbulent structures are not modeled with high accuracy, the main aerodynamic phenomena are represented reliably. For more detailed analysis of viscous effects and the various scales of turbulence, especially in complex flow conditions, URANS provides more accurate and dependable results, though it requires significantly higher computational resources. To conclude, the low-order method is a useful tool for preliminary analysis in the early stages of a project, providing a general overview of the aerodynamic phenomena that will also appear in higher-fidelity simulations. It is important to note that using URANS to validate FLOWUnsteady was the only available option in this case, but it comes with some uncertainty. The URANS simulations themselves lack validation with experimental data, and the numerical models are based on fundamentally different approaches, which limits the reliability of the comparison. It is therefore important to interpret these comparisons with a clear understanding of the limitations and assumptions inherent to each method.

# Chapter 7

# Conclusions and Future Works

Urban Air Mobility (UAM) is emerging as one of the most innovative and promising developments in modern aviation. Growing urbanization and the demand for more efficient and sustainable transport systems have led to the creation of aircraft tailored for urban operations, providing fast and safe alternatives to conventional ground transportation. Among these, electric Vertical Take-Off and Landing (eVTOL) vehicles are reshaping the concept of air mobility, offering a range of potential benefits. However, several technical challenges remain, including integration with current air traffic systems and effective noise control. Noise is a particularly critical issue for eVTOLs, as the interaction of propeller blade tip vortices can produce sounds that are disruptive to city residents. The successful deployment of these technologies depends heavily on a deep understanding of the aerodynamic behavior of the propellers involved. This thesis focused on investigating, through high-fidelity and low-order numerical simulations, the aerodynamic interaction mechanisms between propellers in both hover and forward flight conditions, considering a single isolated propeller and a side-by-side configuration with minimal tip-to-tip distance.

## 7.1 Conclusions

The thesis project focused on the numerical investigation of propellers in a side-by-side configuration and on the aerodynamic mechanisms that lead to thrust loss. The work gradually progressed toward implementing the high-fidelity numerical model, starting with understanding the Star-CCM+ software and then moving on to the low-order model FLOWUnsteady. The low-order method was used in comparison with the URANS approach to evaluate its reliability in the context of early project pre-design, when a clear definition of the final aircraft is not yet available. Step by step, theoretical and explanatory elements were added to better understand the phenomena involved, ultimately providing clear answers to the research questions outlined in the introductory chapter. The following conclusions were reached:

- The aerodynamic interaction in hover between two propellers with a tip-to-tip distance of 2% results in a noticeable drop in thrust, here as well, about 2% of the thrust produced in the single propeller configuration, as also seen in the literature in the papers [9, 10] . This effect is caused by the aerodynamic interaction between the wakes of the two propellers when placed in close proximity. A central upward turbulent region forms, where the tip vortices, after a certain distance of development, tend to merge, as also seen in [11]. Evidence of the various effects observed in the side-by-side configuration was found in the literature in the paper by [12,14]. Despite the strong contraction observed in the single-propeller hover case, the wakes in the side-by-side configuration show reduced contraction as they begin to merge with each other.

- The forward flight case shows a different interaction behavior between the two wakes in the side-by-side configuration. The presence of strong inertial effects results in a nearly negligible thrust drop, as the two wakes, despite the minimal distance between the tip vortices, do not merge but are instead carried downstream, as also found in the paper [13]. The thrust produced by a single propeller in the side-by-side configuration is nearly the same as that of the isolated propeller, confirming the minimal interaction between the wakes of the two propellers.

- The low order software FLOWUnsteady, based on the reformulated vortex particle method (rVPM), accurately reproduces the aerodynamic phenomena observed in both the single propeller and side-by-side configurations, as also observed in the trends found in the literature [21–23, 57]. It is suitable when the goal is to perform a global simulation with low computational cost and to obtain an initial estimate of the flow behavior and results. However, for more detailed analyses where the objective is to accurately capture viscous effects and the full range of turbulent structures, especially in complex flow conditions, URANS simulations with Star-CCM+ provide more reliable results.

This thesis project is, however, incomplete in terms of result validation. The experimental phase will soon be carried out at the von Karman Institute for Fluid Dynamics using the VX4 propeller, which will provide a more concrete comparison with the numerical data obtained. At this stage, some doubts remain regarding the aerodynamic phenomena observed in the graphs, which may be clarified in future work. URANS simulations were used as a reference to compare with rVPM simulations, with the sole purpose of evaluating the differences between a low-order method and a high-fidelity one. However, this approach can be seen as a risk, as it involves comparing two physical and numerical models that rely on very different assumptions and there were not many results to compare. It is therefore important to interpret these comparisons with a clear understanding of the limitations and assumptions inherent to each method. The ultimate goal of this thesis was intended to be the analysis of tonal noise using prediction algorithms, once the unsteady loading was obtained. This will be addressed in future work.

## 7.2 Future works

This thesis focused on the numerical investigation of two propellers in a side-by-side configuration. Based on this work, several directions for future research are suggested:

- The single propeller hover case certainly deserves further investigation using higher numerical accuracy methods, in order to evaluate the behavior and the impact of numerical parameters on the obtained solutions. Due to limited computational resources, a Large Eddy Simulation (LES) was not included in this thesis. However, incorporating LES in future studies could provide more detailed insights into the aerodynamic interaction between the two propellers, as turbulent structures would be modeled more accurately.
- The lack of reference experimental data made direct validation of the simulations impossible. In the future, an experiment will be set up to collect experimental data, which will allow for the validation of the numerical results and a better investigation of the aerodynamic phenomena that currently raise questions about the findings.
- Based on the aerodynamic results obtained, noise could be investigated, particularly tonal noise in the far field. In particular, once the unsteady loading of the propeller is obtained, a possible final goal of this thesis could be to investigate tonal noise using prediction algorithms, in order to evaluate how much sound is generated in the different cases studied, as shown in these research works [56, 58]. Analyzing how the unsteadiness caused by aerodynamic interaction in the side-by-side configuration contributes to noise generation would be a key step toward understanding and mitigating rotor noise pollution.
- It was observed that thrust produced in forward flight is very low, making it appear as though the propeller is almost unloaded. According to information from the propeller manufacturer, applying a pitch angle could increase thrust. This could be an interesting topic for future work to identify the optimal pitch

angle that balances thrust production and noise reduction.

- Introducing a phase angle could be an effective strategy to explore and control interaction dynamics between blades and rotors. It would help improve understanding of wake interaction phenomena. With an appropriate phase angle, far-field noise levels could also be reduced, contributing to lower acoustic impact.
- Using FLOWUnsteady, different parameters from those used in this thesis could be explored to achieve results closer to URANS level accuracy. With more computational resources, future work could include simulations with a higher number of particles to better reproduce wake development, while also incorporating viscous and turbulence models.

# Bibliography


[1] Mehmet Necati CiZreliOğullari, Pınar Barut, and Tapdig Imanov. Future air transportation ramification: urban air mobility (UAM) concept: Urban Air Mobility. *Prizren social science journal*, 2022.

[2] Eduardo Cabrera and João M. Melo De Sousa. Use of Sustainable Fuels in Aviation—A Review. *Energies*, 2022.

[3] W. Johnson and C. Silva. NASA concept vehicles and the engineering of advanced air mobility aircraft. *The Aeronautical Journal*, 2022.

[4] Anna Straubinger, Raoul Rothfeld, Michael Shamiyeh, Kai-Daniel Büchter, Jochen Kaiser, and Kay Olaf Plötner. An overview of current research and developments in urban air mobility – Setting the scene for UAM introduction. *Journal of Air Transport Management*, 2020.

[5] Antonio J. Torija and Charlotte Clark. A Psychoacoustic Approach to Building Knowledge about Human Response to Noise of Unmanned Aerial Vehicles. *International Journal of Environmental Research and Public Health*, 18, 2021.

[6] Yiyuan Ma, Wei Zhang, Yizhe Zhang, Yuelong Ma, and Zhiliang Bai. Preliminary Design and Experimental Investigation of a Distributed Electric Propulsion Aircraft. *ICAS*, 2021.

[7] Alessandro Zarri, Alexandros Koutsoukos, Francesco Avallone, Frits de Prenter, Daniele Ragni, and Damiano Casalino. Aeroacoustic Interaction Effects of Adjacent Propellers in Forward Flight. 2023.

[8] Steven Yoon, Henry C. Lee, and Thomas H. Pulliam. Computational Analysis of Multi-Rotor Flows. January 2016.

[9] Wenwu Zhou, Zhe Ning, Haixing Li, and Hui Hu. An Experimental Investigation on Rotor-to-Rotor Interactions of Small UAV Propellers. 2017.

[10] Giorgia Sinibaldi and Luca Marino. Experimental analysis on the noise of propellers for small UAV. *Applied Acoustics*, 2013.

[11] Angus Leslie, Kee Choon Wong, and Doug Auld. Broadband Noise Reduction on a mini-UAV Propeller. 2008.

[12] Matthew Misiorowski, Farhan Gandhi, and Assad A. Oberai. Computational Study on Rotor Interactional Effects for a Quadcopter in Edgewise Flight. *AIAA Journal*, 2019.

[13] Reynard De Vries, Nando Van Arnhem, Tomas Sinnige, Roelof Vos, and Leo L.M. Veldhuis. Aerodynamic interaction between propellers of a distributed-propulsion system in forward flight. *Aerospace Science and Technology*, 2021.

[14] Riccardo Piccinini, Matteo Tugnoli, and Alex Zanotti. Numerical Investigation of the Rotor-Rotor Aerodynamic Interaction for eVTOL Aircraft Configurations. *Energies*, 2020.

[15] Reda R. Mankbadi. Transition, turbulence, and noise. *MA:Spinger US*, 1994.

[16] Tapan K. Sengupta and Yogesh G. Bhumkar. *Computational Aerodynamics and Aeroacoustics*. Springer Singapore, 2020.

[17] Eric Manoha, Stephane Redonnet, and Stephane Caro. Computational aeroacoustics. *Encyclopedia of Aerospace Engineering*, 2010.

[18] D. Akiwate, P. Joseph, A. B. Parry, and C. Paruchuri. On the balance between the tonal and broadband noise of uninstalled propellers. *Institute of Sound and Vibration Research*, 2021.

[19] Georges-Henri Cottet and Petros D. Koumoutsakos. *Vortex Methods: Theory and Practice*. Cambridge University Press, 2000.

[20] Erwin Stein. Volume 2 Solids and Structures.

[21] Eduardo J. Alvarez and Andrew Ning. Stable Vortex Particle Method Formulation for Meshless Large-Eddy Simulation. 2024. Publisher: American Institute of Aeronautics and Astronautics (AIAA).

[22] Eduardo J. Alvarez and Andrew Ning. Meshless Large-Eddy Simulation of Propeller–Wing Interactions with Reformulated Vortex Particle Method. *Journal of Aircraft*, 2024. Publisher: American Institute of Aeronautics and Astronautics (AIAA).

[23] Eduardo J. Alvarez and Andrew Ning. High-Fidelity Modeling of Multirotor Aerodynamic Interactions for Aircraft Design. *AIAA Journal*, 2020.

[24] M. H. Zawawi, A. Saleha, A. Salwa, N. H. Hassan, N. M. Zahari, M. Z. Ramli, and Z. C. Muda. A review: Fundamentals of computational fluid dynamics (CFD). 2018.

[25] Antony Jameson and Luigi Martinelli. Mesh Refinement and Modeling Errors in Flow Simulation. *AIAA Journal*, 1998.

[26] S. Faure, D. Pham, and R. Temam. Comparison of finite volume and finite difference methods and application. *Analysis and Applications*, 2006.

[27] Matania Ben-Artizi and Joseph Falcovitz. Generalized Riemann Problems: From the Scalar Equation to Multidimensional Fluid Dynamics. In *Recent Advances in Computational Sciences*, 2008.

[28] P. Navarro E. Vazquez Cendon, A. Hidalgo. The riemann problem in computational science. *CRC Press*, 2012.

[29] title = Turbulent Flows journal = Cambridge University Press year = 2000 S.B. Pope, P.J Eccles.

[30] David S.-K. Ting. Basics of engineering turbulence. *U.K: Academic Press*, 2016.

[31] O. Métais. Large-Eddy Simulations of Turbulence. In M. Lesieur, A. Yaglom, and F. David, editors, *New trends in turbulence Turbulence: nouveaux aspects*. Springer Berlin Heidelberg, 2001.

[32] D. Wilcox. Turbulence modelling for cfd. *DCW Industries*, 1993.

[33] Giancarlo Alfonsi. Reynolds-averaged navier stokes equations for turbulence modelling. *Applied Mechanics Reviews*, 2009.

[34] J. L. Lumley. Toward a turbulent constitutive relation. *Journal of Fluid Mechanics*, 1970.

[35] Barrett Baldwin and Timothy Barth. A one-equation turbulence transport model for high Reynolds number wall-bounded flows. In *29th Aerospace Sciences Meeting*. American Institute of Aeronautics and Astronautics, 1991.

[36] D. Wilcox and R. Traci. A complete model of turbulence. *9th Fluid and PlasmaDynamics Conference*, 1976.

[37] johan C. Kok. Resolving the dependence on freestream values for the k-omega turbulence model. *AIAA Journal 38*, 2000.

[38] K. Hanjalić and B. E. Launder. A Reynolds stress model of turbulence and its application to thin shear flows. *Journal of Fluid Mechanics*, 1972.

[39] S M Salim, K C Ong, and S C Cheah. Comparison of RANS, URANS and LES in the Prediction of Airflow and Pollutant Dispersion. *World Congress on Engineering and Computer Science*, 2011.

[40] H. Zhang, C. Bachman, and H. Fasel. Reynolds-averaged Navier-Stokes calculations of unsteady turbulent flow. In *38th Aerospace Sciences Meeting and Exhibit*. American Institute of Aeronautics and Astronautics, 2000.

[41] M. Karczewski M.Stajuda. Development of a cfd model for propeller simulation. *Polytechinc of Lodz*, 2016.

[42] Alessandro Zarri, Alexandros Koutsoukos, Francesco Avallone, Frits de Prenter, Daniele Ragni, and Damiano Casalino. Aeroacoustic Interaction Effects of Adjacent Propellers in Forward Flight. 2023.

[43] Siemens Digital Industries Software. Star-ccm+ user guide. *Star-CCM+*, 2024.

[44] Austin Thai and Sheryl M. Grace. Prediction of small quadrotor blade induced noise. In *25th AIAA/CEAS Aeroacoustics Conference*. American Institute of Aeronautics and Astronautics, 2019.

[45] Patricia Ventura Diaz and Steven Yoon. Computational study of NASA's quadrotor urban air taxi concept. 2020.

[46] Sophie Le Bras, Korcan Kucukcoskun, Daniel Acevedo-Giraldo, and Michel Roger. Aeroacoustic Simulations of a Pylon-Mounted Propeller Configuration at Low Reynolds Number. In *30th AIAA/CEAS Aeroacoustics Conference (2024)*. American Institute of Aeronautics and Astronautics, 2024.

[47] E. J. Alvarez, J. Mehr, and A. Ning. FLOWUnsteady: An interactional aerodynamics solver for multirotor aircraft and wind energy. *AIAA AVIATION 2022 Forum*, 2022.

[48] Zhenyu Wang and A. Pandey. A comprehensive approach to study aerodynamic and aeroacoustic performance of small multicopter unmanned aerial systems. *American Institute of Aeronautics and Astronautics*, 2018.

[49] Jennifer N. Abras and Nathan Hariharan. Comparison of computational fluid dynamics hover predictions on the S-76 rotor. *Journal of Aircraft*, 2018.

[50] Jatinder Goyal, Francesco Avallone, and Tomas Sinnige. Isolated propeller aeroacoustics at positive and negative thrust. *Aerospace Science and Technology*, 2024.

[51] A. Zarri, A. Koutsoukos, F. Avallone, F. De Prenter, D. Ragni, and D. Casalino. Aeroacoustic interaction effects of adjacent propellers in forward flight. 2023.

[52] J. Anderson R. Green E. Alvarez, E.J. Mehr. www.flow.byu.edu/flowunsteady. 2017.

[53] W. R. M. Van Hoydonck, H. Haverdings, and M. D. Pavel. A review of rotorcraft wake modeling methods for flight dynamics applications. *National Aerospace Laboratory (NLR)*, 2009.

[54] R. De Vries, N. Van Arnhem, and T. Sinnige. Aerodynamic interaction between propellers of a distributed propulsion system in forward flight. *Aerospace Science and Technology*, 2021.

[55] T. Stokkermans and et al. Aerodynamic interaction effects between propellers in typical eVTOL vehicle configurations. *Journal of Aircraft*, 2021.

[56] Alessandro Zarri, Edoardo Dell'Erba, Wim Munters, and Christophe Schram. Aeroacoustic installation effects in multi-rotorcraft: Numerical investigations of a small-size drone model. *Aerospace Science and Technology*, 2022.

[57] Zhang Sheng Gao Zheng, Siyuan Zheng. Aerodynamic characteristics study on multiple propellers in distributed electric propulsion configurations. *Physics of Fluids*, 2025.

[58] Alessandro Zarri, Alexandros Koutsoukos, Francesco Avallone, Frits De Prenter, Daniele Ragni, and Damiano Casalino. Aeroacoustic interaction effects of adjacent propellers in forward flight. *AIAA AVIATION 2023 Forum*, 2023.